RAL T 029

A STUDY OF TWO-JET AND THREE-JET PRODUCTION AT THE CERN p-$\bar{p}$ COLLIDER

by

Elizabeth Jane Buckley
Department of Physics
Queen Mary College

A thesis submitted in accordance with the regulations
for the Degree of Doctor of Philosophy
in the University of London

1986

ABSTRACT

Results on hadronic jet production in the UA1 detector at the CERN p-$\bar{p}$ Collider at centre of mass energies of 546 GeV and 630 GeV are presented. The two-jet angular distribution is presented and compared with leading order QCD predictions and the need for the non-scaling behaviour of QCD is demonstrated. An attempt is made to extract information about the kinematic form of the q^2-scale using the angular distribution. The highest mass two-jet events are used to set limits on the number of flat space-time dimensions. The production of three-jet events is studied and the Dalitz plot and angular distributions for the events are compared to the predictions from the leading order QCD bremsstrahlung formulae. Some attempt is made to study the asymmetries arising due to quark-gluon scattering. Finally the relative rates of two-jet and three-jet production are compared. Evidence that the three-jet events are characterized by a lower q^2-scale than the two-jet events is presented. The measured three-jet to two-jet ratio is used to extract a value for the strong coupling constant α_s.

ACKNOWLEDGEMENTS

On an experiment as large as UA1 it would require reproduction of the author list to thank all those people who in one way or another have made this analysis possible.

There are two people in particular to whom I owe a great deal and would like to thank. The first is Graham Thompson who has give me much help and encouragement over the last three years. He also undertook the awesome task of reading this thesis and offered invaluable comments and advice. Secondly many thanks to Bill Scott, with whom I worked very closely with while I was at CERN, for his boundless enthusiasm for physics and his insight. I should also like to thank Professor Peter Kalmus for his continued encouragement and Professor Carlo Rubbia for his support and interest in this work.

I shall take this opportunity to thank those colleagues with whom I have worked, either with or under, R. Bock, W. Kozanecki, A. Nandi, R. Sobie, D. Clarke, T.J.V. Bowcock, A. Honma, R. Batley and P. Kyberd.

Last, but not least, I would like to thank Steve for his unfailing support and encouragement which enabled me to finish this thesis on time.

This thesis is dedicated to my parents.

CONTENTS

FIGURES

TABLES

CORRECTIONS

p.17 line 16 "adopoted" should read "adopted".

p.19 line 5 "$J^P = \frac{1}{2}^-$" should read "$J^P = \frac{1}{2}^+$".

p.20 line 3 "$\mathbf{3} \otimes \mathbf{3}$" should read "$\mathbf{3} \otimes \mathbf{3} \otimes \mathbf{3}$".

p.20 line 20 "$m_{D^0} > m_\psi$" should read "$2m_{D^0} > m_\psi$".

p.23 line 11 "Figure 2.3[29]" should read "Figure 2.3[28,29]".

p.33 line 17 "$|\mathcal{M}|^2 \to 0$" should read "$|\mathcal{M}|^2 \to \infty$".

p.48 line 27 should read "the shower position with a resolution of $\sigma_y = \sigma_z = 2$ mm".

p.49 Figure 3.5 "Fixations to magnet yoke" should read "attachments to magnet yoke".

p.106 line 20 should read "The mean weight for both sample 1 and sample 2 is 1.22".

p.85 The correlation coefficient for the fitted parameters in equation 4.16 is -1.0.

p.109 The correlation coefficient for the fitted parameters in equation 5.13 is -1.0.

§1.2 the following text should be added at the end of p.18.

The initial analysis[63] based on the 1983 Collider data was performed at CERN in close collaboration with Dr. W. Scott. The following topics were covered in this initial analysis

1. The investigation of the two-jet angular distribution, including the need for scaling violations.
2. The investigation of the three-jet angular distributions and Dalitz plot.
3. The measurement of the three- to two-jet ratio, including the suggestion that three-jet and two-jet events at the same mass are characterized by different q^2-scales.
4. The determination of a value for the strong coupling constant, α_s.

I have repeated this analysis using the 1984 Collider data and have extended it to include the following topics.

1. Fitting of the shape of the two-jet and three-jet mass spectrums.

2. Investigation of the effects of resolution on the two-jet angular distribution.

3. Determination of the q^2-scale for the two-jet angular distribution. (This has also been performed independently at CERN by a different method[68].)

4. Investigation of non-scaling behaviour in the three-jet angular distributions.

The jet energy correction procedure[55] described in §4.1 was developed in conjunction with Dr. W. Kozanecki.

§4.2 p.72 the following lines should be added after line 13.

The χ^2 per d.o.f is 6.6 for Figure 4.9a and 3.3 for Figure 4.9b, indicating that these curves do not provide a very good description of the data.

§4.3 p.75 line 6 – 10 are replaced by the following text.

These curves provide a reasonable description of the data (χ^2 per d.o.f = 2.3 for Figure 4.11a and 1.1 for Figure 4.11b) but can be improved to give the solid curves. These curves include both $\alpha_s^2(q^2)$ and $F(x_1,q^2)F(x_2,q^2)$ terms and give a better description of the data with a χ^2 per d.o.f of 0.43 for Figure 4.11a and 1.0 for Figure 4.11b.

§5.5 p.115 lines 4 – 15 are replaced by the following text.

In Figure 5.13a the $\cos\theta_3$ distribution is plotted (after unsmearing and renormalization to 492.2 events). The solid curve is the theoretical prediction including non-scaling effects for $A = 2.5$, with the mean q_{3J} being $0.26m_{3J}$ giving a χ^2 of 10 for 6 degrees of freedom. Almost identical curves are obtained for other choices of A such as 1.5 and 7.5, giving $\langle q_{3J}\rangle \sim 0.2m_{3J}$ and $0.45m_{3J}$ respectively and $\chi^2 \sim 10$, and hence are not shown. This is identical to the two-jet situation where a wide range of possible values for A gave reasonable agreement with the data. There is a clear deviation from scaling behaviour (dashed curve, χ^2 per d.o.f = 4.2) with a tendency for the non-scaling curve to become flatter around $\cos\theta_3 = 0$. Figure 5.13b shows the $|\psi|$ distribution for the data. The solid curve is obtained using $A = 2.5$ as above, yielding a χ^2 per d.o.f of 1.2, and again the curves for the other choices of A are almost identical and have χ^2 per d.o.f $\sim$ 1.2. Here again the deviation from perfect scaling (dashed curve, χ^2 per d.o.f = 3.2) is apparent.

§6.2 p.122 lines 25 – 27 and p.124 lines 1 – 8 are replaced by the following text.

For both mass and boost this choice does not provide a very good description of the data (χ^2 per d.o.f = 8.0 and 7.8 respectively), with the curve falling significantly below the points in both plots. The other three curves are obtained by taking a significantly lower scale for the three-jet events, while keeping $q_{2J} = 0.45 m_{2J}$. The uppermost curve (dash-dotted) corresponds to $q_{3J} = 0.2 m_{3J}$ and clearly this choice is too low as it predicts a much higher ratio than is observed (χ^2 per d.o.f = 7.4). The dashed curve uses $q_{3J} = 0.26 m_{3J}$ and this choice clearly provides a good description of the data as does the dotted curve for which $q_{3J} = 0.3 m_{3J}$ (χ^2 per d.o.f = 0.75 and 1.13 respectively). The data plotted versus boost are fitted equally well by the dashed curve and the dotted curve (χ^2 per d.o.f = 1.5) but the dash-dotted curve is not a good description of the data with χ^2 per d.o.f = 9.3.

§6.3 p.126 The following text should be added to the end of §6.3.

Recently the UA2 Collaboration[67] and the AFS Collaboration at the ISR[69] have published measurements of α_s. As they use a different approach from the one described here the methods will be described briefly.

The AFS Collaboration define jets using a window jet algorithm to obtain inclusive samples of two-jet and three-jet events. They define an uncorrected α_s by equating jets directly with partons and determining the experimental three- to two-jet ratio. The final corrected value of α_s is obtained by the use of a tuned version of the ISAJET Monte Carlo to study the effects of fragmentation and detector acceptance and hence obtain a correction factor. The result quoted is

$$\alpha_s(L.O.) = 0.18 \pm 0.03 \pm 0.04 \quad \text{at} \quad \langle q^2 \rangle \sim 300 \text{ GeV}^2 \qquad (6.13)$$

where the first error is statistical and the second is systematic.

The UA2 Collaboration define their jets using a cluster algorithm and then define exclusive samples of two- and three-jet events. They use a full QCD Monte Carlo to generate events which are then simulated through the UA2 apparatus and use these events to define a theoretical three- to two-jet ratio R_{QCD}. The

corresponding ratio R_{exp} is found from the data and the value of α_s required to make $R_{QCD} = R_{exp}$ is

$$\alpha_s(L.O.) = 0.23 \pm 0.01 \pm 0.04 \quad \text{at} \quad \langle q^2 \rangle \sim 1700 \text{ GeV}^2. \tag{6.14}$$

Both these measurements assume that $q_{2J} = q_{3J}$ and so can be compared to the first line of Table 6.3 where

$$\alpha_s(L.O.) = 0.226 \pm 0.012 \pm 0.041 \quad \text{at} \quad \langle q^2 \rangle \sim 6000 \text{ GeV}^2. \tag{6.15}$$

This result compares very favourably with the UA2 result. It is a little high compared to the AFS result, which is at $\sqrt{s} = 63$ GeV, but is still within the quoted errors.

The AFS Collaboration note in their publication that all three determinations of α_s rely on the independent fragmentation model and that if string fragmentation models were used instead the values could well come out higher, in analogy with e^+e^- experiments. Recent work by Bengtsson, Sjöstrand and van Ziji[70] of the University of Lund indicates that this may well be the case. They have studied in detail the effects of the different fragmentaion models on the value of the three- to two-jet ratio. They found that the string model produces fewer three-jet final states than the independent fragmentation model and the discrepency between the three- to two-jet ratio from the independent model and that from the string model may be a much as a factor of two at the ISR energy. This discrepency decreases as a function of energy, actually as $1/E_{T_{min}}$ where $E_{T_{min}}$ is the minimum jet E_T (or minimum invariant mass in the case of the results presented in this thesis), and hence is less important at SPS energies. They find that to allow for the effect of string fragmentation the AFS result needs to be increased by 55% while the UA2 result and the results presented here need to be increased by only 13%. Applying these corrections gives

$$\begin{aligned} \text{AFS} &: \alpha_s = 0.28 \\ \text{UA2} &: \alpha_s = 0.26 \\ \text{This thesis(UA1)} &: \alpha_s = 0.26 \end{aligned} \tag{6.16}$$

thus bringing the AFS result much closer to the other two results.

All three values are much higher than those obtained in e^+e^- experiments but as has been discussed previously this can be attributed to different q^2-scales for two-jet and three-jet events.

1. INTRODUCTION

1.1 The Proton-Antiproton Project

Probably one of the most exciting achievements of High Energy Physics over the last few years has been the successful operation of the CERN Super Proton Synchrotron (SPS) as a proton-antiproton collider and the subsequent discovery of the W and Z^0 particles, an achievement for which Carlo Rubbia and Simon van der Meer were awarded the 1984 Nobel Prize for Physics[1].

The project was motivated by the desire to produce the W and Z^0 particles, known as the Intermediate Vector Bosons, postulated to be the carriers of the weak force. These particles were predicted by the Weinberg-Salam model[2,3] and were expected to be very massive, $\sim$ 80 GeV (from here onwards we will use the convention that $\hbar = c = 1$) for the W^+ and W^- (eighty times the proton mass), while the Z^0 would be even heavier at $\sim$ 90 GeV.

In 1976 there was no machine capable of producing these objects. Fixed target machines cannot produce enough energy because the interaction must conserve momentum and so for a beam of particles of energy E, the available energy for producing new particles, $\sqrt{s}$, increases as $E^{1/2}$. This means that in order to produce a W boson by colliding a beam of protons at, say, a hydrogen target would require a beam energy of about 3.5 TeV. This problem can be overcome by having two counter-rotating beams of particles which are allowed to collide head-on at certain points in their orbit. If the two beams each have energy E then the centre of mass of the collision is at rest in the laboratory and the energy available for particle creation rises as E.

So in 1976 it was proposed by Rubbia et al.[4] that the CERN SPS could be converted into a proton-antiproton collider which would provide enough energy and luminosity to produce the Intermediate Vector Bosons, if indeed they existed. This route was chosen rather than a proton-proton collider (which would have been easier) because a $W^{\pm}$ or a Z^0 is produced when a quark annihilates with an antiquark and there would not be sufficient high momentum antiquarks in the proton to produce a reasonable event rate.

One of the major problems was how to produce and store a sufficient quantity of antiprotons to enable the desired luminosity to be reached. Antiprotons do not occur naturally but have to be created in high energy collisions. This process is not very efficient, to produce one antiproton requires about 10^6 protons so that for 10^{13} protons/second interacting in a target, about 10^7 antiprotons/second are produced. Therefore, if this process is repeated over the course of one day then $N_{\bar{p}} \sim 10^{11}$ can be reached.

After production the antiprotons then have to be stored, a procedure which is complicated by the range of directions and momenta which they acquire during production. These random motions have to be reduced, a process known as cooling. Cooling increases the particle density in six-dimensional phase-space (three space and three momentum co-ordinates) and reduces the size of the beam. In the Antiproton Accumulator (AA) this density is increased by a factor of 10^9.

However cooling appears to violate Liouville's Theorem which requires that the phase-space volume and the number of particles remains a constant. This means that we cannot compress the phase-space by conservative forces such as electromagnetic fields, we can only distort it without changing the density. However there is a way of overcoming this by using the fact that the particles are points in phase-space with empty space in between and therefore we can push the particles towards the centre of the phase-space while squeezing the empty space outwards so that on the macroscopic level the particle density increases but the small-scale density is strictly conserved. This can only be achieved if information is available about the position in phase-space of individual particles and if we are able to direct the pushing action against the particles.

This is the basis of stochastic cooling, a technique invented in 1968 by Simon van der Meer of CERN[5]. It was originally used at the ISR to reduce the emittances of the proton beams and it was proposed that it could be used to cool beams of antiprotons. A stochastic cooling system consists of a sensor or *pick-up* that acquires electrical signals from the particles and a *kicker* that pushes the particles.

The antiproton beam has to undergo both momentum (longitudinal) cooling

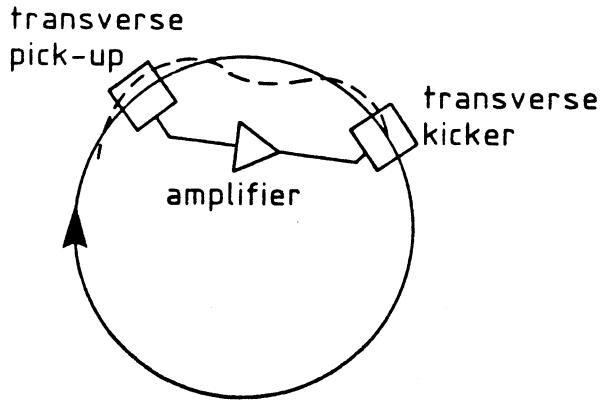

Figure 1.1 Cooling horizontal betatron oscillations.

and betatron (transverse) cooling. Cooling the transverse oscillations of a single particle is fairly straightforward. Under the influence of the focussing fields the particle executes betatron oscillations about its central orbit. A differential pick-up measures the displacement of the particle from its ideal orbit and this pick-up is connected via an amplifier to a kicker which will correct the displacement of the particle. If the distance between the pick-up and the kicker is an odd number of quarter betatron wavelengths and if the gain is correct then the oscillation will be cancelled as shown in Figure 1.1. In practice there are a very large number of particles, $\sim 10^6$ and hence even with very fast electronics their signals will overlap. However each particle's signal will still be there so cooling is taken care of, but the gain must now be reduced because all the other particles with overlapping signals will have a heating effect due to their random phases with respect to each other. On average this heating effect is zero, it is only the second-order term that contributes and this is proportional to the gain squared whereas the cooling effect varies linearly with the gain. Therefore we can always choose the gain so that the cooling effect dominates.

Momentum cooling reduces the energy spread and increases the longitudinal density and is found to be the dominant effect in the accumulation of antiprotons. There are two methods of momentum cooling, the Palmer method and the notch filter or Thorndahl method[6]. The Palmer method utilizes the relationship between the momentum of a particle and its radial position. A pick-up is placed at a point where the dispersion is high so that the particle position depends strongly on momentum. This is similar to the method for transverse cooling described

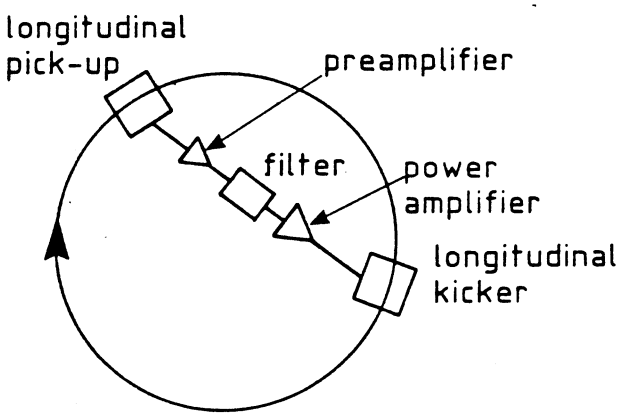

Figure 1.2 Filter method of cooling.

above but the kicker must now give longitudinal kicks. The Thorndahl method uses a sum pick-up followed by a filter to discriminate between particles of different energies. The filter used is a transmission line shorted at its far end and whose length is equal to half a rotation period. It behaves like a short-circuit at all resonant frequencies, showing characteristic notches at these frequencies. Thus particles with low momentum are accelerated and those with high momentum decelerated until all the particles have fallen into notches. The filter method is illustrated in Figure 1.2.

There exists an alternative way of cooling beams of antiprotons which was proposed by Budker[7] in 1966. This method, known as electron cooling, uses a cold electron beam superimposed on an antiproton beam which is cooled by electromagnetic interactions (scattering).

The Initial Cooling Experiment (ICE)[8,9] tested both of these methods successfully. The original plan was to use electron cooling but this required antiprotons of low energy to work well and so an additional ring would have been required to decelerate the antiprotons. Hence the stochastic solution with one ring and a fixed field was preferred.

Stochastic cooling was shown to work in Spring 1978 and so shortly afterwards the p-$\bar{\text{p}}$ project was authorized and construction of the Antiproton-Accumulator (AA) and conversion of the SPS to a collider were started. The work was completed within three years and the first collisions were seen in December 1981[10] at $\sqrt{s} = 546$ GeV at a luminosity of $5 \times 10^{27}\text{cm}^{-2}\text{s}^{-1}$ and the first physics results soon followed[11]. The layout of the CERN accelerator complex is shown

in Figure 1.3.

From production of antiprotons to injection of the beams into the SPS takes about 24 hours. The process starts with the Proton Synchrotron (PS). Every 2.6 seconds a beam of 10^{13} protons is accelerated to 26 GeV by the PS and focussed onto a tungsten target followed by a magnetic horn. There are 1.2×10^{7} antiprotons produced for every one of these proton pulses that fall within the acceptance of the AA, which is at a momentum of about 3.5 GeV, close to the production maximum.

The injected $\bar{p}$ pulse is pre-cooled in 2.2 seconds using the filter method in the outer part of the AA. It is then passed across into the inner part of the vacuum chamber and the *shutter*, which separates the two halves of the ring, is closed ready for the next pulse to be injected. The stack is cooled continuously, causing the particles to migrate gradually towards the dense core of the stack. The cooling is carried out by a system of 32 pick-ups and 100 kickers. After about 24 hours, some 10^{11} antiprotons have been accumulated, a good stack consists of about 3×10^{11} antiprotons. A fraction of this stack,typically about 30 %, (in 1984 about 0.6×10^{11} antiprotons) is extracted to the PS and accelerated to 26 GeV and then transferred to the SPS in the form of three bunches along with three bunches of protons. The remaining antiprotons in the AA then form the basis of the new stack.The complete cycle is illustrated in Figure 1.4[12,13].

The protons and antiprotons are then accelerated in the SPS to a momentum of 273 GeV. In 1984 the collider was upgraded, enabling beam momenta of 315 GeV to be reached. With the magnets of the SPS operating in continuous mode it is only possible to achieve a maximum beam momentum of 315 GeV compared to pulsed mode where 450 GeV can be reached. In 1984 a typical *shot* had a luminosity of $2.5 \times 10^{29} \mathrm{cm}^{-2}\mathrm{s}^{-1}$ with a lifetime of about 24 hours and the integrated luminosity delivered by the machine was $\sim 390\ \mathrm{nb}^{-1}$. Similar luminosities have been reached in 1985 and with the lifetime of the beams now approaching 30 hours the integrated luminosity delivered was $\sim 500\ \mathrm{nb}^{-1}$. At these luminosities the collisions occur at a rate of 12000 per second!

Six experiments UA1 - UA6[14] were approved to take data at the collider.

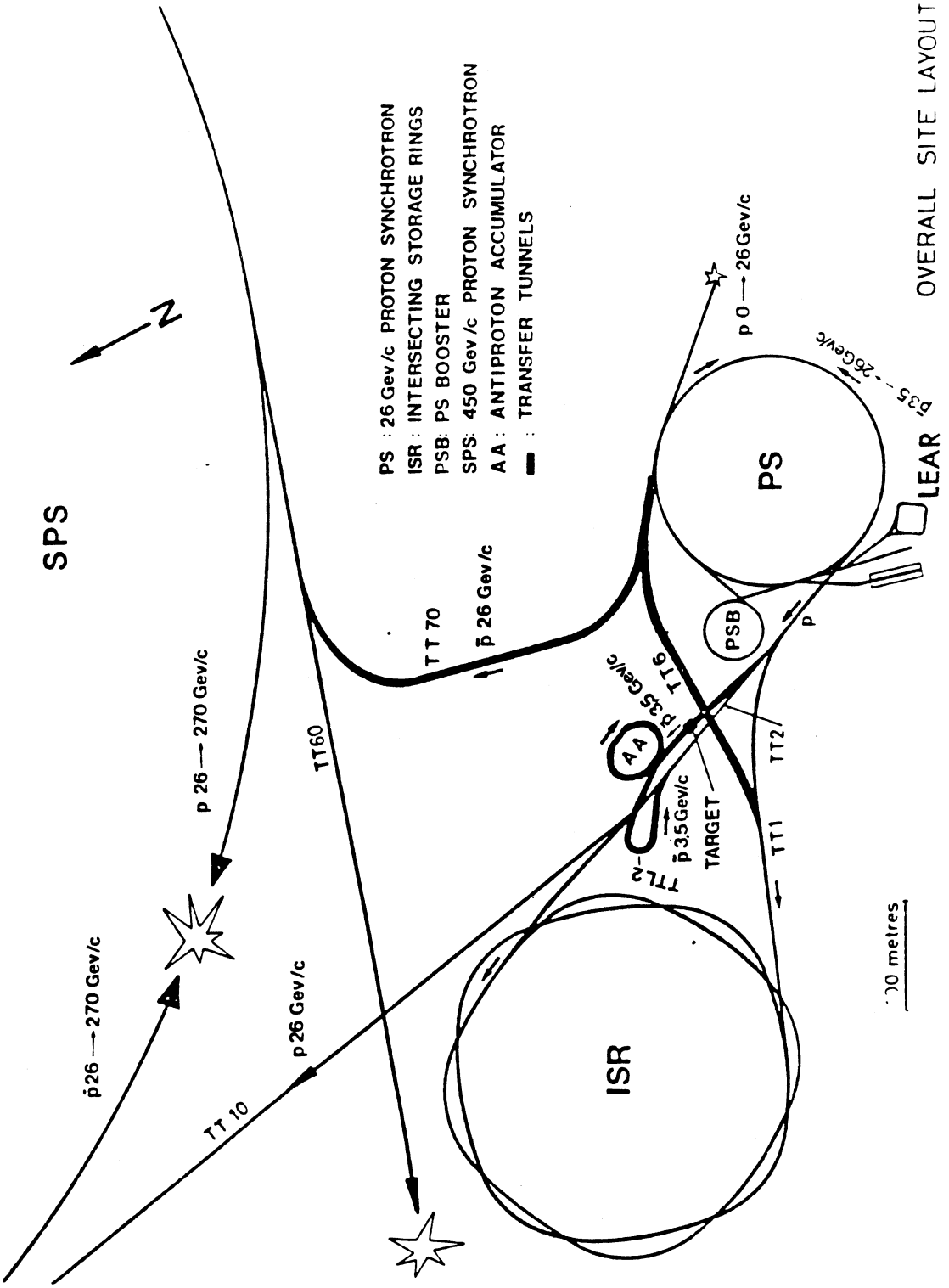

Figure 1.3 Layout of the CERN accelerator complex.

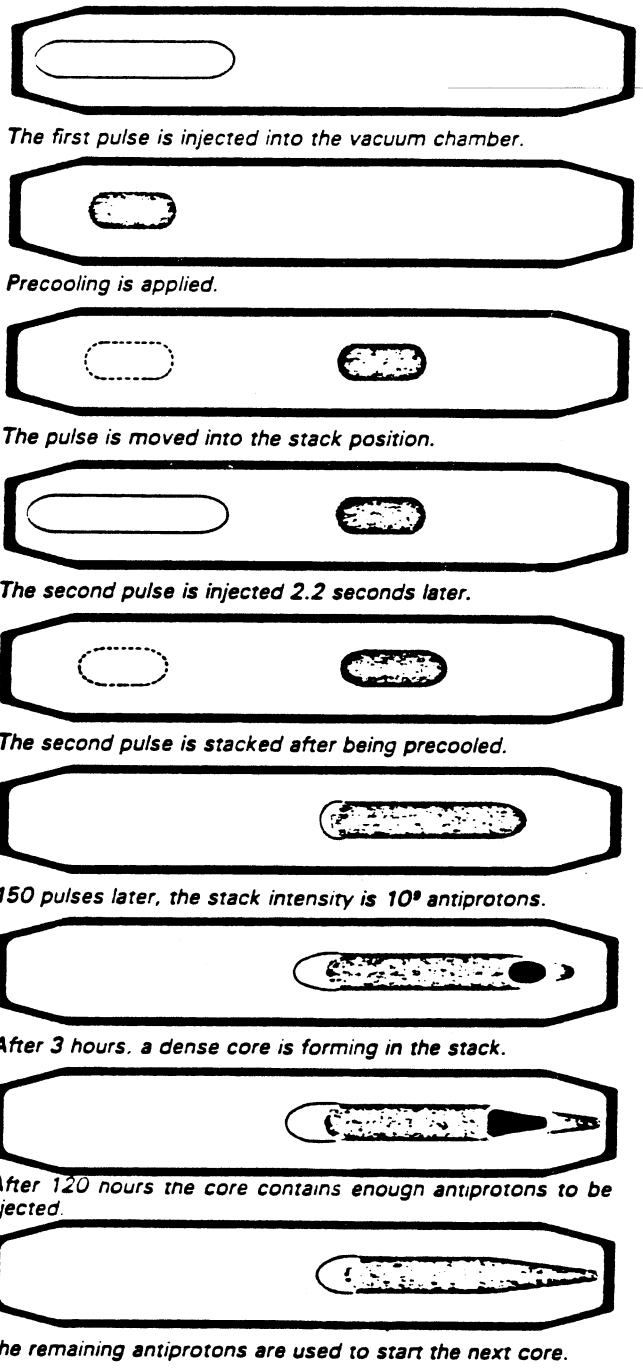

Figure 1.4 Cooling and stacking cycle of the AA.

Only two of them, UA1 and UA2 are capable of detecting the Intermediate Vector Bosons, while the other experiments (UA3-UA6) are much smaller pieces of apparatus. The results presented in this thesis are based upon data accumulated by the UA1 experiment, the largest experiment at the collider, built and operated by about 170 physicists from 18 institutions in Europe, the United States and Canada.

1.2 This Thesis

The results presented here are an analysis of two-jet and three-jet events in the high transverse energy jet data collected by the UA1 experiment in 1983 and 1984. There are basically two ways of performing an analysis of this type.

1. Select a fairly large sample of events using reasonably loose criteria and compare them to generated events from a full QCD Monte Carlo that have been passed through a full simulation of the UA1 apparatus. The Monte Carlo can be used to investigate in detail any problems due to detector acceptance, jet fragmentation, jet algorithms etc., and to correct for them.

2. The other method, and the one adopoted here, is to select a very small subset of the data with restrictive cuts so that the events populate regions of the detector where the acceptance is good and problems due to fragmentation, algorithms etc., are much reduced. One then compares the events to Monte Carlo calculations done at the parton level.

The organization of this thesis will be as follows. In Chapter 2 there is a brief discussion of the quark-parton model based on deep inelastic scattering results. There is then a fuller description of the theory of Quantum Chromodynamics (QCD), believed to be the best candidate for a theory of strong interaction physics. Chapter 3 contains details of the UA1 apparatus with a description of each of the major components of the detector.

Following these are three chapters of results. Chapter 4 concentrates on two-jet production. There is a description of the UA1 jet-finding algorithm and the corrections that have to be applied to the reconstructed jet energies. The data

selection procedure is described in some detail and the raw angular distributions are shown together with predictions from leading order QCD. The need for the non-scaling behaviour of QCD is then discussed and much better agreement is obtained between theory and experiment when this is taken into account. The effects of acceptance and resolution smearing are then considered and the data is corrected accordingly. An attempt is then made to determine the q^2-scale appropriate to the two-jet angular distribution. Finally the distribution for the very highest mass two-jet events is used to try and place limits on the number of flat space-time dimensions.

In Chapter 5 results are presented on three-jet production. The form of the three-jet differential cross-section is investigated and can be described in terms of four independent dimensionless phase-space variables. The data sample selection is then presented, with the final event sample being selected by placing cuts on the aforementioned variables. After acceptance corrections the three-jet Dalitz plot for the sample is shown along with the angular distributions and compared to the predictions of the leading order QCD bremsstrahlung formulae. Evidence is presented of the need for non-scaling effects in the angular distributions and an appropriate q^2 choice is made. Lastly an attempt is made to look for possible asymmetries in the angular distributions arising from quark-gluon scattering.

In Chapter 6 a comparison of three-jet and two-jet production rates is made. The theoretical integrated two-jet and three-jet cross-sections are computed for the choice of cuts used and there is evidence that the three-jet cross-section can be represented by a universal subprocess as in the two-jet case. Results are then presented on the ratio of three-jet to two-jet events first as a function of subprocess centre of mass energy and then as a function of boost. Evidence is given for the three-jet events being characterized by a lower q^2-scale than two-jet events of the same mass. Finally an attempt is made to extract a value for the strong coupling constant α_s using the measured three-jet to two-jet ratio. Finally in Chapter 7 some conclusions are drawn.

2. THEORETICAL BACKGROUND

2.1 The Static Quark Model of Hadrons

It was known by 1964 that the large number of 'elementary' particles could be grouped into families according to their spin and parity. The known baryons formed a decuplet with $J^P = \frac{3}{2}^+$ and an octet with $J^P = \frac{1}{2}^-$ while the mesons existed as nonets (actually a singlet and an octet), the pseudoscalar mesons with $J^P = 0^-$ and the vector mesons with $J^P = 1^-$. The members of these multiplets could be arranged according to their strangeness S and third component of isospin I_3. On a plot of S against I_3 the members of each isospin multiplet had essentially the same mass but states of different strangeness differed quite substantially in mass. However the mass difference for each increment of strangeness was roughly the same. This did not seem to be an accident, in fact the Ω^- baryon was predicted on this basis three years before it was actually discovered [15].

In 1964 Gell-Mann[16] and Zweig[17] put forward a hypothesis that could explain the observed regularities. They postulated that there existed three types of fermion known as quarks, each of a different *flavour*. These three flavours were dubbed up, down and strange or u, d and s. The u and d quarks formed an $S = 0$ isospin doublet ($I_3 = +\frac{1}{2}(u)$, $I_3 = -\frac{1}{2}(d)$) while the s quark was an $S = -1$ isospin singlet. Baryons were assumed to be composed of three quarks each of baryon number $B = \frac{1}{3}$ and carrying fractional charges of $+\frac{2}{3}$ and $-\frac{1}{3}$ while the mesons, with baryon number B =0 were formed from a quark-antiquark pair. The increase in mass of the isospin multiplets with increasing strangeness could now be attributed to a mass difference between the u, d quarks and the s quark in the region of $m_s - m_{u,d} \simeq 150$ MeV.

These quarks were thought of as the fundamental representation of the symmetry group SU(3) and the higher dimensional representations, the particle multiplets, could be formed by combining the fundamental representation according to the rules of SU(3) algebra. These particle multiplets are referred to as the irreducible representations of the symmetry group and are for the mesons

$$q\bar{q} \equiv \mathbf{3} \otimes \bar{\mathbf{3}} = \mathbf{1} \oplus \mathbf{8}$$

and for the baryons

$$qqq \equiv \mathbf{3} \otimes \mathbf{3} = \mathbf{1} \oplus \mathbf{8} \oplus \mathbf{8} \oplus \mathbf{10}$$

All this is simply mathematics, it does not require the quarks to be physical objects, they could be nothing more than convenient mathematical entities that explain the regularities of the particle spectrum. One piece of evidence for the validity of the quark hypothesis came in 1974 with the discovery of charmonium.

Groups working on the SPEAR e^+e^- ring at SLAC and the Brookhaven AGS announced the discovery of a new resonance the J/ψ at a mass of 3.1 GeV with an extremely narrow total width of $\Gamma = 69 \pm 15$ keV[18,19]. The extreme narrowness of the resonance (and hence long lifetime) suggested that its decay to ordinary hadrons was strongly suppressed (the OZI rule[20]) and hence it could not be understood in terms of a strongly decaying excited state of u,d, or s quarks. Four years earlier in 1970 Glashow, Iliopoulos and Maiani[21] had proposed the existence of a fourth quark flavour called charm to account for the absence of strangeness changing neutral currents (the GIM mechanism). It was postulated that the ψ was a vector combination of $c\bar{c}$ (like the ϕ is an $s\bar{s}$ combination) with $J^{PC} = 1^{--}$. It turns out that the ψ can only decay via OZI suppressed channels because decay to the lightest charmed meson, the D^0, is forbidden by energy conservation ($m_{D^0} > m_\psi$), hence its very narrow width. If the ψ is a $q\bar{q}$ bound state then singlet and triplet spin states and s,p,d,etc., states of orbital motion should be observed analagous to those of positronium. These states were indeed observed, the ψ', ψ'' and so on.

The discovery was followed in 1977[22] by the observation of another series of narrow resonances Υ,Υ' etc.,with masses between 9.5-10.5 GeV which were explained as being bound states of a new heavier quark, 'bottom' or b. These new particles and their spectroscopy provided some fairly convincing evidence for the quark constitution of hadrons.

2.2 Deep Inelastic Scattering

Experiments at SLAC in 1968[23] involving the scattering of electrons off protons in liquid hydrogen with electron energies up to 18 GeV observed that there was a significant probability for the electron to scatter off a proton with a large momentum transfer. This suggested that the charge of the proton was localized on a few scattering centres – analagous to Rutherford's deduction from α-particle scattering that the atom contained a nucleus.

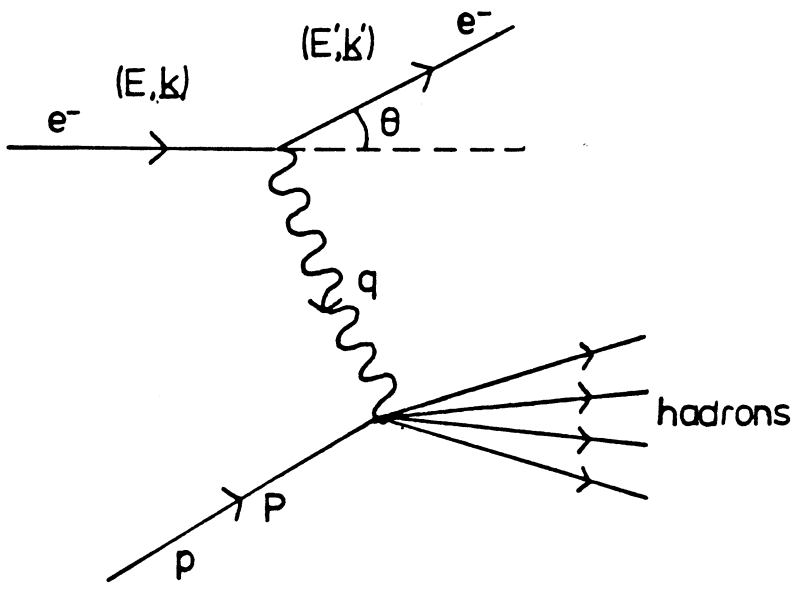

Figure 2.1 The kinematics of deep inelastic scattering.

We will discuss deep inelastic scatttering in some detail as a number of the ideas introduced here will be used later. Consider the process shown in Figure 2.1, that of an electron scattering off a proton via one-photon exchange. Defining

$$Q^2 = -q^2 = -(k - k')^2 = 4EE' \sin^2 \theta/2 \tag{2.1}$$

where Q^2 is the 4-momentum transfer squared to the struck proton,

$$\nu = E - E' = \frac{P \cdot q}{M} \tag{2.2}$$

and also the dimensionless variable

$$x = \frac{Q^2}{2M\nu} \qquad \text{where } 1 > x > 0 \tag{2.3}$$

allows us to write the cross-section in terms of Q^2 and ν as

$$\frac{d^2\sigma}{dQ^2 d\nu} = \frac{4\pi\alpha^2}{Q^4}\frac{E}{E'}\left[W_2(Q^2,\nu)\cos^2\frac{\theta}{2} + 2W_1(Q^2,\nu)\sin^2\frac{\theta}{2}\right] \tag{2.4}$$

where $W_1(Q^2,\nu)$ and $W_2(Q^2,\nu)$ are stucture functions which correspond to the two possible polarization states of the exchanged photon and can be varied independently of each other.

For any $x = Q^2/2M\nu$ and $Q^2 \geq 1GeV^2$ we have the phenomenon of Bjorken scaling[24], namely

$$\begin{aligned} MW_1(x,Q^2) &\longrightarrow F_1(x) \\ \nu W_2(x,Q^2) &\longrightarrow F_2(x) \end{aligned} \tag{2.5}$$

The Q^2 independence of the dimensionless F_1,F_2 for any x implies that the structure functions are independent of any mass scale. This effect arises naturally if the inelastic e-p scattering is due to incoherent inelastic scattering from pointlike constituents in the proton as this will be scale invariant[25]. Can these pointlike constituents, called *partons*, be identified with the quarks, in other words, do they have spin $\frac{1}{2}$ and fractional charges?

Information about the spin of the partons can be obtained by comparing cross-sections for scattering via the two alternative polarization states of the photon, longitudinal and transverse, σ_L and σ_T respectively[26]. For spin $\frac{1}{2}$ partons $\sigma_L/\sigma_T \rightarrow 0$ while for spin 0 $\sigma_L/\sigma_T \rightarrow \infty$. Assuming that partons are spin $\frac{1}{2}$ objects then we obtain a relationship between the two dimensionless structure functions, namely

$$2xF_1(x) = F_2(x) \tag{2.6}$$

which is known as the Callan-Gross relation[27]. This implies that if partons are spin $\frac{1}{2}$ then $2xF_1(x)/F_2(x) = 1$. This ratio is plotted as a function of x in Figure 2.2[28] and demonstrates that spin $\frac{1}{2}$ partons are clearly favoured over spin 0.

The fractional charge of the partons can be demonstrated by comparing the structure functions for electron-nucleon scattering with those from neutrino- nu-

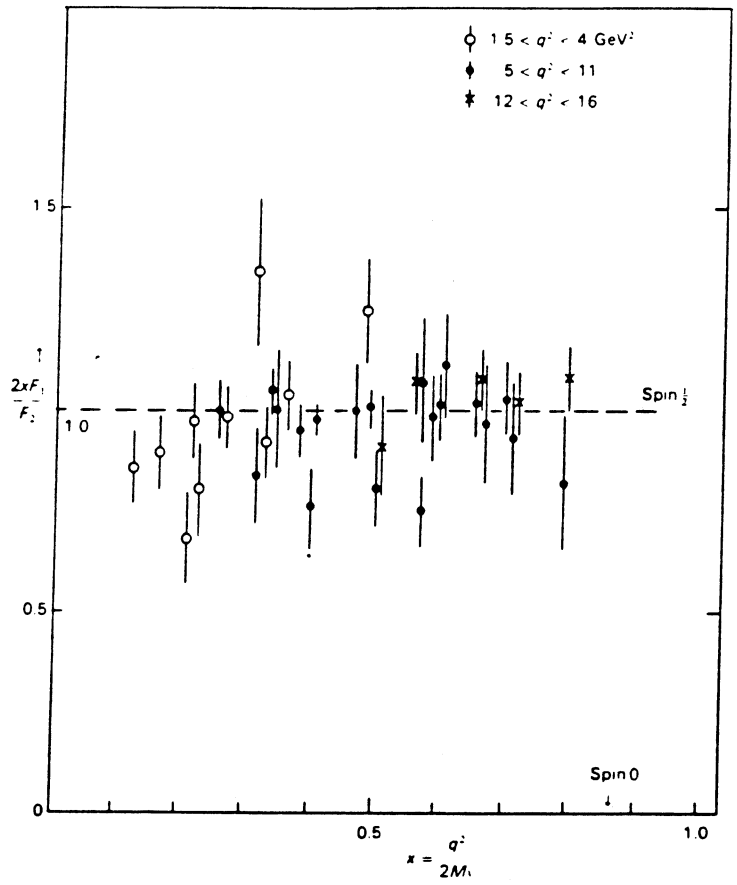

Figure 2.2 Verification of the Callan-Gross relation.

cleon scattering. We have

$$F_2^{\nu N}(x) = x\left[u(x) + d(x) + \overline{u}(x) + \overline{d}(x)\right] \tag{2.7}$$

where $u(x), d(x), \overline{u}(x), \overline{d}(x)$ are the quark and antiquark densities in the nucleon, and

$$F_2^{eN}(x) = x\left\{\frac{5}{18}\left[u(x) + d(x) + \overline{u}(x) + \overline{d}(x)\right] + \frac{1}{9}\left[s(x) + \overline{s}(x)\right]\right\} \tag{2.8}$$

i.e. the sum of the quark densities weighted by the squares of the charges. Comparing the two equations we see that

$$F_2^{\nu N}(x) \leq \frac{18}{5} F_2^{eN}(x) \tag{2.9}$$

where the factor of 18/5 results from the fractional charge of the quarks and the equality holds if s,c,... quarks can be neglected. Figure 2.3[29] shows $F_2(x)$

plotted versus x, where the points are the neutrino data from Gargamelle at CERN and the solid curve is a fit through the SLAC electron data multiplied by 18/5. It can be seen that not only do electrons and neutrinos "see" the same type of substructure but that the partons do indeed have the same fractional charges as those ascribed to the quarks.

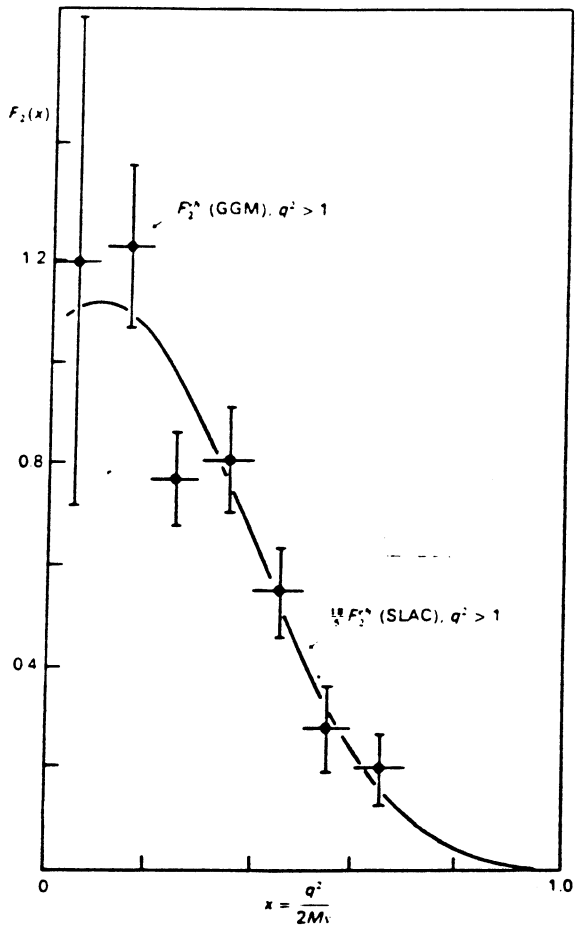

Figure 2.3 Verification of the fractional charge of the quarks.

Additional evidence for the spin $\frac{1}{2}$ nature of the partons comes from the angular distribution of '2 jet' events produced in e^+e^- anihilation in the energy range W=27-37 GeV[30]. The process occuring is

$$e^+e^- \longrightarrow q\bar{q}, \qquad q\bar{q} \longrightarrow \text{hadrons}$$

and for spin $\frac{1}{2}$ partons the angular distribution of the resulting jet of hadrons is expected to be of the form $(1 + \cos^2\theta)$ which is verified to be the case (c.f. $e^+e^- \rightarrow \mu^+\mu^-$).

All this is clear evidence that hadrons are composed of pointlike constituents called partons which we can identify with the quarks.

The area under the curve in Figure 2.3 measures the momentum fraction in the nucleon which is carried by the quarks. This turns out to be $\sim 50\%$[31] and the remaining momentum is postulated to be carried by gluons, massless particles that couple to the quarks but not to leptons. The theory which describes the interactions between the quarks and the gluons is called Quantum Chromodynamics or QCD and will be described in some detail in the rest of this chapter.

2.3 Quantum Chromodynamics

2.3.1 Colour

As well as the normal quantum numbers, the quarks possess another degree of freedom that of *colour*. This quantum number gives rise to the 'chromo' in Quantum Chromodynamics and leads to the theory being non- Abelian.

Historically colour was introduced to explain the existence of the Δ^{++} baryon which is composed of three u quarks and has $J^P = \frac{3}{2}^+$ hence the spin assignments of the quarks must be (u $\uparrow$ u $\uparrow$ u $\uparrow$) which clearly violates the Pauli principle. To overcome this difficulty it was postulated that quarks came in three colours, e.g., red,blue and green and so the quark assignments for the Δ^{++} became ($u_r \uparrow u_b \uparrow u_g \uparrow$) and the Pauli principle was no longer violated.

The introduction of colour also resolved the discrepancy between the measured ratio between $e^+e^- \rightarrow$ hadrons and $e^+e^- \rightarrow \mu^+\mu^-$ and the predicted ratio. This ratio, R, is given by

$$R = \frac{e^+e^- \rightarrow \text{hadrons}}{e^+e^- \rightarrow \mu^+\mu^-} = \Sigma e_i^2 \tag{2.10}$$

where e_i is the charge on quark i. Naïvely one expects for u,d,s quarks $R = 2/3$ and for u,d,s,c,b quarks $R = 11/9$. These values of R are substantially lower than those observed in the data. If however the quarks come in three colours then the

quantity Σe_i^2 must be multiplied by three, resulting in much better agreement between theory and experiment.

Although the quarks possess colour, all the known baryons and mesons are colour singlets, the colours of the quarks 'cancel' each other. Baryons are composed of three quarks of different colours while the mesons are a colour-anticolour quark-antiquark pair.

Quantum Chromodynamics is a non-Abelian gauge theory, the gluons also carry colour as compared with the photon in QED which is electrically neutral. The gluons form a colour-anticolour octet. There are actually $3^2 = 9$ combinations but one of these is a colour singlet and so will have no coupling to quarks or other gluons. This property of the gluons means that they can couple to each other and this is responsible for another important feature of QCD, that of *asymptotic freedom.*

2.3.2 Asymptotic Freedom

The strength of the interaction between the quarks is characterized by the strong coupling constant, α_s. As in QED, this coupling is not in fact a constant but actually depends on the masses or momentum transfer squared, q^2, in the particular process. In the leading- logarithm approximation $\alpha_s(q^2)$ is given by[32]

$$\alpha_s(q^2) = \frac{\alpha_s(q_0^2)}{1 + B\alpha_s(q_0^2)\ln(q^2/q_0^2)} = \frac{1}{B\ln(q^2/\Lambda^2)} \qquad (2.11)$$

where $B = (33-2f)/12\pi$, with f = number of quark flavours, and we have made the substitution $\Lambda^2 = q_0^2 \exp[-1/B\alpha_s(q_0^2)]$. The constant Λ characterizes the scale at which α_s becomes large and perturbation theory breaks down. We find that for $f \leq 16$ flavours $\alpha_s(q^2)$ decreases as q^2 increases. This is opposite to the effect that occurs in QED where α decreases as q^2 decreases. This behaviour is a well known phenomenon in dielectric materials where a test charge immersed in the material exerts a potential which is smaller than the Coulomb potential in free space and so the dielectric introduces a shielding effect. This also occurs in vacuum as the test charge is continually emitting and absorbing virtual photons

which can temporarily form e^+e^- pairs, again producing a shielding effect. In QCD the virtual gluons are able to form $q\bar{q}$ pairs and so again we will have a shielding effect. In QCD however there is the possibility for the gluons to couple to each other and so a gluon can give rise to a gluon pair. This increases the effective colour charge of the bare quark and produces an antishielding effect, namely a low q^2 probe will see more colour charge and hence feel a stronger coupling than a high q^2 probe. For $f \leq 16$ flavours this antishielding effect dominates over the shielding one and hence the effective coupling decreases as q^2 increases.

This means that as q^2 increases the partons will appear increasingly as if they are free particles, as is indeed observed in deep inelastic scattering. However, as q^2 decreases and approaches Λ^2 the coupling between the partons becomes very large and is thought to be responsible for the confinement of the quarks within the hadrons.

As a consequence of the dependence of the coupling constant on a mass scale the structure functions F_1 and F_2 are not dimensionless as was predicted by the naïve parton model. Instead scaling is approached asymptotically as $\alpha_s(q^2 \to \infty) \longrightarrow 0$ and at finite q^2 scaling is broken by logarithms of x and q^2.

2.3.3 Parton-Parton Scattering

Parton-parton interactions that occur at sufficiently high energies, $q^2 \gg \Lambda^2$ can be treated in the framework of perturbation theory and hence we can derive cross-sections for these processes. The cross-sections for the various parton-parton subprocesses have been calculated to leading order in α_s^2 by Combridge et al.[33].

For a particular process we can define the Mandelstam variables $\hat{s}$,$\hat{t}$ and $\hat{u}$

$$\begin{aligned} \hat{s} &= (p_1 + p_2)^2 \\ \hat{t} &= -\frac{\hat{s}}{2}(1 - \cos\theta) = (p_1 - p_3)^2 \\ \hat{u} &= -\frac{\hat{s}}{2}(1 + \cos\theta) = (p_1 - p_4)^2 \end{aligned} \tag{2.12}$$

where p_1 and p_2 are the incoming parton momenta and p_3 and p_4 are the outgoing

Parton Subprocess	$\Sigma = 2\hat{s}/\pi\alpha_s^2 \; d\sigma/d\cos\theta$
$q_1q_2 \to q_1q_2$ $q_1\bar{q}_2 \to q_1\bar{q}_2$	$\frac{4}{9}\frac{\hat{s}^2+\hat{u}^2}{\hat{t}^2}$
$q_1q_1 \to q_1q_1$	$\frac{4}{9}\left(\frac{\hat{s}^2+\hat{u}^2}{\hat{t}^2}+\frac{\hat{s}^2+\hat{t}^2}{\hat{u}^2}\right)-\frac{8}{27}\frac{\hat{s}^2}{\hat{u}\hat{t}}$
$q_1\bar{q}_1 \to q_2\bar{q}_2$	$\frac{4}{9}\frac{\hat{t}^2+\hat{u}^2}{\hat{s}^2}$
$q_1\bar{q}_1 \to q_1\bar{q}_1$	$\frac{4}{9}\left(\frac{\hat{s}^2+\hat{u}^2}{\hat{t}^2}+\frac{\hat{t}^2+\hat{u}^2}{\hat{s}^2}\right)-\frac{8}{27}\frac{\hat{u}^2}{\hat{s}\hat{t}}$
$q\bar{q} \to gg$	$\frac{32}{27}\frac{\hat{u}^2+\hat{t}^2}{\hat{u}\hat{t}}-\frac{8}{3}\frac{\hat{u}^2+\hat{t}^2}{\hat{s}^2}$
$gg \to q\bar{q}$	$\frac{1}{6}\frac{\hat{u}^2+\hat{t}^2}{\hat{u}\hat{t}}-\frac{3}{8}\frac{\hat{u}^2+\hat{t}^2}{\hat{s}^2}$
$qg \to qg$	$-\frac{4}{9}\frac{\hat{u}^2+\hat{s}^2}{\hat{u}\hat{s}}+\frac{\hat{u}^2+\hat{s}^2}{\hat{t}^2}$
$gg \to gg$	$\frac{9}{2}\left(3-\frac{\hat{u}\hat{t}}{\hat{s}^2}-\frac{\hat{u}\hat{s}}{\hat{t}^2}-\frac{\hat{s}\hat{t}}{\hat{u}^2}\right)$

Table 2.1 Lowest order parton-parton cross-sections.

parton momenta, $\hat{s}$ is the centre-of-mass subprocess (c.m.s) energy squared and θ is the c.m.s scattering angle. The various subprocess cross-sections can be written in terms of $\hat{s}$, $\hat{t}$ and $\hat{u}$ and in Table 2.1 is listed the quantity Σ for each of the subprocesses. In Figure 2.4 we show the corresponding angular distributions in $|\cos\theta|$ for the different subprocesses.

We notice that apart from the s-channel only processes (production of new parton types or flavours) all the elastic subprocesses have the same angular form $(1-\cos\theta)^{-2}$ in the limit of $\hat{s}/\hat{t} \to \infty$. In this approximation the cross-sections for gluon-gluon to gluon-quark to quark- antiquark elastic scattering are in the ratio $1 : \frac{4}{9} : \frac{16}{81}$. This ratio reflects the relative strengths of the couplings at the three-

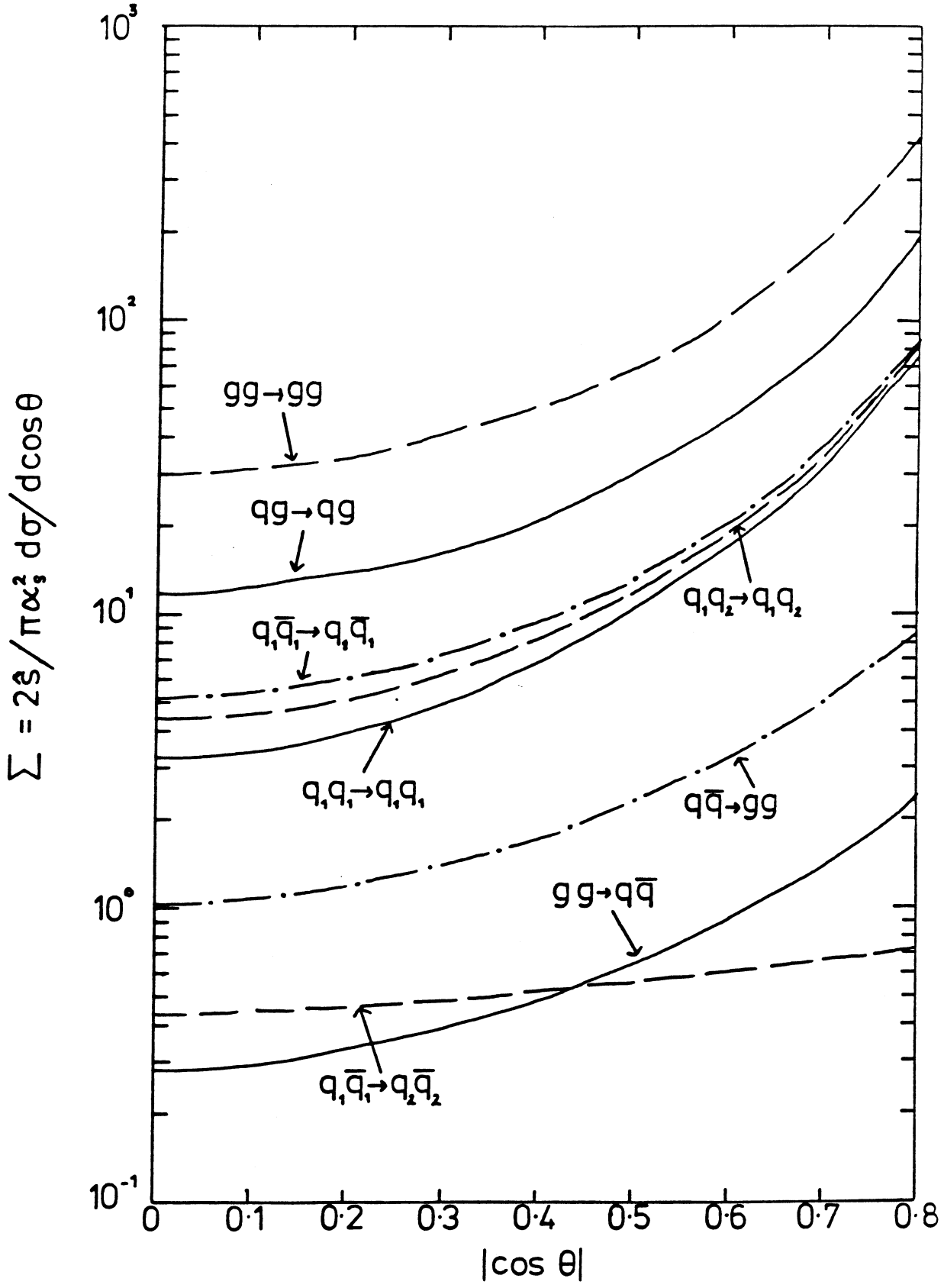

Figure 2.4 Angular distributions in $|\cos\theta|$ for $2 \to 2$ subprocesses.

gluon vertex compared to the quark-quark-gluon vertex which are given by the colour factors C_A and C_F respectively. The factors C_A and C_F are proportional to the 'probability' for a gluon to radiate a gluon (P_{gg}) and a quark to radiate a gluon (P_{gq}) respectively. For SU(N) we have $C_A = N$ and $C_F = (N^2-1)/2N$ so for $SU(3)_{colour}$, $C_A = 3$ and $C_F = 4/3$ implying that

$$\frac{P_{gg}}{P_{gq}} \propto \frac{C_A}{C_F} = \frac{9}{4}. \tag{2.13}$$

The origin of the ratio can now be explained as in Figure 2.5.

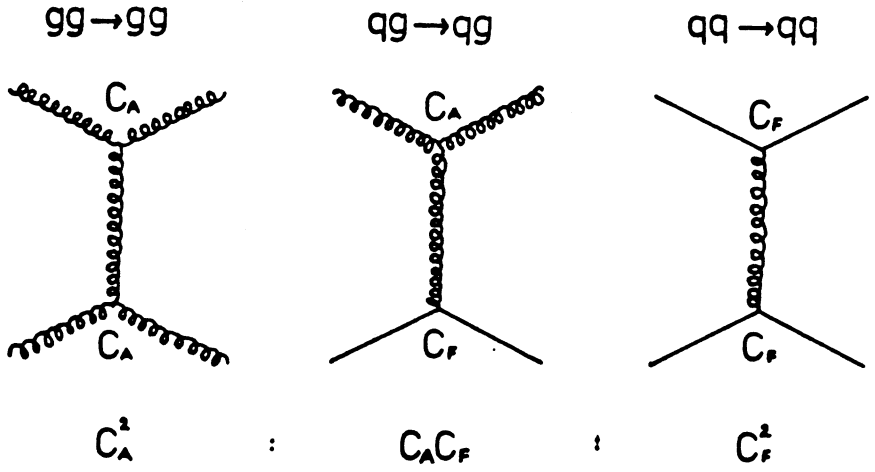

Figure 2.5 Explanation of the origin of the ratio $1 : \frac{4}{9} : \frac{16}{81}$ for $2 \rightarrow 2$ scattering.

2.3.4 Gluon bremsstrahlung

Just as in QED there is the possibility for a charged particle to radiate a photon, so in QCD there is the possibility for the coloured partons to radiate gluons as *bremsstrahlung*. In QED this probability is small, being proportional to α (= 1/137). However, in QCD this probability is much greater because it is proportional to α_s and $\alpha_s \gg \alpha$, at least for the q^2's attainable by present experiments. For this reason we cannot ignore gluon bremsstrahlung and we may have to deal with fairly complex event structures where multiple branching has

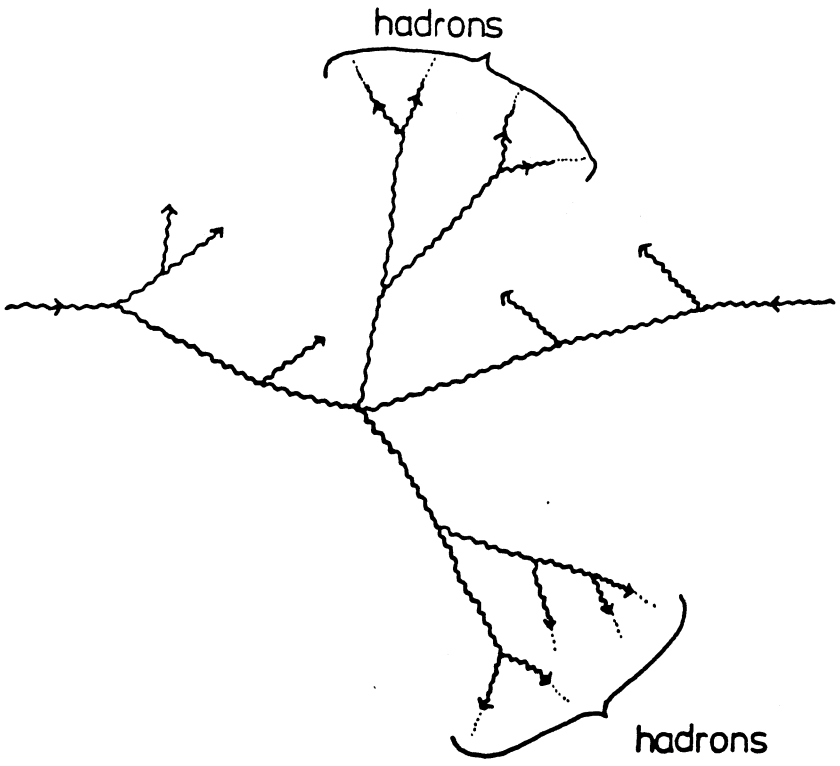

Figure 2.6 A parton-parton scatter with multiple branching.

occurred as in Figure 2.6. Ideally calculations of cross-sections should be to all orders in α_s but this is technically very difficult to achieve. Calculations exist, however, for 3-parton final states to $O(\alpha_s^3)$ by Berends et al.[34] and more recently for 4-parton final states, $O(\alpha_s^4)$, by various groups[35]. We will be concerned here only with 3-parton final states.

The matrix elements for the following subprocesses have been calculated by Berends et al.,$gg \to ggg$, $q\bar{q} \to q\bar{q}g$, $q\bar{q} \to q'\bar{q}'g$, $q\bar{q} \to ggg$. All other subprocesses can be obtained from these four matrix elements by crossing. Although they can be written in a fairly compact form, the matrix elements for 2→3 processes are much more complex than those for 2→2 processes.

Consider the subprocess

$$g(k_1) + g(k_2) \longrightarrow g(k_3) + g(k_4) + g(k_5).$$

The matrix element $|\mathcal{M}|^2$ (which is the result of evaluating 25 Feynman diagrams!)

can be written as

$$|\mathcal{M}|^2 = 32\pi^3\alpha_s^3\left[N^3/N^2-1\right]\left[(12345)+(12354)+(12435)+(12453)+(12534)\right.$$
$$+(12543)+(13245)+(13254)+(13425)+(12524)+(14235)+(14325)\left.\right]$$
$$\times\left[(12)^4+(13)^4+(14)^4+(15)^4+(23)^4+(24)^4+(25)^4\right.$$
$$\left.+(34)^4+(35)^4+(45)^4\right]/(12)(13)(14)(15)(23)(24)(25)(34)(35)(45) \tag{2.14}$$

where we have defined

$$(ijlmn) = (k_ik_j)(k_jk_l)(k_lk_m)(k_mk_n)(k_nk_i) \qquad \text{and} \qquad (ij) = (k_ik_j)$$

with $i,j,l,m,n = 1,\ldots,5$.

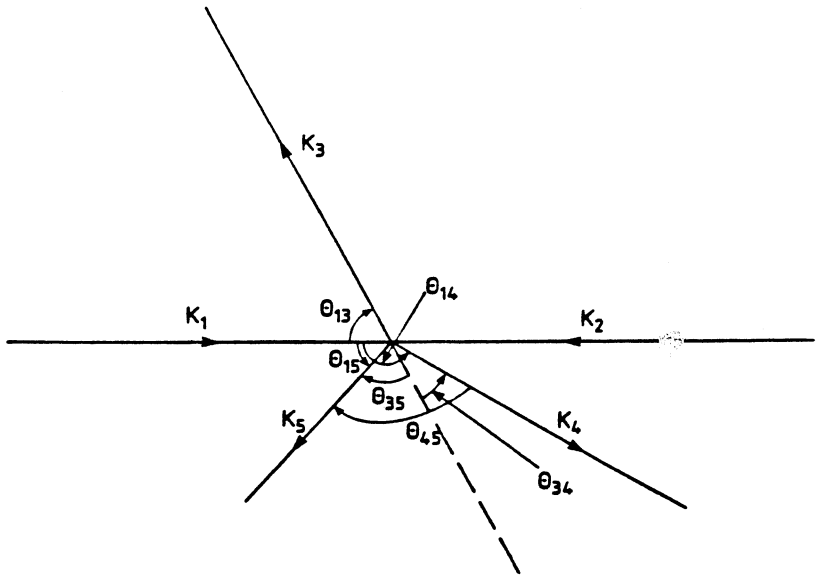

Figure 2.7 Kinematic variables in the three-parton c.m.s.

We can gain some insight into the behaviour of $|\mathcal{M}|^2$ by considering the denominator of equation 2.14. We can write the 10 dot products as follows, assuming massless partons and working in the centre-of-mass of the 3-parton system,

$$(12) = \hat{s}/2 \quad (13) = k_1k_3(1-\cos\theta_{13}) \quad (14) = k_1k_4(1-\cos\theta_{14})$$
$$(15) = k_1k_5(1-\cos\theta_{15}) \quad (23) = k_2k_3(1+\cos\theta_{13}) \quad (24) = k_2k_4(1+\cos\theta_{14})$$
$$(25) = k_2k_5(1+\cos\theta_{15}) \quad (34) = k_3k_4(1+\cos\theta_{34}) \quad (35) = k_3k_5(1+\cos\theta_{35})$$
$$(45) = k_4k_5(1-\cos\theta_{45}) \tag{2.15}$$

where k_1 and k_2 are the momenta of the incoming partons and k_3,k_4 and k_5 are the momenta of the outgoing partons, θ_{1j} is the angle between parton j and the incoming parton labelled k_1, θ_{3j} is the angle that parton j makes with $-k_3$ ($j = 3,\ldots,5$) and θ_{45} is the angle between partons 4 and 5. This is illustrated in Figure 2.7.

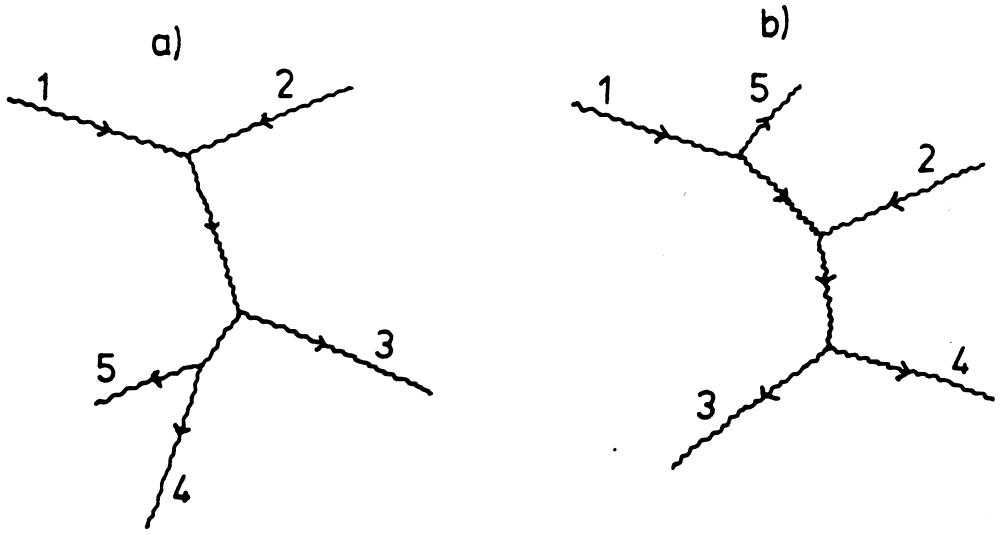

Figure 2.8 Parton-parton scatter with a) final-state radiation and b) initial-state radiation.

Now we make the substitution $m_{ij}^2 = 2k_ik_j(1-\cos\theta_{ij})$ where m_{ij}^2 is the invariant mass squared between parton i and parton j. The denominator of equation 2.14 can now be written (ignoring constant factors) as

$$|\mathcal{M}|^2 \propto \frac{\alpha_s^3}{\hat{s}} \left[m_{13}^2 m_{14}^2 m_{15}^2 m_{23}^2 m_{24}^2 m_{25}^2 m_{34}^2 m_{35}^2 m_{45}^2\right]^{-1} \qquad (2.16)$$

We can see that the matrix element will become singular if any of the m_{ij}^2's$\rightarrow 0$. So taking k_5 as being the bremsstrahlung parton then if $m_{45}^2 \rightarrow 0$ then this implies that as partons 4 and 5 approach each other and parton 5 becomes small the probability of bremsstrahlung becomes larger. In this configuration there is a high probability that parton 5 is radiated from parton 4 and this is referred to as *final-state bremsstrahlung* (Figure 2.8a). The other situation where $|\mathcal{M}|^2 \rightarrow 0$

that is of importance is when $m_{15}^2 \rightarrow 0$ or $m_{25}^2 \rightarrow 0$ meaning that the probability of bremsstrahlung is again high when parton 5 is close to either of the incoming partons. This implies that there is a high probability for parton 5 to have been radiated from parton 1 or 2 and it is referred to as an *initial-state bremsstrahlung* (Figure 2.8b). Both these situations are identical to saying that partons prefer to radiate low energy, small angle bremsstrahlung.

2.3.5 Higher order corrections – the K-factor

All our discussions up until now have been concerned with lowest order calculations for $2 \rightarrow 2$ and $2 \rightarrow 3$ processes. Unfortunately, if we require the cross-sections to all orders in α_s then there are a large number of extra diagrams which have to be considered. These extra diagrams result in a multiplicative correction , known as the K-factor, which we have to apply to the leading order cross-sections to obtain the complete cross-section.

The corrections to the parton-parton cross-section has only been considered in full for the case of distinguishable quarks[36] $q_i + q_j \rightarrow q_i + q_j$ and comes from considering the diagrams listed in Figure 2.9. Approximate calculations[37] exist for the other $2 \rightarrow 2$ processes and these are presented in Table 2.2 where $K = (1 + \alpha_s/2\pi\ (C_\ell + C_b)\pi^2)$. The coefficients C_ℓ and C_b arise from considering soft gluon loops and soft gluon bremsstrahlung respectively.

Very recently a complete calculation of the higher order corrections for all $2 \rightarrow 2$ processes to $O(\alpha_s^3)$ has been made by Ellis and Sexton[38]. They calculated the cross-sections for all $2 \rightarrow 2$ processes, in n-dimensions in order to regulate divergences, and the corresponding virtual radiative corrections. In the case of $gg \rightarrow gg$ this involved evaluating diagrams such as those in Figure 2.10 and the interference between these and the four lowest order diagrams, of which there are 108. In order to regulate the singularities due to soft or collinear parton emission the cross-sections for $2 \rightarrow 3$ were also required, again calculated in n-dimensions.

At present they have applied their results to one hadron inclusive scattering only and the indications are that the K-factor corrections are large and positive and may be angle-dependent in the case of quark-quark scattering.

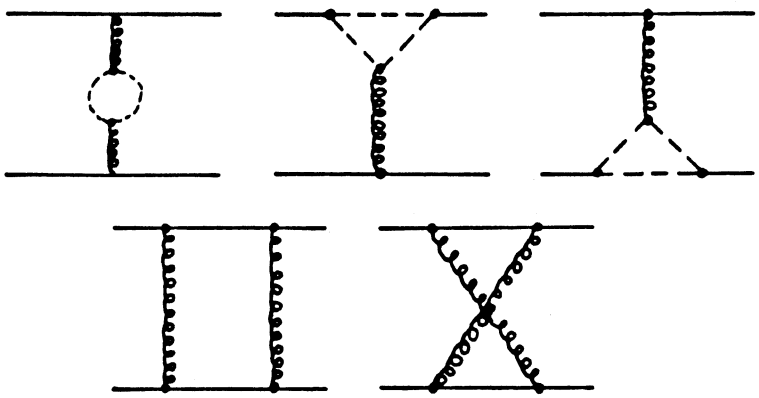

Figure 2.9 The virtual corrections to the process $q_i q_j \rightarrow q_i q_j$.

Process	C_t	C_b	K for $N = 3$ $\alpha_s = 0.15$
$gg \rightarrow gg$	$N/2$	$N/2$	1.7
$qg \rightarrow qg$	$N/2$	$N/3 - 1/6N$	1.6
$qq \rightarrow qq, qq' \rightarrow qq'$	$2/N$	$N - 5/3N$	1.7
$q\bar{q} \rightarrow gg, gg \rightarrow q\bar{q}$	$N/4 - 1/2N$	$2N/3$	1.7
$q\bar{q} \rightarrow q\bar{q}, q\bar{q} \rightarrow q'\bar{q}'$	$1/N$	$(N^2 - 1)/3N$	1.3

Table 2.2 K-factors for $2 \rightarrow 2$ processes.

Of course it is always possible to minimize these corrections by an appropriate choice of scale, and the results of ref.38 suggest that this scale is substantially lower than the 'natural' scales of $\hat{s}$ or p_T^2. As yet there are no calculations for the $O(\alpha_s^4)$ corrections to the $2 \rightarrow 3$ processes.

2.3.6 Hadronization

The mechanism of confinement prevents partons from manifesting themselves directly so there is a process known as hadronization which converts the partons

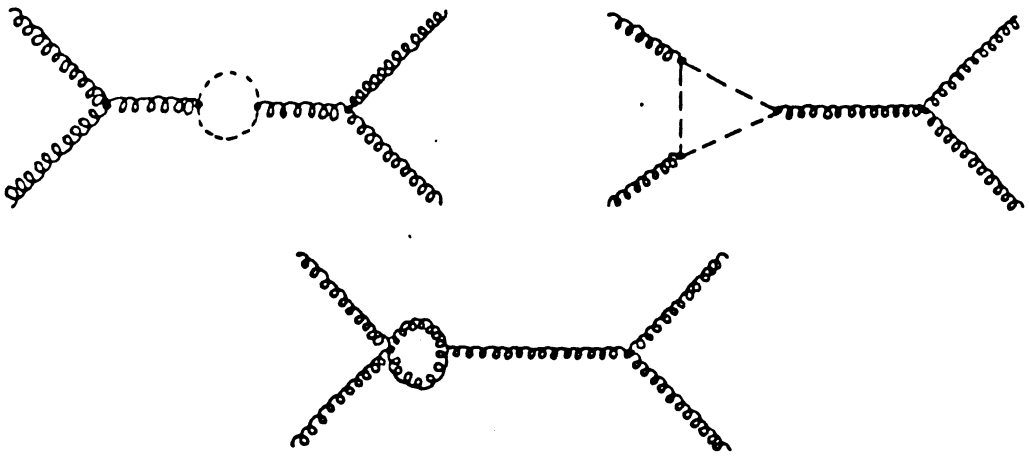

Figure 2.10 Some of the virtual corrections to the process $gg \rightarrow gg$.

into *jets* of observable hadrons. The hadronization process takes place some time after the interaction when $\alpha_s(q^2)$ is large and hence it cannot be described by perturbative QCD, instead we have to use phenomenological models. The two main models are the Independent Fragmentation Model of Field and Feynman[39] and the Lund String Model[40], both of which will be described briefly.

a) Independent Fragmentation Model

As the name of this model suggests, each quark is considered to fragment independently of the others and this fragmentation is independent of the initial scatter. Suppose that a quark of type a with momentum W_0 in the z direction creates a colour field in which new $q\bar{q}$ pairs can be produced. This quark a then combines with an antiquark $\bar{b}$ from a new pair $b\bar{b}$ to form a meson $a\bar{b}$, leaving b to combine with further antiquarks. This meson may be directly observed, a *primary* meson, or it may decay to further mesons known as secondaries. There is a hierarchy of primary mesons with $a\bar{b}$ first in *rank*, $b\bar{c}$ second in rank, $c\bar{d}$ third and so on. This is an ordering in flavour only not in momentum.

If a rank-1 primary meson carries away momentum ξ_1 from a quark-jet of type a with momentum W_0 then the remaining cascade starts with a quark of type b with momentum $W_1 = W_0 - \xi_1$. If z is the momentum fraction carried away by the meson, where $z = \xi_1/W_0$ then we can define the probability that

the rank-1 primary meson leaves a momentum fraction $(1-z)$ to the remaining cascade as $f(1-z)dz$. The fragmentation of jets is then parameterized in terms of this function $f(1-z)$ and three constants. We take

$$f(1-z) = 1 - a + 3a(1-z)^2 \tag{2.17}$$

with $a = 0.77$ chosen after examination of experimental data.

The first parameter defines the probability of a $q\bar{q}$ pair being $u\bar{u}$,$d\bar{d}$ or $s\bar{s}$. The following values are used

$$\begin{aligned} \gamma_u &= \gamma_d = \gamma \\ \gamma_s &= 1 - 2\gamma \\ \gamma &= 0.4 \end{aligned} \tag{2.18}$$

which assumes that the production of $s\bar{s}$ is half as likely as production of $u\bar{u}$.

The second parameter determines the production of resonances. The probability of a $q\bar{q}$ pair being a pseudoscalar, vector, tensor,... meson is given by $\alpha_{ps}, \alpha_v, \alpha_t, \ldots$ respectively. The values are

$$\begin{aligned} \alpha_{ps} &= \alpha_v = 0.5 \\ \alpha_t, \ldots &= 0 \end{aligned} \tag{2.19}$$

This choice leads to $N(\rho^0)/N(\pi^0) \rightarrow 1$ as $z \rightarrow 1$, which has been verified experimentally.

The final parameter is the transverse momentum of the hadrons with respect to the jet axis. Each meson is given a transverse momentum equal to the vector sum of the transverse momenta of the constituent quarks (which has a Gaussian distribution). For a cascade of primary mesons, the P_T distribution is a Gaussian with mean value

$$< P_T^2 >= 2\sigma^2 \tag{2.20}$$

which is measured by experiment to be $\sim (439\text{MeV})^2$ and leads to a value for σ^2 of $(350\text{ MeV})^2$.

This model is by no means perfect, it requires some kind of long-range final-state interaction to rearrange the colour so that the final-state hadrons are colour singlets. There is no mechanism for the production of baryons and it does not describe gluon fragmentation although it is assumed that a similar mechanism occurs. However the fragmentation model of B. Webber does deal with the problem of gluon jet fragmentation by taking into account soft gluon interference[41] and produces results similar to those described below for the Lund Model.

b) The Lund String Model

This model solves some of the problems of the above model in that it is relativistically invariant and is able to deal with gluon fragmentation. One pictures the force between two quarks as being confined to a tube or string with a string tension K (energy per unit length). If K is non-zero then this implies that an infinite amount of energy will be required to separate the two quarks and hence the quarks are confined. As a $q\bar{q}$ pair move out from some spacetime point with large equal and opposite momenta then the energy in the string may become sufficiently large so that it breaks into pieces, each one being a $q\bar{q}$ pair or meson. It is assumed that the field has no excited transverse degrees of freedom during the soft hadronization and therefore the P_T is conserved locally at each breaking point and the $q\bar{q}$ pair have large equal and opposite transverse momenta. This leads to a P_T distribution for the mesons which is Gaussian with a mean value of $(440\ \text{MeV})^2$. As the $q\bar{q}$ pairs have compensating flavours then there will be a strict ordering of mesons with respect to flavour (rank) which on average also agrees with the ordering in rapidity.

If we generalize the dynamics of the relativistic massless string to three dimensions then it is possible to have a localised excitation, a *kink*, carrying energy and momentum and moving with velocity c. This kink is pulled back with twice the force acting on an endpoint quark and behaves like a gluon. The force-field stretched from the quark to the antiquark via the gluon implies that the mesons will be produced around two hyperbolae in momentum space, there will be more mesons between the quark and gluon and the antiquark and gluon than between the quark and antiquark. An asymmetry of this type has in fact been observed

by the Jade Collaboration at Petra[42].

2.3.7 The proton structure function

The total $2 \rightarrow 2$ differential scattering cross-section can be written as

$$\frac{d\sigma}{d\cos\theta} = \int\int \sum_{i,j} \frac{F_i(x_1)}{x_1} \frac{F_j(x_2)}{x_2} \frac{d\sigma_{ij}}{d\cos\theta} dx_1 dx_2 \tag{2.21}$$

where $d\sigma_{ij}/d\cos\theta$ is the subprocess cross-section for partons i and j. The quantities $F_i(x_1)/x_1$ and $F_j(x_2)/x_2$ are the antiproton and proton structure functions respectively and they represent the number density of parton i in the antiproton and parton j in the proton, with x being the scaled longitudinal momentum of the parton and is identical to the quantity defined in equation 2.3

$$x = \frac{P_{parton}}{P_{proton}}. \tag{2.22}$$

If we assume that the elastic subprocesses dominate and have a common angular dependence as was shown in §2.3.3 then we can write the total differential cross-section of equation 2.21 as

$$\frac{d\sigma}{d\cos\theta} = \int\int \left[\sum_{i,j} \frac{F_i(x_1)}{x_1} \frac{F_j(x_2)}{x_2} c_{ij} \right] \frac{d\sigma_{gg}}{d\cos\theta} dx_1 dx_2 \tag{2.23}$$

where $d\sigma_{gg}/d\cos\theta$ is the differential cross-section for gluon-gluon scattering. In obtaining equation 2.23 we have used the result of §2.3.3 that the cross-sections for $gg \rightarrow gg$, $qg \rightarrow qg$ and $q\bar{q} \rightarrow q\bar{q}$ are in the ratio $1 : \frac{4}{9} : \frac{16}{81}$ and this enables us to write

$$\frac{d\sigma_{ij}}{d\cos\theta} = c_{ij} \frac{d\sigma_{gg}}{d\cos\theta} \qquad \text{with} \qquad i,j = qg, q\bar{q}. \tag{2.24}$$

If these are indeed the dominant subprocesses then equation 2.23 becomes

$$\frac{d^3\sigma}{d\cos\theta dx_1 dx_2} = \frac{F(x_1)}{x_1} \frac{F(x_2)}{x_2} \frac{d\sigma_{gg}}{d\cos\theta} \tag{2.25}$$

where $F(x)$ is an effective structure function given by

$$F(x) = G(x) + \frac{4}{9} \left[Q(x) + \overline{Q}(x) \right] \tag{2.26}$$

with $G(x)$ being the gluon structure function and $Q(x)$ ($\overline{Q}(x)$) being the quark

(antiquark) structure function. The ratio $1 : \frac{4}{9} : \frac{16}{81}$ means that the product of the structure functions $F(x_1)F(x_2)$ is a perfect square and this results in the factorization of the structure functions.

The structure functions are not only functions of x but also of q^2. As q^2 increases the resolving power increases and the number of gluons increases and so the momentum fraction carried by each gluon decreases, in otherwords there are more low momentum partons in the proton and the structure function *softens*. These q^2 dependences take the form of slowly varying logarithmic corrections that are expected from QCD and are known as *scaling violations* because they break the scale invariant nature of the structure functions.

3. THE APPARATUS

3.1 Introduction

The UA1 detector was designed to search for the Intermediate Vector Bosons, primarily through their leptonic decay modes, but because the experiment would be operating in an energy regime which until now had been unexplored it was important that the detector was also as general purpose as possible.

One of the most important features of the design is that the detector is 'hermetic'. The calorimetry covers almost the full solid angle, down to 0.2^0 from the beam direction. This enables the total transverse energy in an event to be reconstructed and hence the presence of any 'missing' energy, which may be caused by an escaping neutrino from a $W \rightarrow e\nu$ decay, can be detected.

The detector consists of three basic components and is constructed in a series of layers, each one fitting inside the next. A section through the detector is shown in Figure 3.1.

1. At the centre, surrounding the beam pipe is a high resolution drift chamber, the Central Detector, extending over the angular range $5^0 < \theta < 175^0$. The resulting tracks are momentum analysed by the 0.7 Tesla dipole field.

2. Surrounding the central detector are electromagnetic (e.m.) and hadronic calorimeters. The central calorimeters cover the angular range $25^0 < \theta < 155^0$ and consist of two elements, an electromagnetic part (the gondolas) and a hadronic part (the C's) which also serves as the return yoke for the magnet and as a filter for the muon chambers. The end-cap calorimetry covers the angular intervals $5^0 < \theta < 25^0$ and $155^0 < \theta < 175^0$ and again has an e.m. section (the bouchons) and a hadronic part (the I's). The forward calorimeters cover the region $0.2^0 < \theta < 5^0$ and $175^0 < \theta < 179.8^0$ and once again are divided into e.m. and hadronic compartments.

3. Outside the calorimeters are two layers of drift chambers for the detection of penetrating particles such as muons which traverse the rest of the detector without interacting. Iron shielding between the hadron calorimeter and the

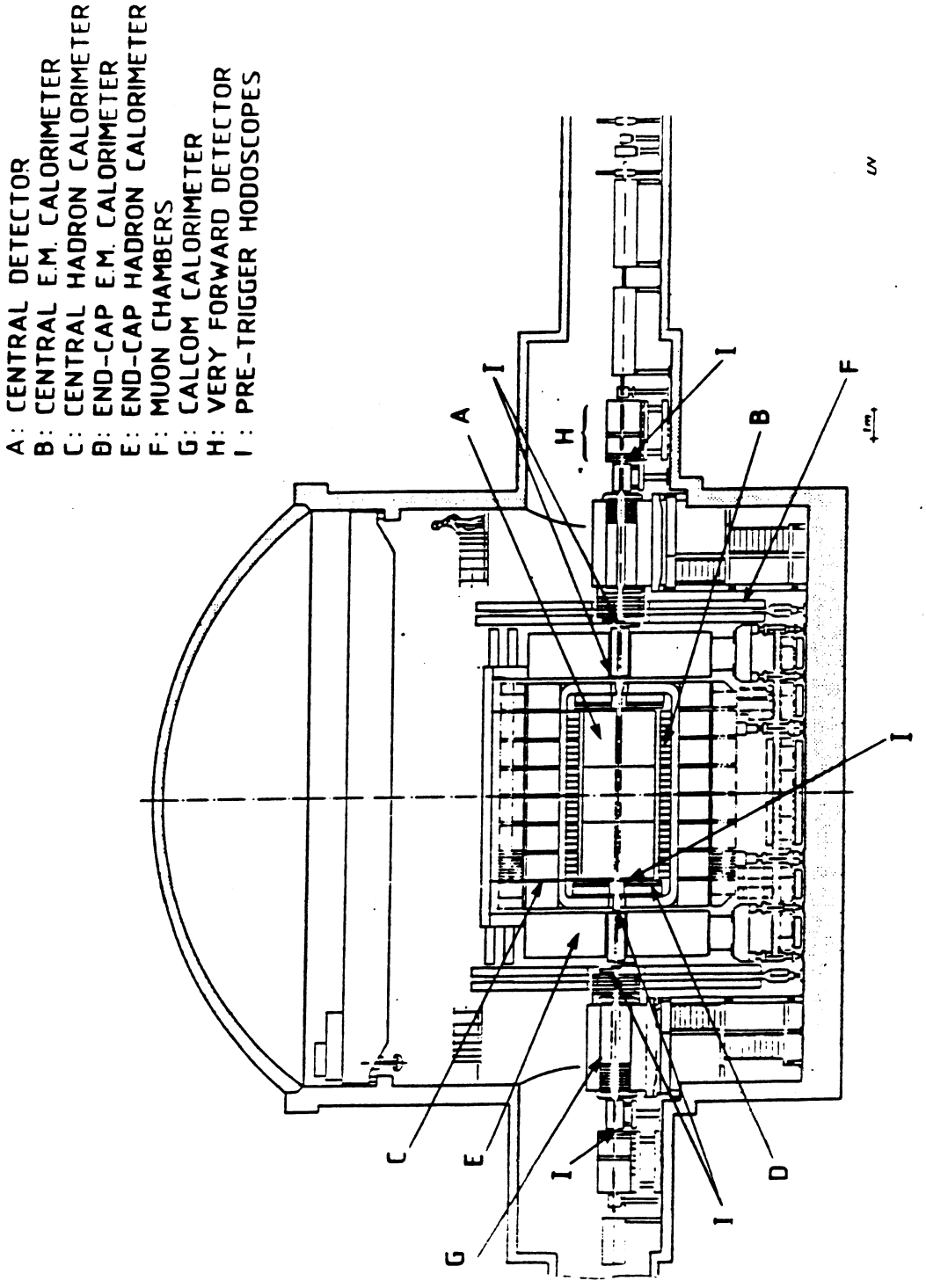

Figure 3.1 Section through the UA1 apparatus.

muon chambers also acts as an additional filter to remove as many hadrons as possible.

The UA1 co-ordinate system is chosen such that the collision point is defined to be $(x, y, z) = (0, 0, 0)$. The positive x-axis points along the direction of the incoming antiproton beam and the polar angle θ is defined w.r.t. this axis. The y- and z-axes form the plane in which ϕ, the azimuthal angle, is defined, $\tan\phi = y/z$, with the positive z-axis pointing along the direction of the horizontal magnetic field and the positive y-axis pointing vertically upwards. This is illustrated in Figure 3.2. We also define a quantity η, known as pseudorapidity, where $\eta = -\ln\tan\theta/2$, θ being the polar angle. So in Figure 3.2, $\theta = 25^0(155^0)$ corresponds to $\eta = 1.5(-1.5)$ units of pseudorapidity.

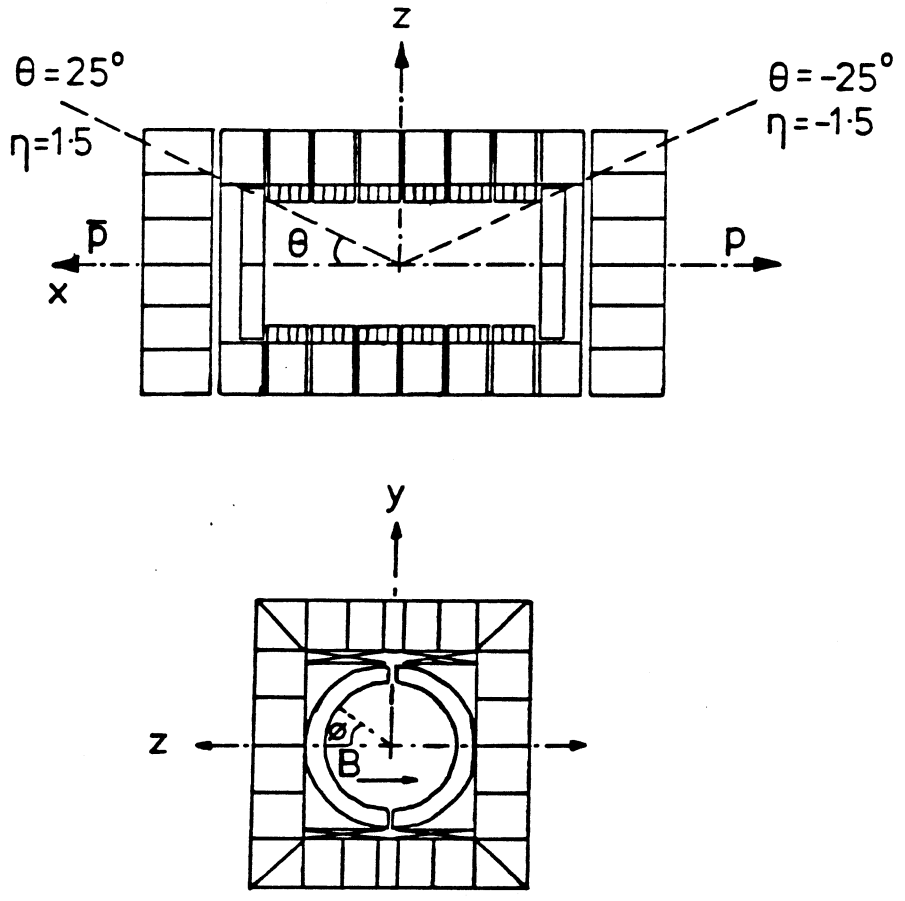

Figure 3.2 The UA1 co-ordinate system.

3.2 The Central Detector

The Central Detector, or CD, is at the heart of the experiment and is a cylindrical drift chamber with image readout[43]. It is 6 metres long with a diameter of 2.7 metres and is divided into 6 half-cylinders, three above and three below the beam-pipe (Figure 3.3). Some relevant parameters relating to the chamber design are given in Table 3.1.

The wire arrangement within a drift cell is illustrated in Figure 3.4. The field wires are arranged so that the drifting electrons cannot cross the wire plane and so avoids any left/right ambiguity. There are two types of chamber, the two central chambers where the wire planes are arranged vertically, and the four forward chambers where the orientation is horizontal. This arrangement is chosen so that the drift-direction which is the most accurately measured co-ordinate is the major component in the measurement of the sagitta of a track.

In the x-y plane (the plane of bending) the co-ordinate is determined from the wire number and position plus the drift time which is measured by a TDC (time-to-digital converter) interpolator with a 4 ns accuracy. The z co-ordinate (along the wire) is determined using charge division. The two pulses obtained from the z-measurement can also be used to determine dE/dx for a track and so provide particle identification for tracks with $p \leq$ 2 GeV.

For any particular wire, several tracks may cross the sensitive drift volume, each one generating a pulse at a different time. The image readout, which is based on Flash ADCs (analogue-to-digital converter), allows a complete picture of what happens during the 4 μs drift time. For each slice of 32 ns the left and right signal amplitudes of each wire are recorded. To record all this information would require approximately 256 bytes/wire, a total of 2 Mbytes/event. So the data is compacted (e.g., empty 32 ns bins are skipped) using on-line microprocessors known as ROPs (Read Out Processor). The wires are readout in groups of 12 using CTDs (charge and time digitizer) and each ROP operates on five of these groups, making a total of 110 ROPs operating in parallel.

In order to obtain accurate measurements from the detector the drift velocity, drift angle, absolute reference time t_0 and absolute wire postion must be known,

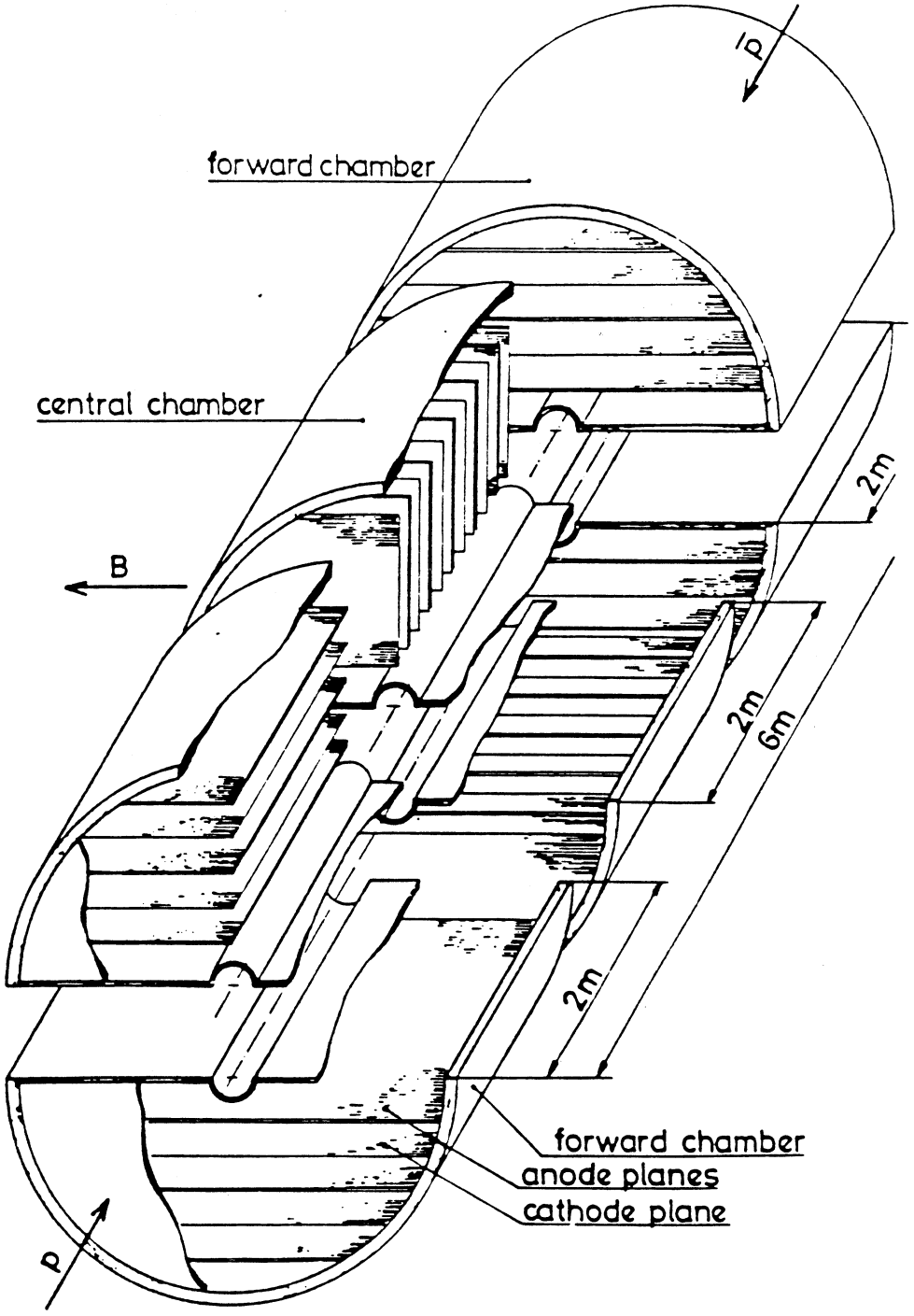

Figure 3.3 The UA1 Central Detector.

Gas mixture	40% Argon 60% Ethane
Electric field	1.5 kV/cm
Magnetic field	0.7 Tesla
Drift gap	18 cm
Drift angle	23^0 for B=0.7 T
Drift velocity	53 μm /ns
Sense wire spacing	1 cm
Sense wires in drift volume	175 (Forward) 80 (Central)
Drift volumes	46
Total number of sense wires	6250

Table 3.1 Main parameters of the Central Detector.

as well as the variation between drift volumes and between chambers. The entire central detector requires 50,000 calibration constants and these are obtained by processing of raw data, a process which is repeated every 24 hours while the experiment is taking data. Direct monitoring is provided by an on-line test pulse system which allows regulation wire-by-wire, for example, the different propagation times of the pulse along a wire can be used to adjust the t_0 of that wire.

The most accurately measured co-ordinate is the drift-time, with an overall spatial resolution of approximately 290 μm. The resolution on the charge division co-ordinate is typically $\sim$ 2% of the wire length. This leads to a $\pm$20% error on a 1m long track at p =40 GeV in the plane normal to the magnetic field. The two-track resolution (obtained from the minimum time separation between hardware pulses) is about 1.5 cm. This can be reduced to approximately 5 mm by the software detection in the ROPs of additional pulses. However, the error on the start time of the second pulse is 4 times larger and the z-measurement is bad for both pulses.

The track-finding efficiency in minimum bias events is 97% but this reduces for high multiplicity events and within collimated jets. This number has been ver-

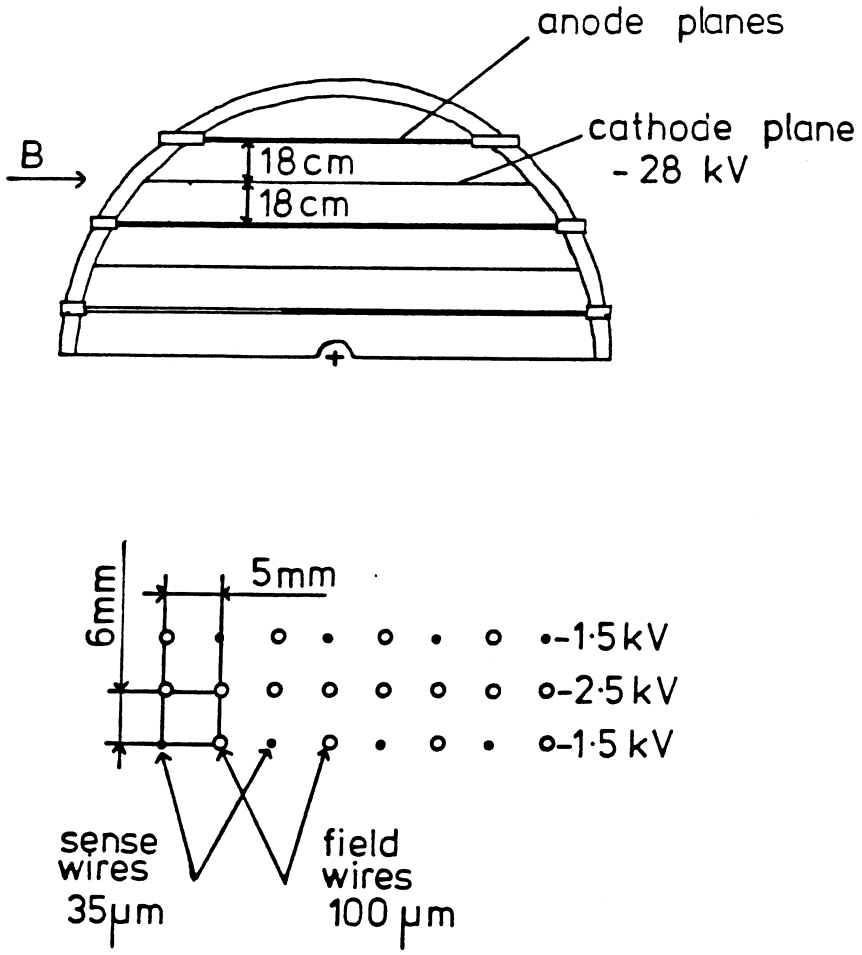

Figure 3.4 The wire arrangement within a drift cell.

ified by scanning events on the Megatek, an interactive computer-driven graphics facility which enables detailed study of individual events. Facilities include the ability to rotate events and access large amounts of detailed information about a particular event.

3.3 The Electromagnetic Calorimeter

The central electromagnetic calorimeter[44] has 48 cells known as gondolas because of their shape, as shown in Figure 3.5. The main parameters of the calorimeter can be found listed in Table 3.2.

The scintillation light, whose wavelength is 380 nm, is absorbed by BBQ wavelength-shifter, which covers both sides of each cell, and re-emitted at 480 nm

and then transmitted to the photomultipliers via light-guides. Each of the four samples in depth is viewed by four photomultipliers located outside the magnet. Each PM has two amplifiers at its anode. The first one supplies input to two ADCs, one with high gain, the other low gain to allow for a wide momentum spectrum of particles. The second integrates the pulse and is used in the trigger logic.

Light attenuation is used to determine the position of the deposited energy within a cell. Pairing the top and bottom PM's yields an x-position which has a resolution of $\delta x(\text{cm}) = 6.3/\sqrt{E}$, while pairing the left and right PMs provides a ϕ-position with a resolution of $\delta\phi(\text{rad}) = 0.3/\sqrt{E}$. A χ^2-fit per sampling is then performed to find the best position. In the case of multihits the ϕ and x measurements represent an energy centroid. For an isotropic event this centroid will not be very well determined while for a jet event it will be quite reasonable. In the case of single high P_T electrons we can also make a straight line fit through the samplings using the CD track momentum.

The overall energy resolution of the gondolas is presently $\delta E/E = 0.20/\sqrt{E}$. This is slightly worse than the original $\delta E/E = 0.15/\sqrt{E}$ because of ageing of the scintillator due to radiation damage.

The end-cap calorimeter, or bouchon, shown in Figure 3.5 consists of 64 radial 'petals', 32 at each end with each petal divided into four samplings in depth. Again, BBQ wavelength-shifter is used to transmit the light to the photomultipliers, each sampling having one photomultiplier. The attenuation length is chosen to match the variation of $\sin\theta$ over the radius of the calorimeter so the bouchons measure E_T rather than E.

After the first 11 radiation lengths there is a position detector formed of two layers of orthogonal proportional tubes of 2×2 cm^2 cross-section which measures the shower position and energy with a resolution of $\sigma_y = \sigma_z = 2$ mm.

Reconstruction in the bouchons involves both petal and position detector information. First clusters are found in the position detector and then matched using current division. Then clusters are associated to each petal and the barycentre of all clusters is found, which yields an average radius $\bar{r}$ and azimuthal position

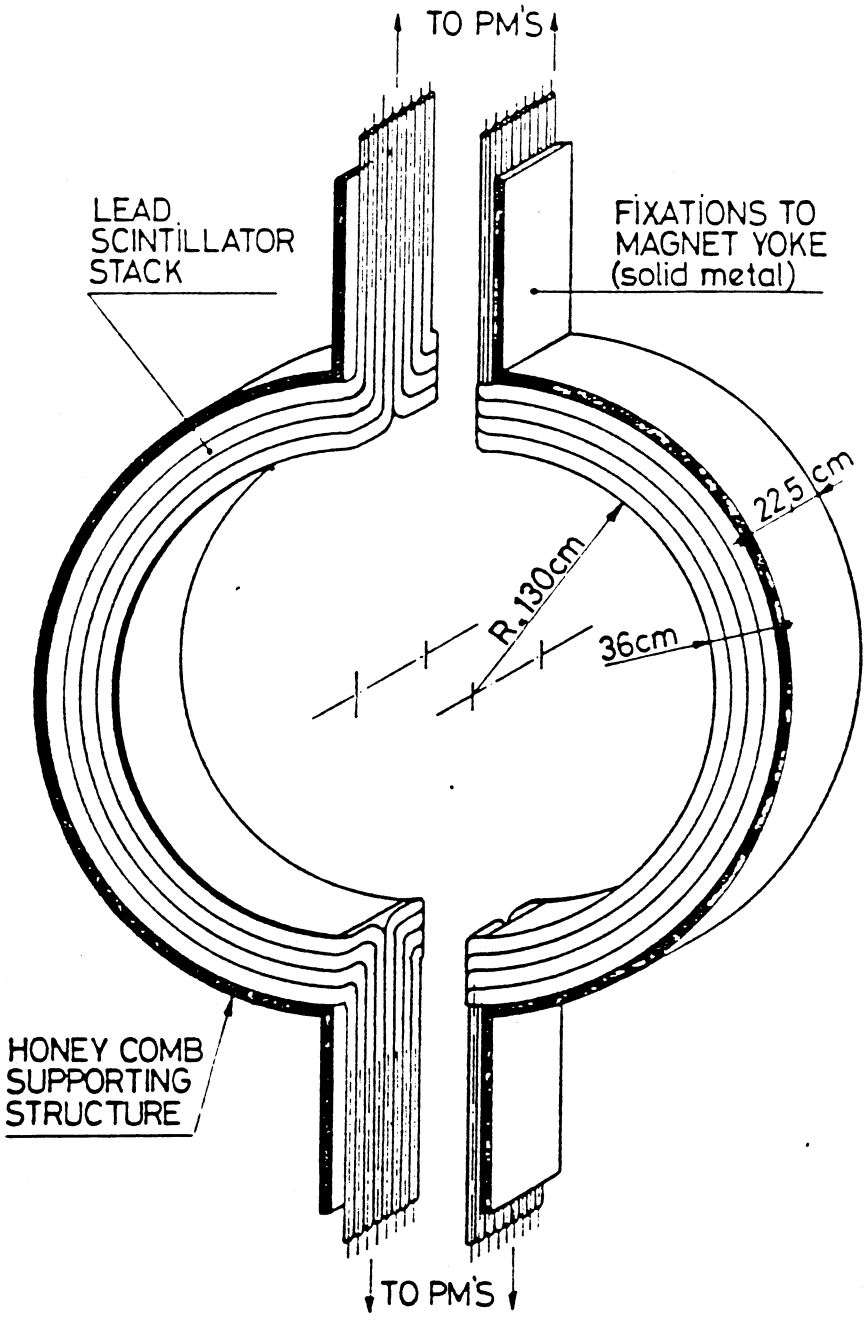

Figure 3.5 The Central Electromagnetic Calorimeter – Gondolas.

$\overline{\phi}$ for a given petal. We can then estimate the petal energy from $\overline{r}$ and the attenuation maps for each sampling.

For a single shower the resolution is $\delta E/E = 0.20/\sqrt{E_T}$ and the angular resolution is equal to the angular spread of one petal, i.e., 11^0. In the case of multihits the resolution is less accurate, especially in the case of isotropic events.

	Gondolas	Bouchons
Lead plate thickness	1.2 mm	4 mm
Scintillator thickness	1.5 mm	6 mm
Cell size ($\Delta\eta \times \Delta\phi$)	0.1×180^0	1.5×11^0
Number of cells	48	64
Thickness at normal incidence	26.4 $X_0/1.1\lambda$	26.7 $X_0/1.2\lambda$
Number of depth samplings	4(3.3/6.6/9.9/6.6 X_0)	4(3.6/7.2/8.7/7.2 X_0)

Table 3.2 Main parameters of the electromagnetic calorimeter.

As with the central detector, good calibration is important to obtain accurate energy measurements. This is achieved by several methods. Unfortunately it is not possible to place the calorimeter elements in a test beam so instead we use a 7 Curie Co^{60} source which emits 1 MeV γ-rays. This can be aimed at each cell in turn and is steerable by remote control. To obtain the absolute calibration of each cell the response to the Co^{60} source is compared to the response of a test module to a γ-source from an electron beam of higher energy. This also provides a complete attenuation map of the whole calorimeter. Two source calibrations are made, one at the beginning of a data-taking period and another at the end. During the course of a run a laser system is used to adjust the photomultiplier gains. The laser system is in turn monitored by an Am^{241} source and photodiodes. Careful monitoring is important because ageing of the scintillator causes the energy detected to decrease and so the calibration constants must be adjusted accordingly.

3.4 The Hadron Calorimeter

Surrounding the e.m. calorimeter is the hadron calorimeter[45], which is also the return yoke for the magnet and serves as a filter for the muon chambers. The main features are summarised in Table 3.3.

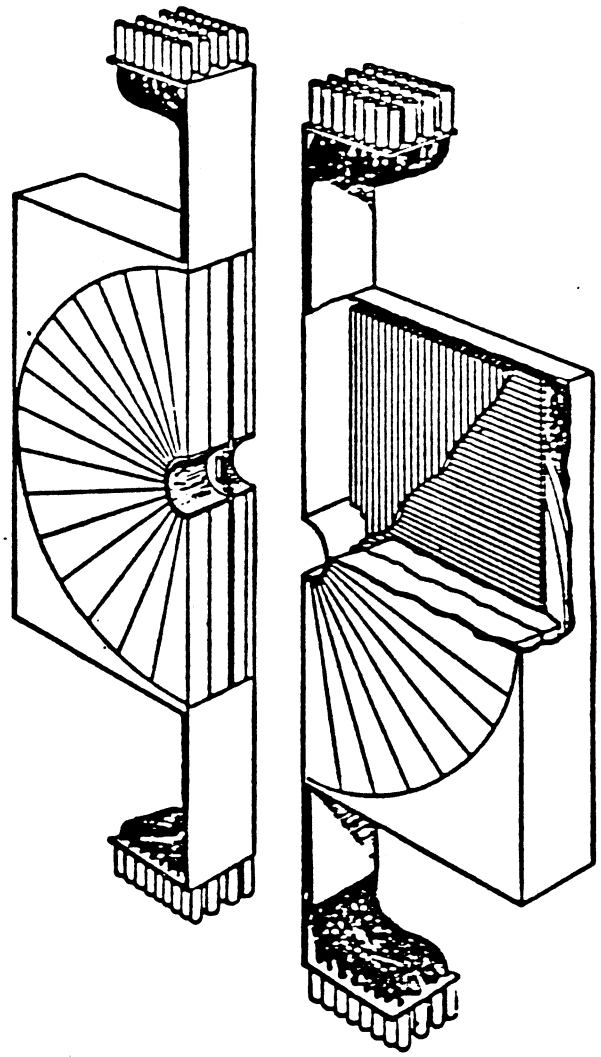

Figure 3.6 The End-Cap Electromagnetic Calorimeter – Bouchons.

There are 16 C modules, 8 on each side of the beam pipe, and one of these modules is shown in Figure 3.7. The scintillator sheets are read out from two opposite edges via BBQ wavelength-shifter bars. These absorb scintillation light at 420 nm and re-emit at 480 nm. The light is then taken from diagonally opposite corners and transmitted through light-guides to the photomultipliers which are situated on the outside of each module. The PM signals are then digitized using a 12-bit Lecroy ADC.

Each C-module is divided into 12 azimuthal sections, each with two samplings in depth and each sampling , or stack, is viewed by two photomultipliers. The

	C's	I's
Iron plate thickness	5 cm	5 cm
Scintillator thickness	1 cm	1 cm
Cell size ($\Delta\eta \times \Delta\phi$)	0.3×15^0	0.4×15^0
Number of cells	232	128
Thickness at normal incidence	5.0λ	7.1λ
Number of depth samplings	2	2

Table 3.3 Main parameters of the hadron calorimeter.

differing amount of light seen by each of the PMs allows us to determine the centroid of the energy deposition for each of the samplings.

The I's consist of 6 vertical sections at each end of the detector. Each end is segmented into 36 stacks with the 16 nearest the beam being further subdivided into four smaller stacks. The large stacks have the same readout as the C's but the small stacks have only one BBQ bar and are readout by one PM. Again, each stack has two depth samplings and the total thickness of iron is greater to allow for the more energetic forward-going particles.

For the large I's it is possible to determine the centroid of the energy deposition but for the small I's this is not possible and so the energy deposition is placed at the centre of the cell.

Monitoring and calibration is carried out by means of a fibre optics system and UV pulses from a nitrogen laser of wavelength 337 nm. Quartz fibres of 200 μm diameter carry the light to the centre of each plate and the light intensity is calibrated using reference scintillation counters. The measurements are cross-checked using cosmic ray muons and source measurements are performed on accessible stacks using an Ru^{106} source. The energy resolution obtained is $\sigma/E = 80\%/\sqrt{E}$ for both the C's and the I's.

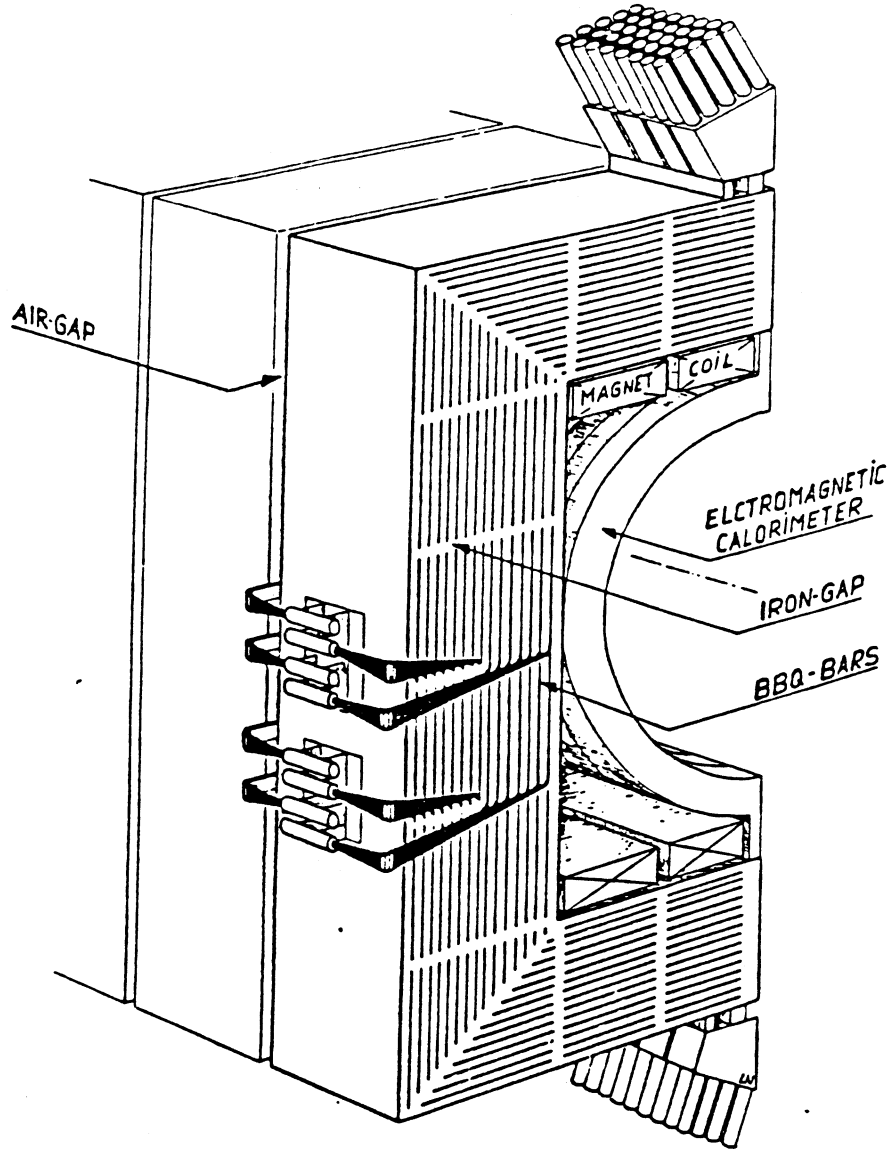

Figure 3.7 The Central Hadronic Calorimeter – C's.

3.5 The Forward Detectors

There are three detectors which extend coverage to within 0.2^0 of the beam. The Calcom calorimeter covers the region $0.7^0 < \theta < 5^0$ and $175^0 < \theta < 179.3^0$ and has an electromagnetic section made of a lead/scintillator sandwich divided into four samplings, each 7.5 radiation lengths deep with a position detector after the first sampling. The hadronic section is an iron/scintillator sandwich with six depth samplings, a total of 10.2 interaction lengths. The Calcom is also a

magnet and compensates for the beam displacement caused by the dipole field of the main magnet.

The very forward detector is the closest to the beam, extending from $0.2^0 < \theta < 0.7^0$ and $179.3^0 < \theta < 179.8^0$, and has a lead/scintillator electromagnetic portion and an iron/scintillator hadronic section.

Located in the I's surrounding the beam-pipe are the end-cap chambers. These are trapezoidal in cross-section with one chamber above the beam-pipe and the other below and have a range of $1^0 < \theta < 5^0$ and $175^0 < \theta < 179^0$. There are two sense wire planes and the drift-time and charge division along the wire are used to obtain the spatial co-ordinates of a track.

3.6 The Muon Chambers

Surrounding the entire experiment are two layers of drift chambers used for the detection of muons[46]. There are a total of 50 chambers, each 4×6 m and consisting of two orthogonal layers of drift tubes made of extruded aluminium filled with an argon/ethane gas mixture. Each of the 5180 sense wires is connected to a charge-sensitive amplifier followed by a voltage- sensitive one and then the signal output to a multitime digitizer (MTD) which has a precision of $\sim$ 8 ns. The resolution of the chambers is about 300 μm.

The two layers of chambers permit defintion of a track pointing to the vertex within a specified cone of aperture $\pm$ 150 mrad. The muon fast trigger is used to filter the pattern of the tube hits. This is carried out less than 1 μs after the maximum drift time which is well within the time between bunch crossings so there is no deadtime.

The additional magnetized iron shielding is also instrumented for muon detection using plastic limited streamer tubes (Iarrocci chambers) with cathode strip readout and filled with isobutane gas. These were only partially operational during the 1984 Collider run.

3.7 The Pretrigger

The purpose of the pretrigger[47] is to provide a $p\bar{p}$ interaction trigger, or in otherwords, a minimum bias physics trigger while at the same time removing as much of the background such as beam-gas collisions and cosmic- rays as possible. It is formed of five sets of scintillation hodoscopes located at increasing distances from the interaction point (see Figure 3.1).

The arrival of the proton and antiproton bunches is signalled by directional couplers, positive pick-up coils which are sensitive to charged particles travelling in one direction, situated 20 m upstream from the interaction point. This signal arrives 50 ns before any of the hodoscope signals and has an accuracy of $\sim$ 1 ns relative to the true time of the bunch crossing. The reference time is taken from the proton coupler signal and is referred to as the Machine Crossing signal (M/C). It is used to generate a beam crossing gate for the discriminators on the hodoscope photomultipliers.

Coincidences are then formed for each hodoscope and we require at least one counter to fire in each arm. At a luminosity of 3×10^{29} cm^{-2} s^{-1} the rate recorded by the SPS hodoscope, an array of counters mounted on the front of the Calcom calorimeter, is $\sim$ 12000 Hz with a corresponding pretrigger rate $\sim$ 10500 Hz. The SPS hodoscope also scales coincidences as a measure of the beam quality, for example measuring the proton and antiproton beam-gas rates.

The efficiency of the pretrigger is 96 % of the inelastic cross-section. This figure is determined by triggering only on the machine crossing signal and then scanning the events on the Megatek and for genuine events (i.e. not cosmic rays, or beam-gas) asking whether or not the pretrigger fired.

3.8 The Calorimeter Trigger

At a luminosity of 3×10^{29} cm^{-2} s^{-1} the 10500 pretriggers per second result mainly in low P_T events and the purpose of the calorimeter trigger[47] is to select those events which are sufficiently interesting to be recorded permanently on magnetic tape.

3.7 The Pretrigger

The purpose of the pretrigger[47] is to provide a $p\bar{p}$ interaction trigger, or in otherwords, a minimum bias physics trigger while at the same time removing as much of the background such as beam-gas collisions and cosmic- rays as possible. It is formed of five sets of scintillation hodoscopes located at increasing distances from the interaction point (see Figure 3.1).

The arrival of the proton and antiproton bunches is signalled by directional couplers, positive pick-up coils which are sensitive to charged particles travelling in one direction, situated 20 m upstream from the interaction point. This signal arrives 50 ns before any of the hodoscope signals and has an accuracy of $\sim$ 1 ns relative to the true time of the bunch crossing. The reference time is taken from the proton coupler signal and is referred to as the Machine Crossing signal (M/C). It is used to generate a beam crossing gate for the discriminators on the hodoscope photomultipliers.

Coincidences are then formed for each hodoscope and we require at least one counter to fire in each arm. At a luminosity of 3×10^{29} cm^{-2} s^{-1} the rate recorded by the SPS hodoscope, an array of counters mounted on the front of the Calcom calorimeter, is $\sim$ 12000 Hz with a corresponding pretrigger rate $\sim$ 10500 Hz. The SPS hodoscope also scales coincidences as a measure of the beam quality, for example measuring the proton and antiproton beam-gas rates.

The efficiency of the pretrigger is 96 % of the inelastic cross-section. This figure is determined by triggering only on the machine crossing signal and then scanning the events on the Megatek and for genuine events (i.e. not cosmic rays, or beam-gas) asking whether or not the pretrigger fired.

3.8 The Calorimeter Trigger

At a luminosity of 3×10^{29} cm^{-2} s^{-1} the 10500 pretriggers per second result mainly in low P_T events and the purpose of the calorimeter trigger[47] is to select those events which are sufficiently interesting to be recorded permanently on magnetic tape.

The 2440 calorimeter PMs are summed to form 288 trigger channels, 136 electromagnetic and 152 hadronic. The signals from these 288 channels are digitized by 8 bit ADCs which allow energy from a few hundred MeV up to 50 GeV to be measured.

For most of the triggers used we require the transverse energy (E_T) in a trigger channel so the energy must be multiplied by the sin θ weight for that channel. There are two identical digital processors each containing a series of RAMs. Each RAM is loaded with a look-up table which converts to energy or E_T. It is possible to compute both energy and transverse energy, one in each processor but to date both have been used to compute transverse energy.

All adjacent pairs of electromagnetic channels are then added with each channel being used twice – this forms the basis of the electron trigger. Also the hadronic channels (again each channel is used twice) are added to the electromagnetic to form blocks of hadronic energy and then the adjacent blocks are summed. These are fairly large due to the different geometries. In the central calorimetry a block consists of two C's and the 8 gondolas in front and in the end-cap a quadrant of 8 petals and 16 I's. These clusters are then passed through two sets of comparators which signal whether programmed levels have been exceeded. These are then passed to clustering and multiplicity logic and allow us to form electron and jet triggers. We can also add the 20 hadronic clusters to form the total transverse energy which is also passed through comparators for triggering.

Each processor can make eight decisions based on multiplicity and thresholds (two e.m. and two hadronic) and four based on total E_T. The final level logic allows each of these eight signals and any four of the 16 external bits (e.g. signals from the muon fast trigger) to be used in 24 logical combinations or triggers. The 24 combinations are OR'd together to form a signal which is sent to the data acquisition or to the 168 emulators which are described below.

In order to have <10% deadtime the rate from the processors must be $\leq$ 10 Hz. At a luminosity of 3×10^{29} cm^{-2} s^{-1} the rate from the processor is 5-6 Hz.

3.9 The 168 Emulators

The rate from the first level trigger described above is still too high and has to be reduced to about 3 Hz which is the tape writing speed. This is achieved with a series of six IBM 168 emulators, one for monitoring and display histograms and the other five for event selection.

In 1983 these were used only to flag those events of special interest, possible W,Z candidates, but in 1984 they were actually used to reject events in order to achieve tape writing rate. Of the events passed by the first level processors about 60% are rejected and the other 40% are accepted, a rate of $\leq$ 4 Hz.

In an event the triggering elements are reconstructed using algorithms very similar to those used in the offline programs using up-to-date calibrations. It takes $\sim$ 500 ms to process a calorimeter trigger and $\sim$ 150 ms for a muon trigger. Some 5% of the events are flagged as being of special interest and are also written onto special tapes. These are processed immediately – the so-called 'express-line'– and a selection of the events are scanned on the graphics facility to check that the apparatus is functioning correctly and the data is of good quality.

3.10 Data Acquisition

The UA1 data acquisition system (DAS) is based on two identical computer systems, a NORD 100 processor front-ending a NORD 500 processor. The 'A' machine runs the main data acquisition along with some limited monitoring programs while the 'B' machine runs the main monitoring programs and also allows the running of offline jobs to check in more detail on the performance of the detector.

The data is fed to the NORD via REMUS which is a system that allows an experiment to have many CAMAC branches. At present the readout of the experiment is being changed from CAMAC to VME, a system based on the 68000 microprocessor.

4. TWO-JET PRODUCTION

The leading order QCD $2 \rightarrow 2$ scattering cross-section formulae give us predictions about the shape of the angular distribution of the jet-jet pairs which we can test against experiment. An analysis of this type was first carried out by the UA1 Collaboration using data from the 1982 Collider run[48]. This analysis demonstrated that the angular dependence in $\cos\theta$ of the differential cross-section, $d\sigma/d\cos\theta$ was independent of x_1 and x_2, the scaled longitudinal momentum of the incoming partons and that this angular distribution was consistent with the form $(1-\cos\theta)^{-2}$. Also it was shown that the parton content of the proton could be described by an effective structure function $F(x)$ (see §2.3.7) with the shape being fitted by an exponential of the form $F(x) = 6.2\exp(-9.5x)$. The analysis was performed with limited statistics and therefore involved integrating over all masses of the jet-jet system and making complicated acceptance corrections.

Using the data from the 1983 and 1984 Collider runs we are now able to study the angular dependence of the differential cross-section for a fixed mass of the jet-jet system, i.e.,fixed c.m.s energy, $\sqrt{\hat{s}}$, and the increased statistics means that the complicated acceptance corrections applied to the 1982 data sample are no longer required.

4.1 Jet reconstruction

We are unable to observe bare partons, but instead detect the hadrons from the fragmentation of these partons and we therefore require some method of combining these hadrons into jets. The aim of any method of jet reconstruction is that the axis of the jet should reproduce the direction of the original outgoing parton and that the energy of the jet should be equal to that of the parton.

The results presented in this thesis are obtained using the standard UA1 jet-finding algorithm which is a geometrical algorithm. Other methods of jet-finding exist such as those using dynamical variables[49] and comparisons between these and the algorithm used here have been presented elsewhere[50].

A jet is defined as the vectorial sum of all the particles which fall within a cone in pseudorapidity-azimuth space (η-ϕ, where η and ϕ are defined in §3.1), centred on the highest transverse momentum particle, of radius ΔR where $\Delta R = \sqrt{\Delta\eta^2 + \Delta\phi^2}$ with $\Delta\eta = \eta_{jet} - \eta_{track}$ and $\Delta\phi = \phi_{jet} - \phi_{track}$ where $\Delta\phi$ is in radians. The justification for using a cone comes from the Sterman-Weinberg[51] definition of a two-jet event in e^+e^- annihilation as one where all but a fraction ϵ ($\epsilon \ll 1$) of the total energy in the event falls within two back-to-back cones of opening angle δ. The fraction of events f in which this happens increases as q^2 increases. Also the fragmentation of partons by gluon radiation and some form of Feynman-Field fragmentation means that the hardest tracks (highest momentum) "remember" the direction of the original parton. So we can place a cone around these hard particles and try to associate the softer particles within this cone.

The actual method used will be described here as it differs from that given in previous publications[52].

1. Each calorimeter cell is assigned an energy vector whose magnitude is given by the energy deposited in the cell and whose direction by the centroid of this deposition for the electromagnetic and central hadron calorimeter cells and the centre of the cell for the end-cap hadron calorimeter.
2. All cells with transverse energy ($E_T = E\sin\theta$) in excess of 1.5 GeV – the *initiator* threshold – are arranged in order of decreasing E_T.
3. The cell with the highest transverse energy initiates the first jet.
4. The next cell is added vectorially to the first if it is closer than $\Delta R = 1$, otherwise a new jet is initiated.
5. This procedure is repeated until all cells with $E_T > 1.5$ GeV have been associated to jets.
6. The cells with transverse energy less than 1.5 GeV are then added to the nearest jet if $\Delta R < 1$.

The final jet is given by the vectorial sum of all the cells in that jet. The a postiori justification for the choice of $\Delta R = 1$ comes from studying the transverse

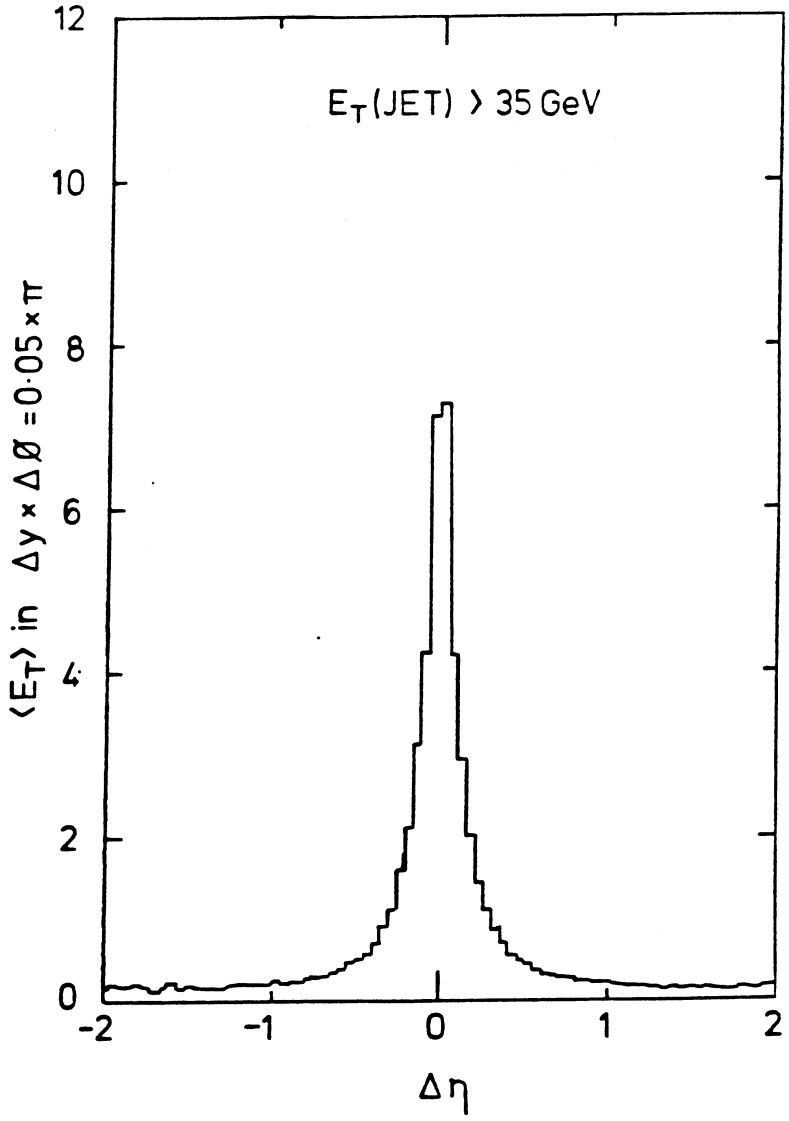

Figure 4.1 Jet energy profile.

energy flow about the reconstructed jet axis (Figure 4.1).

Low transverse energy jets are sensitive to the choice of the initiator threshold, if the threshold is raised from 1.5 GeV to 2.5 GeV then 62% of jets with $E_T < 12$ GeV are no longer reconstructed. As the jets we shall be dealing with have transverse energies well in excess of 12 GeV this is not a problem. Therefore changing initiator thresholds will not significantly change our data sample.

This method of jet-finding can be applied equally well to charged particle

tracks[53] but the analysis described here uses only jets composed of calorimeter cells as we are only interested in the energy of the jets and not their charged particle content.

The ISAJET Monte Carlo[54] was used to compare reconstructed jets and generated jets[55]. Monte Carlo events were passed through a complete simulation of the UA1 apparatus and then the jet algorithm was applied to these events. For each event the two reconstructed jets with the highest E_T were compared to the sum of the hadronic fragments from the two generated scattered partons before any final-state gluon radiation had occurred. One should note that comparing to the sum of the fragments is not strictly the same as comparing to the generated partons for the following reason. During fragmentation the hadronic fragments are given P_T relative to the original parton directions and hence the jets acquire mass and so fail to conserve energy exactly. Energy conservation is imposed after the event is generated by boosting the central jet system until it is at rest in the c.m.s of the colliding partons, rescaling all of the 3-momenta and recalculating the energies. Comparison of the reconstructed energy of the jet, E_{rec}, with the generated energy E_{gen} showed that

$$\left\langle \frac{E_{rec} - E_{gen}}{E_{gen}} \right\rangle = \left\langle \frac{\Delta E}{E_{gen}} \right\rangle \neq 0 \tag{4.1}$$

with typical values for $\langle \Delta E/E_{gen} \rangle \sim -0.2$, i.e., a 20% loss of energy between the reconstructed jets and the sum of the fragments from the scattered partons.

This energy loss can be divided into two parts, one due to the physics of the process and the other due to the UA1 apparatus with each contributing $\sim$ 10%. The first contribution to this loss is from soft gluon radiation which is emitted at wide angles and hence is not contained within the cone of the jet algorithm and also from low momentum particles from the fragmentation which are typically at large angles and are anyway difficult to assign to a particular jet. The second is due to uninstrumented gaps and dead material in the UA1 detector and losses due to the momentum dependent response of hadrons in the electromagnetic calorimeter.

η	ϕ	$-\langle\Delta E/E\rangle$	$-\langle\Delta P/P\rangle$	$\Delta\phi$
0.1	10^0	0.19	0.13	-1^0
0.1	80^0	0.34	0.27	-11^0
1.5	10^0	0.20	0.23	1^0
2.0	10^0	0.20	0.21	0^0

Table 4.1 Differences between generated and reconstructed quantities for a jet of $E_T = 40$ GeV.

The energy loss is found to be dependent on rapidity and azimuthal angle of the jet but over the range of transverse energies considered it is not strongly E_T dependent. The agreement between the reconstructed rapidity of the jet axis and the rapidity of the generated parton is found to be very good with $|\eta_{rec} - \eta_{gen}| \sim 0.01$. Jets whose axes fall close to the vertical gap between the two halves of the central e.m. calorimeter have their azimuthal position shifted towards the horizontal plane and also suffer greater loss of energy. In Table 4.1 are presented typical values for the shifts in energy, momentum and azimuth for a jet with transverse energy of 40 GeV placed at different rapidities. These corrections are parameterized in the form of a look-up table and then used to correct the jet 4-vectors.

4.2 Two-jet event sample

The results presented here are derived from two data samples, 100 nb^{-1} taken during the 1983 Collider run and 263 nb^{-1} collected during the 1984 Collider run For a detailed description of the collection and preparation of the data samples the reader is referred to Appendix A. The events selected from these two sets of data will be referred to as sample 1 and sample 2 respectively.

For each event we take the two highest transverse energy jets. The justification for using this procedure is as follows. The correction that is applied allows for any soft final-state gluon radiation which falls outside the jet cone so the presence of soft third jets is not too important. The presence of hard bremsstrahlung

poses more of a problem. One could argue that any hard third jet should be combined vectorially with the jet closest to it in η-ϕ space but this means that we have to be sure that the jet is a final-state radiation because clearly it would not be correct to include any initial-state radiation. As this is very difficult in practice we decide to only take *top two*. In this situation it turns out that normally the mass of the two-jet system is not sufficient to satisfy the mass cut applied. Only for three-jet events with very high mass do the top two jets still have a sufficiently high mass. For sample 1 there are 9 events which survive (0.7% of the two-jet sample) while the corresponding figure for sample 2 is 15 (1% of the two-jet sample). We therefore conclude that the angular distributions will not be significantly distorted and so taking the top two jets is a reasonable procedure to adopt.

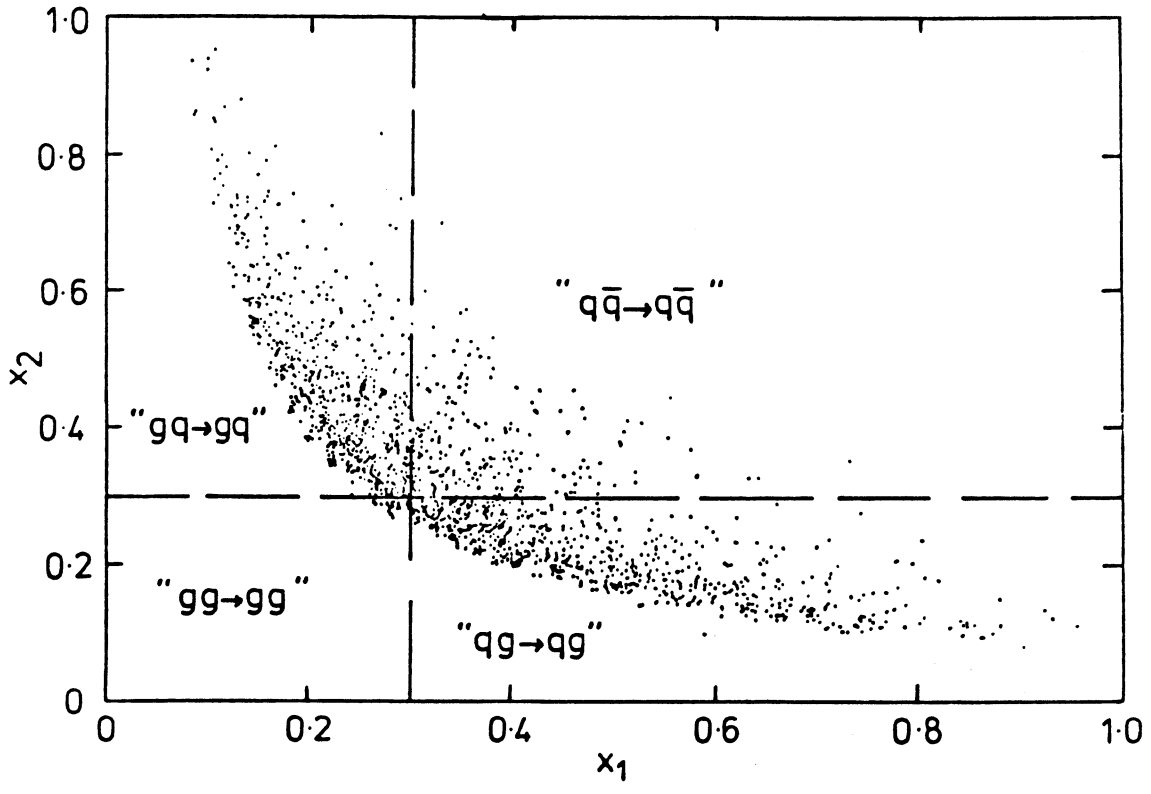

Figure 4.2 The raw x_2 vs x_1 distribution for sample 2.

Having chosen the top two jets in the event we make the assumption that

the jet axis as defined by the UA1 algorithm can be considered to represent the parton direction. The following kinematic quantities can then be defined, assuming the incoming partons are massless and collinear with the beams (the outgoing partons are not required to be massless)

$$\begin{aligned} x_1 &= \left[x_F + (x_F^2 + 4\tau)^{1/2}\right]/2 \\ x_2 &= \left[-x_F + (x_F^2 + 4\tau)^{1/2}\right]/2 \end{aligned} \tag{4.2}$$

with

$$\begin{aligned} x_F &= \left(p_{3_L}^{lab} + p_{4_L}^{lab}\right) / \left(\sqrt{s}/2\right) = x_1 - x_2 \\ \tau &= \frac{m_{2J}^2}{s} = x_1 x_2 \quad \text{where} \quad m_{2J}^2 = \left(p_3^{lab} + p_4^{lab}\right)^2 . \end{aligned} \tag{4.3}$$

The quantities x_1 and x_2 are the scaled longitudinal momentum of the interacting partons, and have laboratory 4-momenta $p_1^{lab} = (x_1\sqrt{s}/2, x_1\sqrt{s}/2, 0, 0)$, the antiproton parton, and $p_2^{lab} = (x_2\sqrt{s}/2, -x_2\sqrt{s}/2, 0, 0)$, the proton parton. The laboratory 4-momenta of the final state jets are given by p_3^{lab} and p_4^{lab} with $p_{3_L}^{lab}$ and $p_{4_L}^{lab}$ being the longitudinal components of 3 and 4 respectively. The variable x_F can be thought of as a measure of the longitudinal boost of the jet-jet system where $x_1 = x_2$ means the system is stationary in the laboratory frame but $x_1 > x_2$ or $x_2 > x_1$ means that the system is in motion, in the $+x$ direction or the $-x$ direction respectively. The quantity τ is the scaled invariant mass squared of the system. In Figure 4.2 is shown the raw x_2 versus x_1 distribution (no acceptance corrections) for sample 2 for events with m_{2J} >180 GeV. As can be seen it is now possible to reach quite large values of x_1 and x_2 at the Collider although the proportion of $q\bar{q}$ scattering is still fairly small, the data being dominated by qg scattering as indicated by the approximate breakdown of the contributions of the dominant subprocesses.

Having obtained x_1 and x_2 and hence p_1^{lab} and p_2^{lab} a Lorentz boost to the c.m.s of the final state jets 3 and 4 is then made. As a consequence of taking only the top-two jets, the jet-jet system in the laboratory may not be perfectly balanced but will have a residual transverse momentum which may be quite large as is illustrated in Figure 4.3 where we have plotted the raw k_T distribution for

both samples (no corrections for the effect of resolution have been made), where

$$k_T = \left((p_{3_y}^{lab} + p_{4_y}^{lab})^2 + (p_{3_x}^{lab} + p_{4_x}^{lab})^2 \right)^{1/2} . \tag{4.4}$$

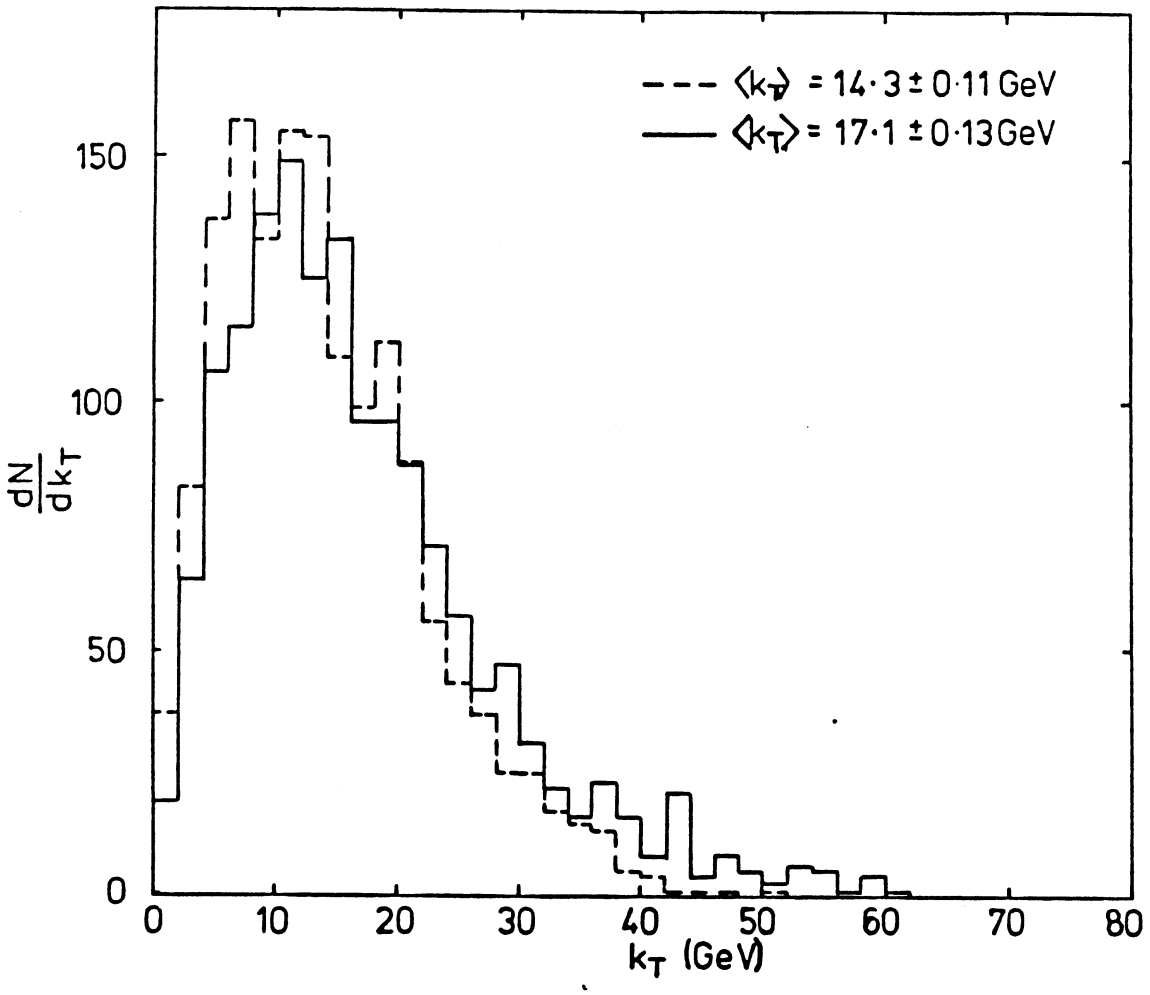

Figure 4.3 dN/dk_T **vs** k_T **for sample 1 (dotted line) and sample 2 (solid line).**

The mean value for sample 1 is 14.3 ± 0.11 GeV which is ~ 3 GeV lower than the mean of sample 2, reflecting the lower average mass of sample 1. The high mean values indicate that the distributions are dominated by resolution effects. This means the direction of the boost is no longer along the x-axis and hence the

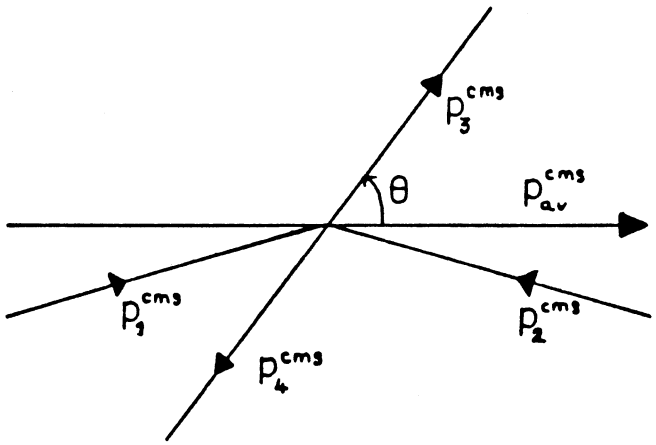

Figure 4.4 Explanation of average beam direction.

beam-beam axis is no longer collinear in the c.m.s. So an average beam direction is defined (Figure 4.4) which is the vector difference of the incoming partons in the c.m.s

$$(\mathbf{p}_1^{cms} - \mathbf{p}_2^{cms}) = \mathbf{p}_{av}^{cms} \tag{4.5}$$

as defined by Collins and Soper[56].

The c.m.s scattering angle θ is defined with respect to this direction, namely

$$\cos\theta = \frac{\mathbf{p}_3^{cms} \cdot \mathbf{p}_{av}^{cms}}{|\mathbf{p}_3^{cms}||\mathbf{p}_{av}^{cms}|} \tag{4.6}$$

where the dot products are between the 3-momenta and $\mathbf{p}_3^{cms}$ is the 3-momentum of jet 3. The software filter (Appendix A) has a fixed E_T threshold for the jets, meaning that a low mass event will satisfy the filter over a much smaller angular range than a high mass event. The aim is to use the widest possible angular range but still keep the jet-jet mass as low as possible. To achieve this compromise we make a fiducial cut on θ of $|\cos\theta| < 0.8$ and a mass cut of 150 GeV (sample 1) or 180 GeV (sample 2). The higher threshold for sample 2 arises because of the higher jet threshold used in the filter. Notice that the angular cut is dimensionless, enabling events with identical m_{2J} but taken at a different c.m.s

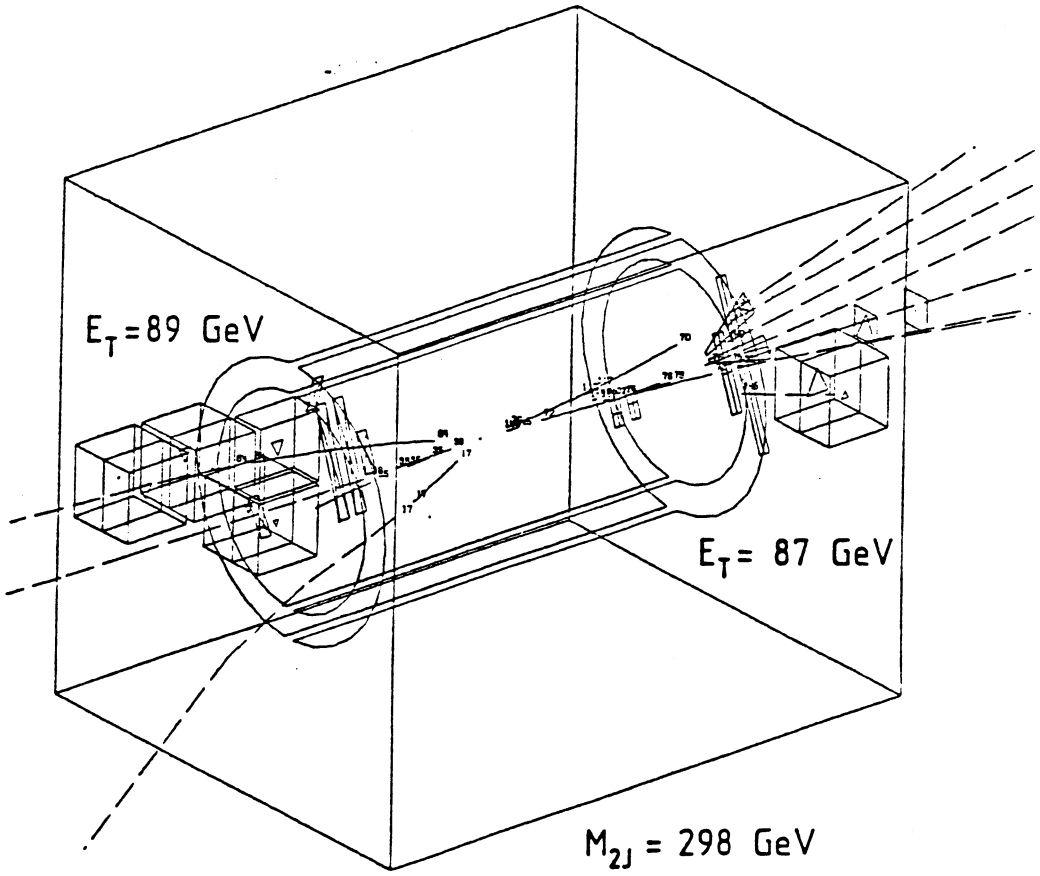

Figure 4.5 A typical two-jet event.

energy, namely 546 GeV or 630 GeV, to be compared directly. A typical event from sample 2 satisfying these requirements is shown in Figure 4.5.

As a check on the back-to-back nature of the two-jet sample we have plotted in Figure 4.6 the $\Delta\phi$ distribution of the jet pairs for sample 2 where

$$\Delta\phi = |\phi_1 - \phi_2|, \quad 360^0 \geq \phi_1, \phi_2 \geq 0^0. \tag{4.7}$$

As is clearly demonstrated by Figure 4.6 the jet pairs are indeed back-to-back with 98% of the sample having $\Delta\phi > 150^0$. We also compare the mass spectrums

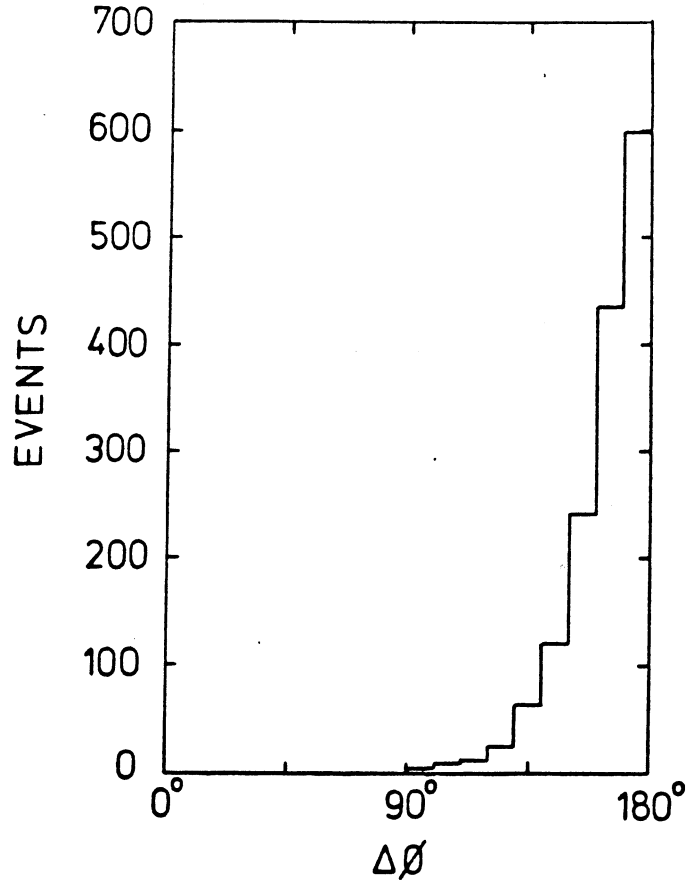

Figure 4.6 $\Delta\phi$ distribution for sample 2.

of the two samples in Figure 4.7, where the crosses are sample 1 and the full circles are sample 2, uncorrected for any effects due to acceptance or resolution. We have normalized sample 1 to sample 2 in the region of m_{2J} between 180 GeV and 250 GeV. The two spectrums are consistent with each other although sample 1 is slightly lower than sample 2 for masses above $\sim$ 210 GeV.

The resulting $\cos\theta$ distributions are plotted in Figure 4.8a for sample 1 – 1142 events over the mass range m_{2J} =150-250 GeV – and Figure 4.8b for sample 2 – 1449 events over the mass range m_{2J} = 180- 250 GeV. The theoretical curves in both figures (which have been normalized to the data) are obtained by integrating the leading order subprocess cross-sections ($\pi\Sigma/2$ from Table 2.1) bin by bin over the angular range $\cos\theta$ = 0.0 - 0.8, but ignoring any q^2 dependence of α_s, i.e., α_s = constant, namely perfect scaling. We compute the contribution to each bin of the three dominant subprocesses and then weight these numbers by the relative

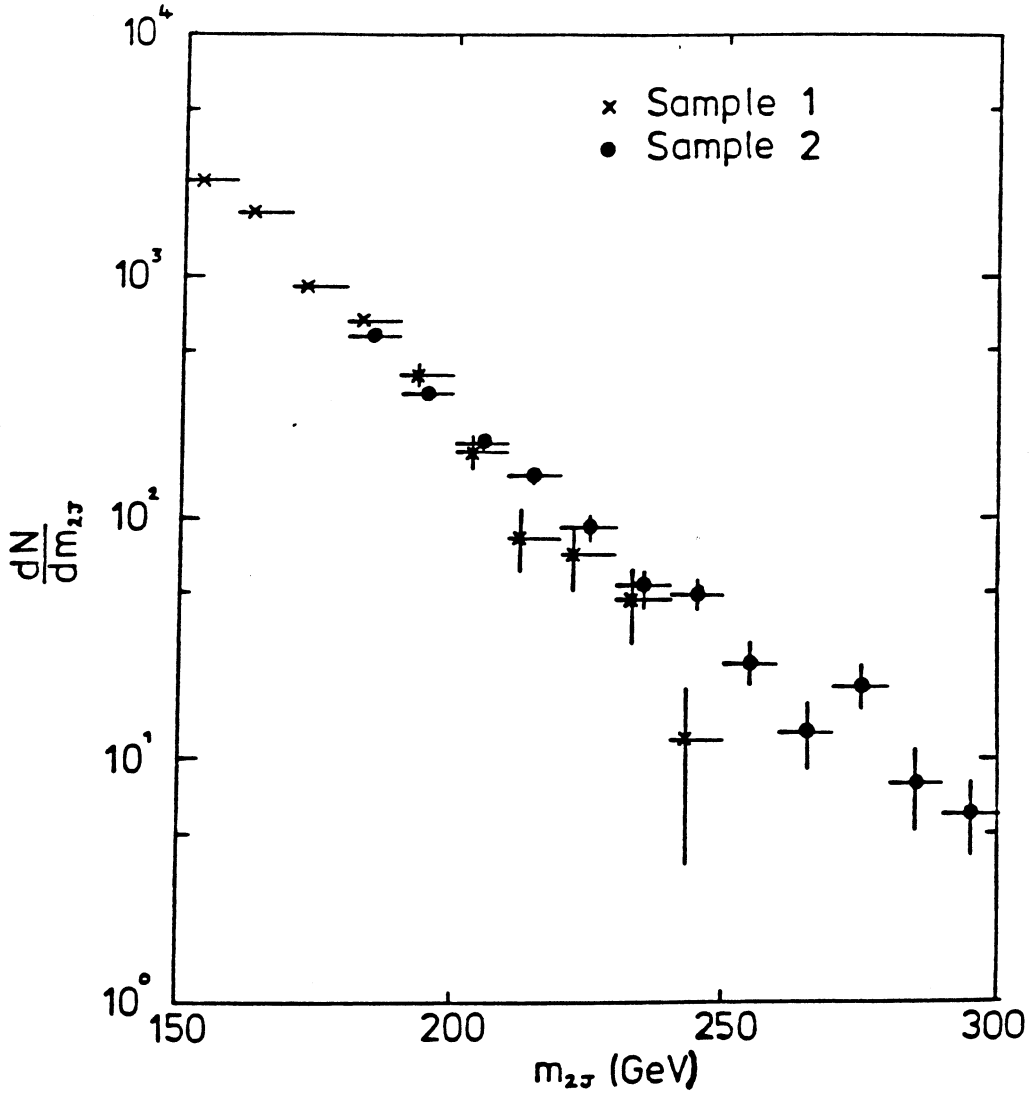

Figure 4.7 Uncorrected two-jet mass spectrum for sample 1 (crosses) and sample 2 (full circles).

contribution of each subprocess over the mass range under consideration. For masses of the jet-jet system between 150 GeV and 250 GeV these contributions are $gg : qg : q\bar{q} \equiv 12\% : 52\% : 36\%$. The curves clearly demonstrate that the data is consistent with the predictions of leading order QCD assuming perfect scaling, although it can be seen that there are observable differences between theory and experiment.

These deviations from the leading order scaling prediction become more apparent if the data is plotted in terms of a new variable χ, where

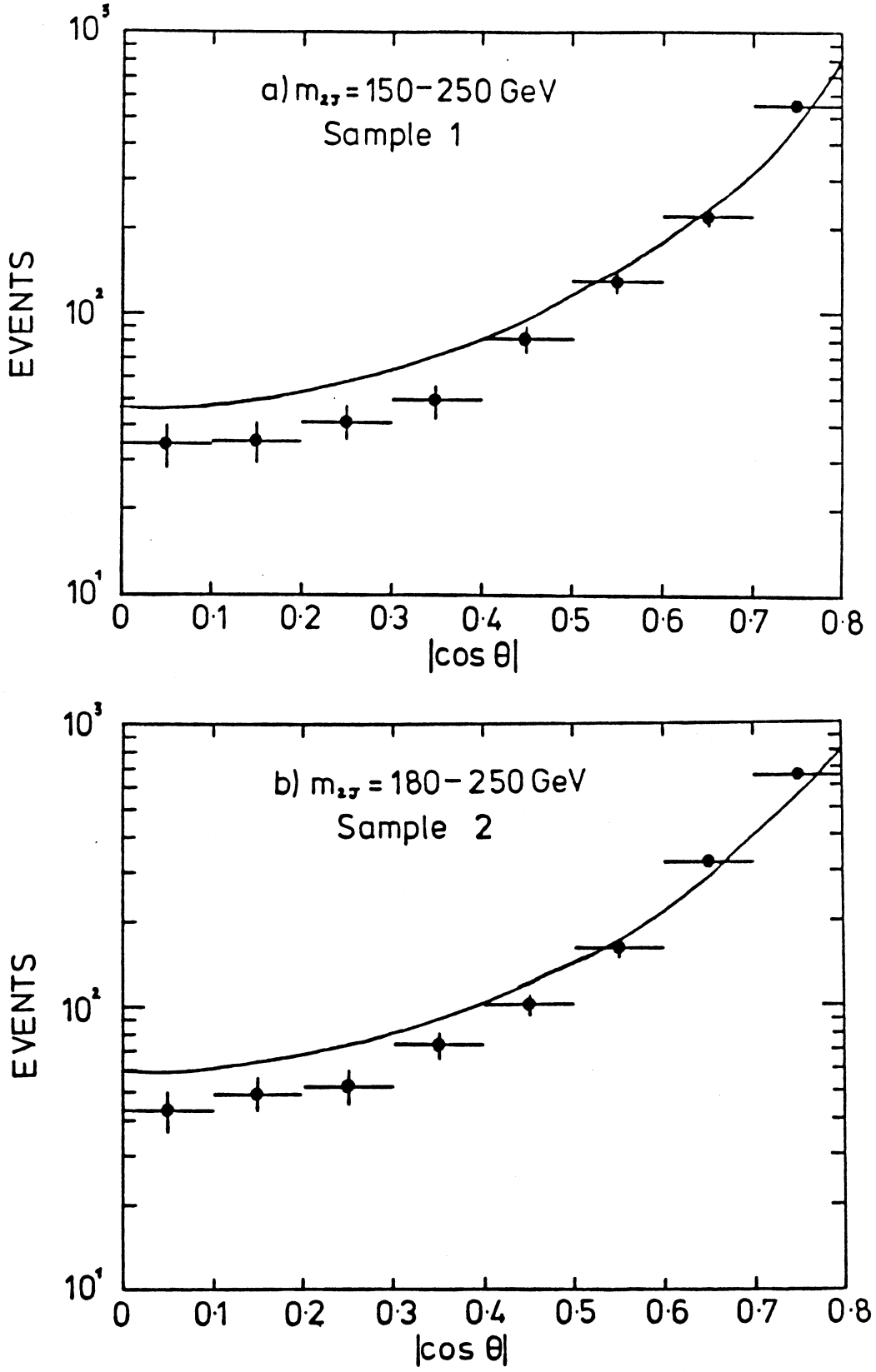

Figure 4.8 Uncorrected two-jet angular distribution in $|\cos\theta|$ for a) sample 1 and b) sample 2. For curves see text.

Parton Subprocess	$\Sigma = 4\hat{s}/\pi\alpha_s^2(1+\chi)^2\ d\sigma/d\chi$
$q_1q_1 \rightarrow q_1q_1$	$\frac{8}{9}\left[F(\chi) - \frac{1}{N}(\chi + 2 + \chi^{-1})\right]$
$q_1\bar{q}_1 \rightarrow q_1\bar{q}_1$	$\frac{8}{9}\left[F(\chi) + \frac{1}{N}(\chi - 1 + \chi^{-1}) + \frac{\chi^2+1}{(\chi+1)^2}\right]$
$qg \rightarrow qg$	$2\left[F(\chi) + \frac{4}{9}\left(\frac{1}{2}\chi + \frac{3}{2} + \frac{1}{2}\chi^{-1}\right)\right]$
$gg \rightarrow gg$	$\frac{9}{2}\left[F(\chi) + 2 - \frac{\chi}{(1+\chi)^2}\right]$

$$F(\chi) = \chi^2 + \chi + 1 + \chi^{-1} + \chi^{-2}$$

Table 4.2 Lowest order parton-parton cross-sections expressed in terms of χ.

$$\chi = \frac{(1+\cos\theta)}{(1-\cos\theta)} = \frac{\hat{u}}{\hat{t}} \tag{4.8}$$

as suggested by Combridge and Maxwell[57]. The leading order subprocess cross-sections of Table 2.1 can be written in terms of χ and the results for Σ (making the substitution $\hat{t} = -\hat{s}(1/\chi + 1)$ and $\hat{u} = -\hat{s}(\chi/1+\chi)$ in Table 2.1) are listed in Table 4.2 for the dominant subprocesses.

As was noted in §2.3.3 these subprocesses have a similar angular distribution in terms of $\cos\theta$ with $d\sigma/d\cos\theta \propto (1-\cos\theta)^{-2}$, from Table 4.2 we can see that in terms of χ the same is again true with

$$\frac{d\sigma}{d\chi} \propto \frac{F(\chi)}{(1+\chi)^2} \tag{4.9}$$

with $F(\chi)$ as given in Table 4.2. The $(1+\chi)^2$ term arises from the evaluation of

the Jacobian $d\cos\theta/d\chi$. Substituting values for χ into equation 4.9 yields the result that for $\chi > 2$, $d\sigma/d\chi \sim$ constant and for $\chi = 1$, $d\sigma/d\chi|_{\chi=1} \sim 1.5\, d\sigma/d\chi|_{\chi>2}$. This increase at small χ is due to the backward scattering component (u-channel exchange) for which the dominant contribution is χ^{-1} which of course falls as χ increases and so becomes less important compared to the forward scattering component χ^2 (t-channel exchange) which increases as χ increases.

The data is shown plotted as $1/N\ dN/d\chi$ versus χ in Figure 4.9a (sample 1) and 4.9b (sample 2) where the requirement of $\cos\theta < 0.8$ has become $\chi < 9$. The corresponding theoretical curves are the leading order scaling prediction, obtained by integration of the cross-sections in Table 4.2 and using the same mix of subprocesses as before. The deviations that were visible in Figures 4.8a and 4.8b are now quite noticeable, at large angles (χ = 1-2) the scaling curve rises well above the data and at small angles (χ = 7-9) it falls substantially below.

The explanation for this behaviour lies with the non-scaling nature of QCD, namely the q^2-dependence of the coupling constant $\alpha_s(q^2)$ and the structure function $F(x, q^2)$.

4.3 Non-scaling effects

In computing the theoretical curves of Figures 4.8 and 4.9 we have ignored the non-scaling behaviour of QCD and have effectively assumed that α_s = constant, but, as was discussed in §2.3.2, the value of the coupling constant does actually depends on the q^2 of the interaction. Unfortunately we do not know a priori what the definition of q^2 should be so a reasonable choice has to be made.

One such choice would be $q^2 = \hat{s}$, the subprocess c.m.s energy squared. It turns out that this is effectively identical to using the scaling approximation for the following reason. We are considering events which are at fixed mass and hence fixed $\hat{s}$ so that $\alpha_s(q^2 = \hat{s})$ will be a constant over the whole angular range ($\chi > 2$) and therefore the event rate will be a constant over this range, exactly the effect obtained in the scaling approximation and clearly not a good explanation of the data. For this reason $q^2 = \hat{s}$ does not seem to be a particularly good choice of scale.

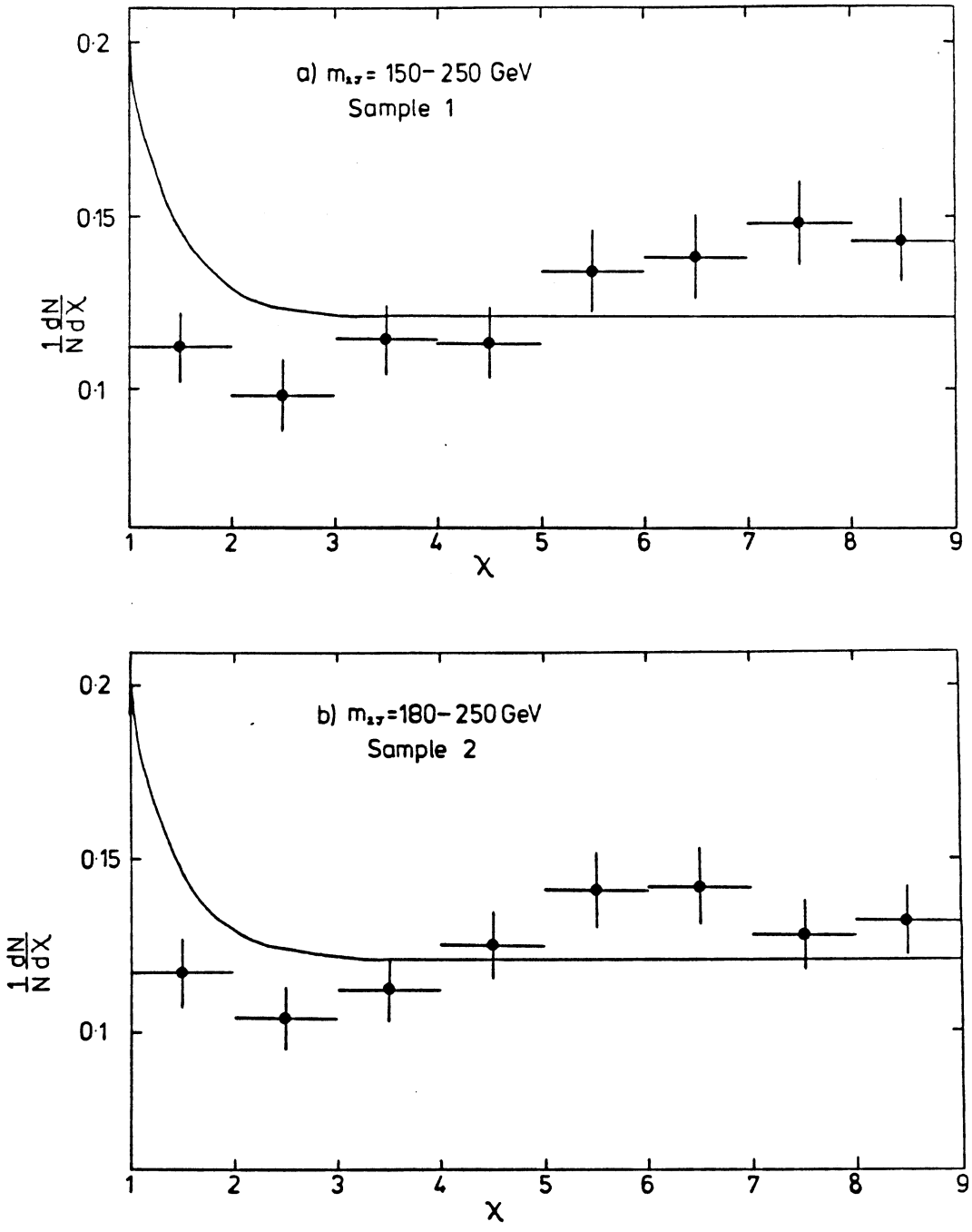

Figure 4.9 Uncorrected two-jet angular distribution in χ for a) sample 1 and b) sample 2. For curves see text.

Examination of the data shows that as χ increases (θ decreases) the event rate rises. As event rate is proportional to α_s^2 then as the scattering angle decreases α_s^2 must increase and hence q^2 must decrease. It therefore seems plausible that we can write $q^2 \rightarrow q^2(1 - \cos\theta)$, i.e., the scale q^2 is dependent on the c.m.s scattering angle. The simplest choice which has the required property is $-\hat{t}$, the 4-momentum transfer squared to the outgoing parton (c.f. deep inelastic scattering), where

$$q^2 = -\hat{t} = \frac{\hat{s}}{2}(1 - \cos\theta) \tag{4.10}$$

and this is the choice we shall adopt for the present.

In addition to the q^2-dependence of α_s there is also dependence on q^2 of the structure function $F(x, q^2)$. As q^2 increases the structure function "softens",in other words, the number of low x partons increases while the number of high x partons is reduced, as shown in Figure 4.10 where we plot the effective structure function $F(x, q^2) = G(x, q^2) + \frac{4}{9}Q(x, q^2)$ for five values of x using $G(x, q^2)$ and $F_2(x, q^2) \equiv Q(x, q^2)$, as measured by the Charm Collaboration[58].

As q^2 decreases, the structure function rises faster for high x partons than for low x partons (for very low x partons $F(x, q^2)$ actually decreases as q^2 decreases). One can equate high x partons with high mass events and low x partons with low mass events for a fixed $\sqrt{s}$. However, for both classes of events $\alpha_s(q^2)$ increases as q^2 decreases. Thus at high mass the $\alpha_s^2(q^2)$ and the $F(x, q^2)$ terms combine in a positive way while for low mass events the two terms tend to cancel each other and the non-scaling effects are consequently much smaller. This behaviour has been demonstrated by measuring the angular distribution of low mass jet pairs in the UA1 data[59].

This information can now be input into the theoretical determination of the angular distribution to obtain modified predictions. We define q^2 as in equation 4.10 and $\alpha_s(q^2)$ as given by equation 2.11 with $f = 6$ (number of quark flavours) and $\Lambda_{QCD} = 200$ MeV. The structure functions used are those obtained by the CDHS Collaboration, evolved in q^2[60]. We use $G(x, q^2)$ and the relationship $F_2(x, q^2) \equiv Q(x, q^2)$ to evaluate an effective structure function $F(x, q^2)$ (§2.3.7). For each bin in χ the contribution to the cross-section is weighted by

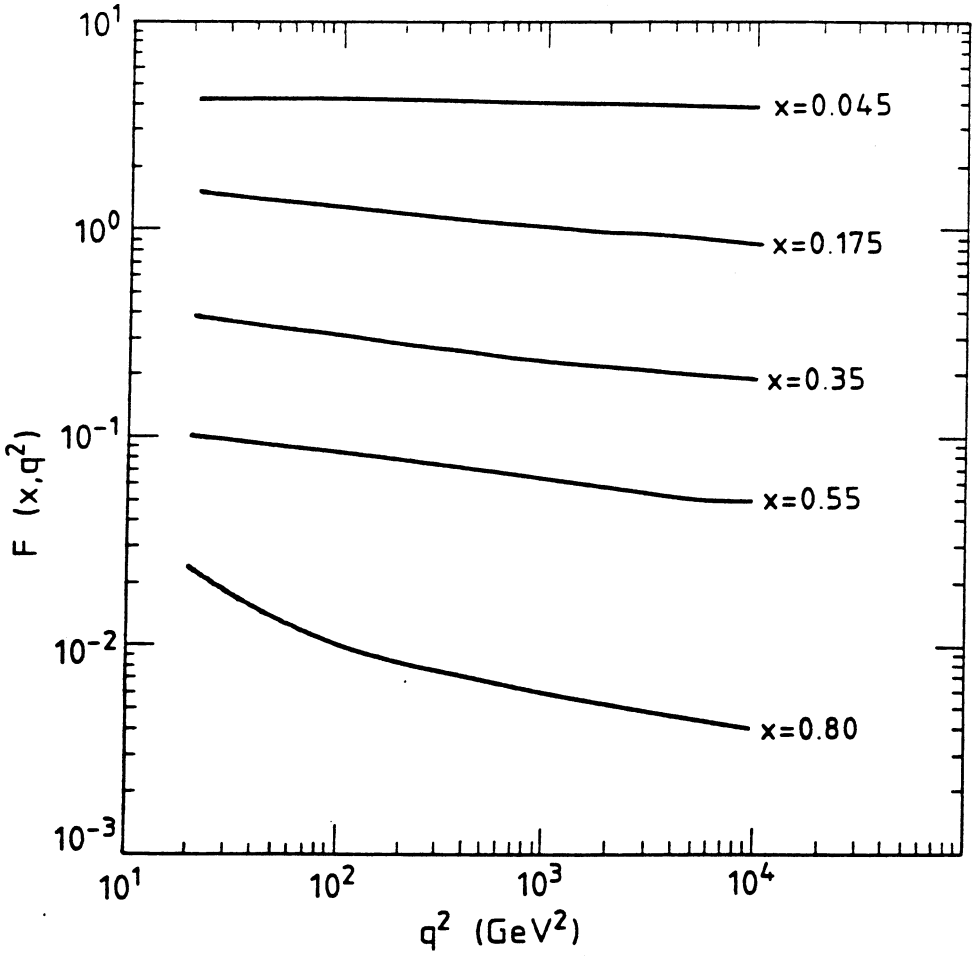

Figure 4.10 Behaviour of the structure function obtained by the Charm Collaboration as a function of q^2 for different values of x.

$\alpha_s^2(q^2)F(x_1,q^2)F(x_2,q^2)$. The results of including these non-scaling terms are shown in Figures 4.11a and 4.11b where they are compared to data sample 1 and data sample 2 respectively. For both experiment and theory the quantity $1/N\ dN/d\chi(\chi)$ is plotted. The dashed curve is the angular distribution obtained if we weight by $\alpha_s^2(q^2)$ alone *or* $F(x_1,q^2)F(x_2,q^2)$ alone, both distributions having almost identical shapes. This curve does not describe the data very well , it still predicts a larger event rate at $\chi = 1$ than is actually observed. However, the solid curve includes both $\alpha_s^2(q^2)$ and $F(x_1,q^2)F(x_2,q^2)$ terms and describes the data much better, especially at $\chi = 1$, an indication that *both* non-scaling effects are required. Note that this applies for a given value of Λ_{QCD}, changing this pa-

rameter would change the shape of the curves and could mean better agreement between the dashed curves and the data.

This improved agreement between theory and experiment also leads us to conclude that the assumption of $q^2 \rightarrow q^2(1-\cos\theta)$ seems to be a reasonable one.

Having demonstrated that the data is indeed compatible with $q^2 = -\hat{t}$ it is now possible to try and extract more detailed information about the q^2- scale of the hard scattering process.

4.4 Acceptance corrections

The results that follow are based on sample 2 only as the statistics of the sample are better and the determination of the detection efficiency will be more straightforward due to the initial selection procedure (Appendix A). The threshold used in the software filter selection was a *sharp* threshold of $E_T > 40$ GeV on the uncorrected transverse energy of the jets. After correcting the jet 4-momenta as described in §4.1 this threshold is no longer sharp, instead there is a depletion of events around $E_T \sim 40$ GeV caused by events which *should* have migrated upwards from $E_T < 40$ GeV. The effect of this on the angular distributions should be small, only contributing at small c.m.s scattering angles and at the lower masses where the jet E_T's are lowest. All events in sample 2 are used and a weight is determined for each *jet* as a function of its corrected E_T. Taking the second highest E_T jet of the event we count the number of jets in a particular bin of corrected jet E_T which have $E_T^{uncor} > 40$ GeV and then determine the probability ϵ to find a jet of a particular corrected E_T, where

$$\epsilon = \frac{N(E_T^{uncor} > 40\text{GeV})}{N^{TOT}}. \tag{4.11}$$

Figure 4.12 shows ϵ as a function of the corrected jet E_T of jet 2. This probability is only 13% for jets with E_T's between 40 and 50 GeV but rises rapidly to 100% for jets with $E_T > 65$ GeV. We now define the following categories of events.

1. An event with $E_T^{uncor}(jet\ 1) > 40$ GeV *and* $E_T^{uncor}(jet\ 2) > 40$ GeV has probability $\epsilon_1\epsilon_2$ of being detected.

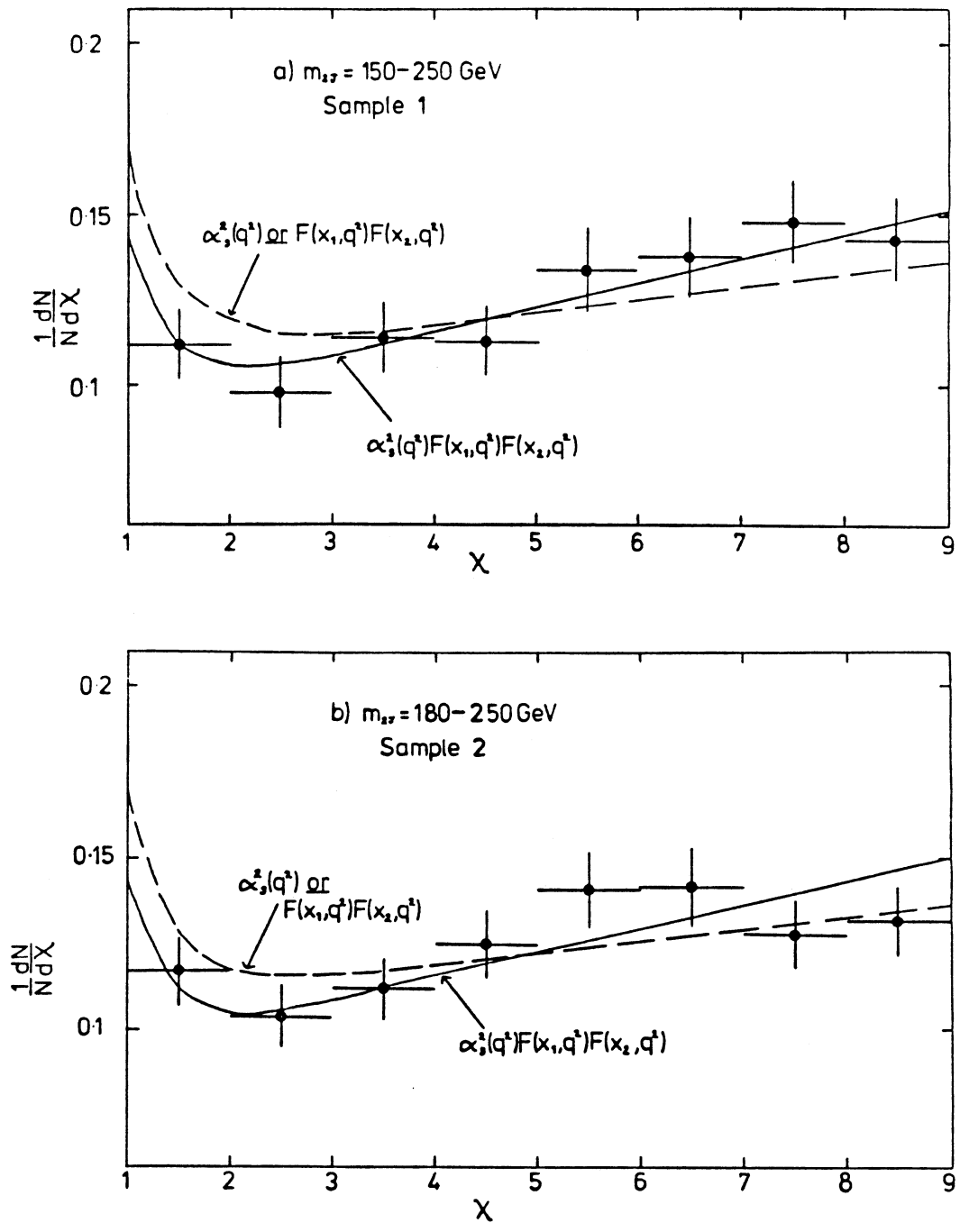

Figure 4.11 Uncorrected two-jet angular distribution in χ for a) sample 1 and b) sample 2. For curves see text.

2. An event with $E_T^{uncor}(jet\ 1/2) > 40$ GeV *but* $E_T^{uncor}(jet\ 2/1) < 40$ GeV has probability $\epsilon_1(1-\epsilon_2) + \epsilon_2(1-\epsilon_1)$ of detection.

3. An event with both $E_T^{uncor}(jet\ 1) < 40$ GeV *and* $E_T^{uncor}(jet\ 2) < 40$ GeV has a detection probability $(1-\epsilon_1)(1-\epsilon_2)$.

We need to correct for events in category 3 which are not observed. For a given event there will be a probability of observing that event which will depend upon the E_T of the two jets in the event. For some events this probability will not be 100% and so we define an event weight W where

$$W = [1-(1-\epsilon_1)(1-\epsilon_2)]^{-1}. \tag{4.12}$$

Those events that have $\epsilon_1 = 1$ or $\epsilon_2 = 1$ will have $W = 1$ while those events with $\epsilon_1 \neq 1$ and $\epsilon_2 \neq 1$ will have $W > 1$. In Table 4.3 we give the resulting angular distribution over the mass range $m_{2J} = 180$-250 GeV.

4.5 Resolution effects

No calorimeter has perfect resolution for measuring energy depositions, it can either detect too much energy or too little energy with equal probability, assuming the detector is properly calibrated. However, because the production cross-section for jets is a steeply falling distribution (for mass or E_T) then effectively we see more events than we should at any point in the distribution due to events which were actually produced at lower mass or E_T. This effect is known as *smearing* and has to be removed from the distributions.

One method is to generate events using a full QCD Monte Carlo and then to pass these events through a full simulation of the UA1 apparatus, and then fully reconstruct the events, as for data. The generated events can then be compared to the reconstructed events to obtain the effect of the resolution smearing. The second method and the one which we choose to adopt is simpler and requires considerably less computing time. We use a simple QCD Monte Carlo to generate events in which the jets are massless, they undergo no bremsstrahlung and no fragmentation. For further details of the Monte Carlo we refer the reader to

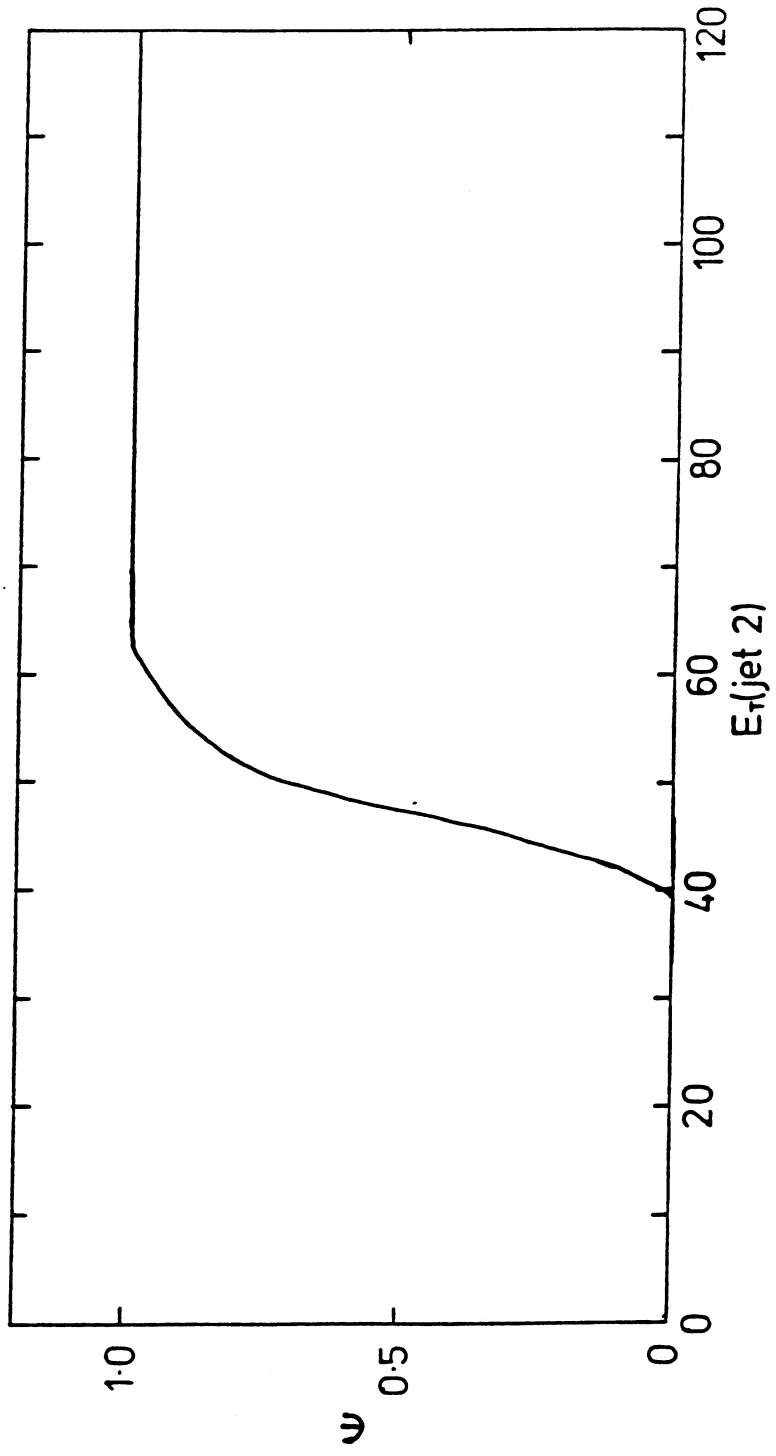

Figure 4.12 Detection efficiency ϵ for a jet of $E_T > 40$ GeV as a function of the corrected jet E_T.

χ	$(N_j)_1 + (N_j)_2$	N_j	$\langle W \rangle$
1-2	169	169	1.0
2-3	150	150	1.0
3-4	162	162	1.0
4-5	181	181	1.0
5-6	204	204	1.0
6-7	206	207.4	1.007
7-8	186	189.8	1.022
8-9	191	196.7	1.03

Table 4.3 Angular distribution after applying acceptance corrections.

Appendix B. Then, using the information about the jet resolution derived from the study described in §4.1 we "smear" the 4-vectors of the jets accordingly using a normally distributed random number, i.e., we assume that the energy resolution is Gaussian. These events are then passed through the same analysis chain as the data and generated distributions are compared to the distributions containing "reconstructed" events to obtain a bin-by-bin correction that can be used to correct the reconstructed distribution so that it resembles the generated one.

For our purposes we are not too concerned with the overall event rate as we are not making a cross-section measurement. What are important are any systematic effects due to differences in energy resolution between the various parts of the calorimeters. In Figure 4.13 we plot the jet energy resolution $\sigma(E_{jet})$ as a function of the pseudorapidity of the jet axis η_{jet} for a jet of E_T =40 GeV for two different azimuthal positions of the jet axis. Clearly the plot exhibits structure, there is a definite worsening of the resolution in the region of η_{jet} =1.5-1.7 where the central and end-cap calorimeters join and again at large η_{jet} the resolution worsens. There is also a trend towards larger $\sigma(E_{jet})$ as the azimuthal position of the axis approaches $\phi = 90^0$, where in the central region the two halves of the calorimeter are joined. This dependence of $\sigma(E_{jet})$ on η_{jet} may affect the shape of the angular distribution. Working in the approximation of

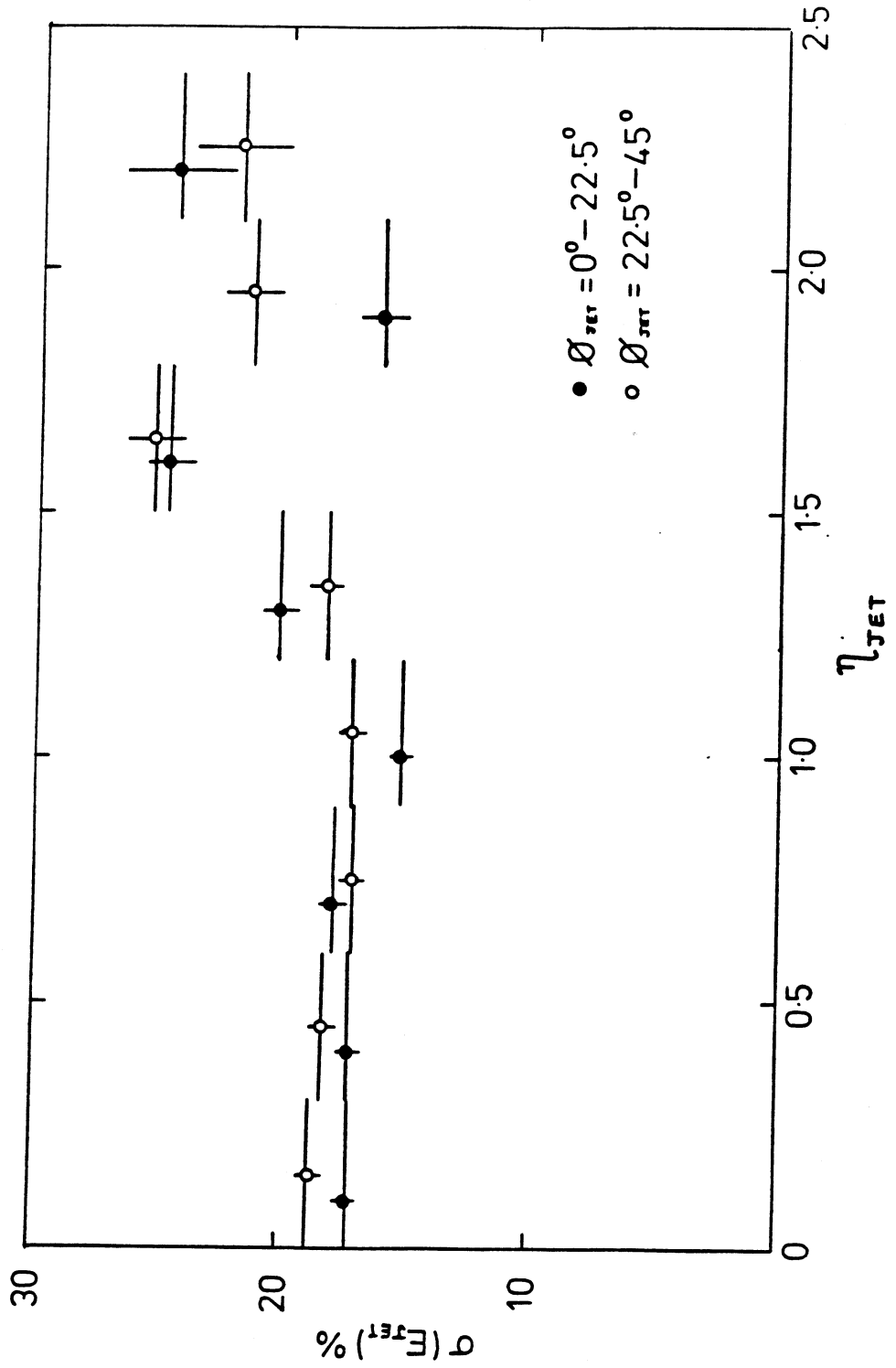

Figure 4.13 Resolution $\sigma(E_{jet})$ for a jet of $E_T = 40$ GeV as a function of jet pseudorapidity.

small longitudinal boosts, then $\theta_{cms} \approx \theta_{lab} \equiv \eta_{jet}$ so that we could expect the events at larger rapidity (small θ_{cms}) to have suffered more smearing than those in the central region, thus leading to a systematic overestimate of the event rate at small scattering angles. In Figure 4.14 we have plotted the correction factor $F(\chi)$ for each bin of χ where

$$F(\chi) = \frac{\text{Number of smeared events}}{\text{Number of generated events}}. \tag{4.13}$$

$F(\chi)$ rises more or less linearly with χ from 1.27 at $\chi = 1-2$ to 1.56 at $\chi = 18-19$, thus showing that there is indeed a systematic effect attributable to the reasons given above. The error on each point is $\sim 1.5\%$. The number of smeared events is always greater than the number of generated events because of the steeply falling jet cross-section.

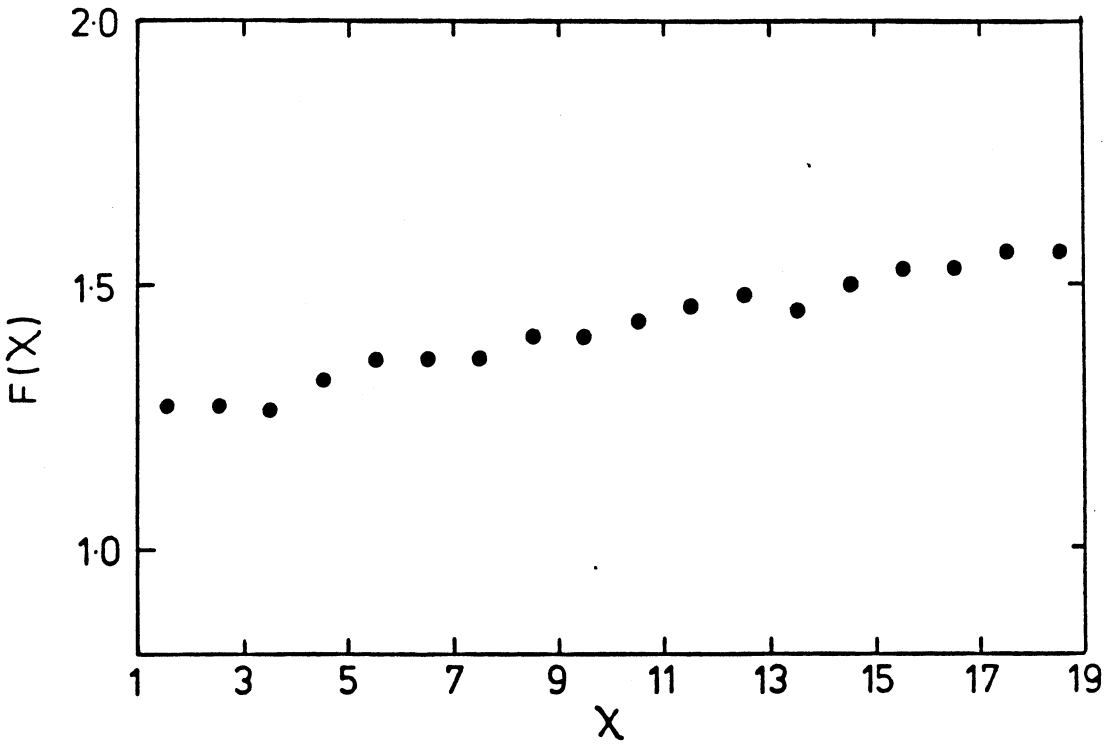

Figure 4.14 Smearing factors $F(\chi)$ as a function of χ.

These correction factors can now be applied to the angular distribution given in Table 4.3 to produce the final two-jet angular distribution for sample 2 as a

χ	N_j/F_j	$1/NdN/d\chi$
1-2	133	0.121 ± 0.01
2-3	118	0.107 ± 0.009
3-4	129	0.117 ± 0.01
4-5	137	0.125 ± 0.01
5-6	150	0.136 ± 0.01
6-7	153	0.139 ± 0.01
7-8	140	0.127 ± 0.01
8-9	140	0.127 ± 0.01

Table 4.4 Final angular distribution for sample 2, $m_{2J} = 180 - 250$ GeV.

function of χ for $m_{2J} = 180$-250 GeV which is given in Table 4.4 where N_j is as defined in Table 4.3 and F_j is the correction applied for each bin j.

As well as the effect of resolution on the angular distribution we are also interested in its effect on the two-jet mass spectrum. As described at the beginning of this section more events are observed at high mass than are actually produced, this is referred to as *hardening* of the spectrum. In correcting for this effect we remove a larger percentage of events at high mass than at low mass, in other words the mass spectrum *softens*.

The smearing factors $F(m_{2J})$ as a function of mass have been obtained by comparing the generated mass spectrum to the reconstructed spectrum and are plotted versus m_{2J} in Figure 4.15. The shape of the distribution is well represented by a fit of the form $F(m_{2J}) = a + bm_{2J} + cm_{2J}^2$ as is indicated by the curve in Figure 4.15.

In Table 4.5 we give the final two-jet mass spectrum corrected for detection efficiency as described in §4.3 and resolution effects for jet-jet masses between 180 and 300 GeV for sample 2.

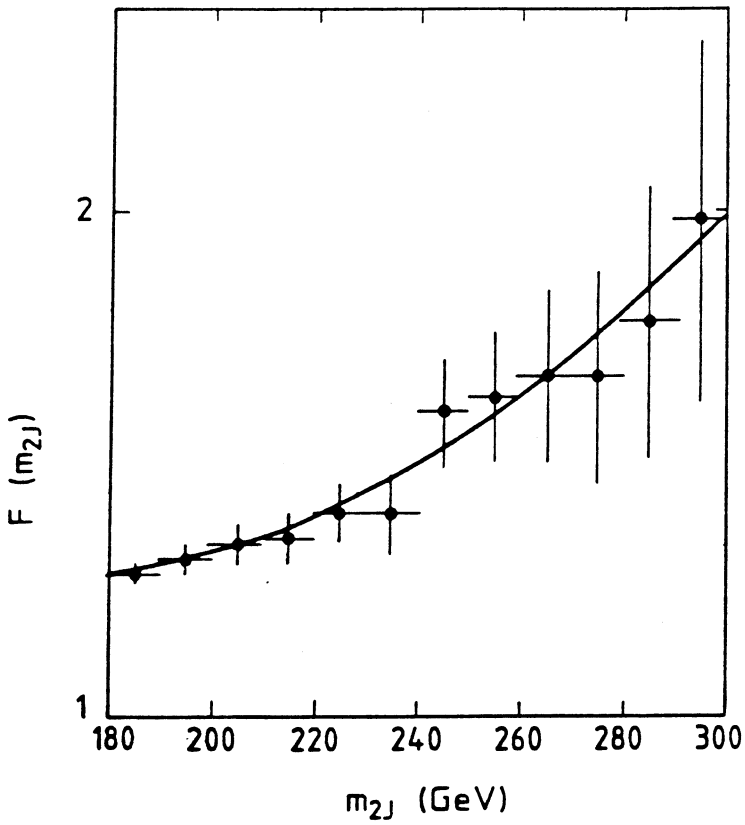

Figure 4.15 Smearing factors $F(m_{2J})$ as a function of the mass of the jet-jet system.

4.6 Parameterization of the two-jet mass spectrum

Having obtained a corrected mass spectrum we can use it to determine a parameterization for the form of the spectrum applicable to the data in the sample. A suitable choice for this parameterization is

$$\frac{dN}{dm_{2J}} = \frac{A}{m_{2J}^n} \tag{4.14}$$

where A and n are parameters to be determined. Taking logarithms of both sides of equation 4.14 yields

$$\ln \frac{dN}{dm_{2J}} = \ln A - n \ln m_{2J} \tag{4.15}$$

and we then use the method of least squares to fit a straight line of this form to

m_{2J}(GeV)	dN/dm_{2J} (Events/10 GeV)
180-190	454.7 ± 18.1
190-200	251.0 ± 13.7
200-210	152.5 ± 10.4
210-220	110.5 ± 8.9
220-230	66.4 ± 7.1
230-240	38.6 ± 5.0
240-250	30.6 ± 4.4
250-260	15.3 ± 3.1
260-270	7.8 ± 2.4
270-280	12.0 ± 2.4
280-290	4.5 ± 1.7
290-300	3.0 ± 1.0

Table 4.5 Final two-jet mass spectrum for sample 2

the data in order to extract $\ln A$ and n. Performing this fit yields

$$\begin{aligned} \ln A &= 58.11 \pm 1.31 \\ n &= 9.96 \pm 0.25 \end{aligned} \tag{4.16}$$

so that the data can be represented by the following parameterization

$$\frac{dN}{dm_{2J}} = \frac{1.73 \times 10^{25}}{m_{2J}^{9.96}}. \tag{4.17}$$

Plotted in Figure 4.16 is the data listed in Table 4.5 along with the fitted spectrum obtained from equation 4.17. We also compare the data to the mass spectrum generated by the Monte Carlo described in the previous section (normalized to the data sample) which can be seen to be in good agreement with the data.

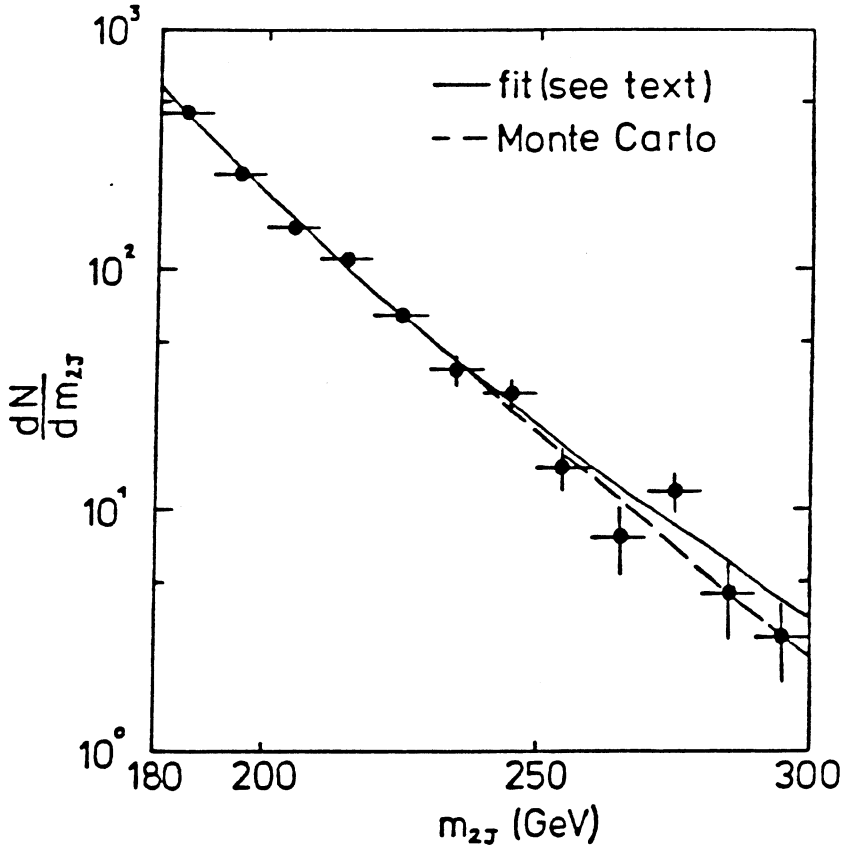

Figure 4.16 Final two-jet mass spectrum for sample 2.

4.7 Determination of the q^2-scale for the two-jet angular distribution

We are now in a position to try to use the angular distribution of the jet pairs to extract the q^2-scale relevant to these events. We define a quantity R where

$$R = \frac{\sigma(\chi = 1-4)}{\sigma(\chi = 4-9)} \tag{4.18}$$

in other words the ratio of the number of events with large scattering angles to the number of events with small scattering angles. This ratio is essentially independent of the jet-jet mass. In other words the shape of the angular distribution, to first order, does not depend on the form of the structure function, which only enters through its logarithmic dependence on q^2. From the measured distribution given in Table 4.4 the ratio is determined to be

$$R_{exp} = 0.528 \pm 0.028. \tag{4.19}$$

This quantity can also be determined from the theoretical distributions and hence the two values can be compared to extract q^2.

There are a number of possible choices for the kinematic form of q^2 which produce the effects observed in the data, for example P_T^2/A,$-\hat{t}/A$, $2\hat{s}\hat{t}\hat{u}/A(\hat{s}^2 + \hat{t}^2 + \hat{u}^2)$ where A is a parameter which we have to determine.

The theoretical calculation we shall use is one written by W.J. Stirling[61]. The program includes all of the $2 \rightarrow 2$ leading order matrix elements and one has the ability to use different structure functions and to change the kinematic definition of the q^2-scale. We shall use the structure functions of Eichten et al.[62] with $\Lambda_{QCD} = 200$ MeV, which is also the value used in the expression for α_s, and f=5 (number of quark flavours). As with the Monte Carlo described in §4.4 we deal only with pure two-jet events with no bremsstrahlung and no fragmentation. We do however include the effects of the q^2-dependence of α_s and of the structure functions that have been shown to be present in the experimental data.

For any particular definition of q^2 we can determine the ratio R_{th} for different choices of the parameter A. In Table 4.6 we list the values of R for the three definitions of q^2 given above and four values of A.

A	R_{th}		
	P_T^2/A	$2\hat{s}\hat{t}\hat{u}/A(\hat{s}^2+\hat{t}^2+\hat{u}^2)$	$-\hat{t}/A$
1	0.557	0.538	0.518
2	0.550	0.533	0.511
3	0.546	0.525	0.507
10	0.529	0.509	0.486

Table 4.6. Values for R_{th} as a function of A and q^2

From Table 4.6 we can see that for each of the kinematic choices of q^2 we will require a different value of the parameter A to match R_{exp} to the theoretical prediction R_{th}. As all three scales produce q^2-values of similar magnitude for fixed A then this will mean that the values for q^2 obtained will differ quite considerably and hence the event rate will also be very different for each of the possibilities. This might at first sight seem totally contradictory but the ratio R is only a measure of the number of events contained in $\chi = 1 - 4$ compared to

the number between $\chi = 4 - 9$ and tells us nothing about the absolute rate of events. As we are not using any overall normalization to tell us this absolute rate then all we are essentially doing is determining the value of A that will produce a distribution of the correct shape but not necessarily the correct event rate. If one fixed the normalization using for example the two-jet mass spectrum then many of the possible choices could probably be eliminated.

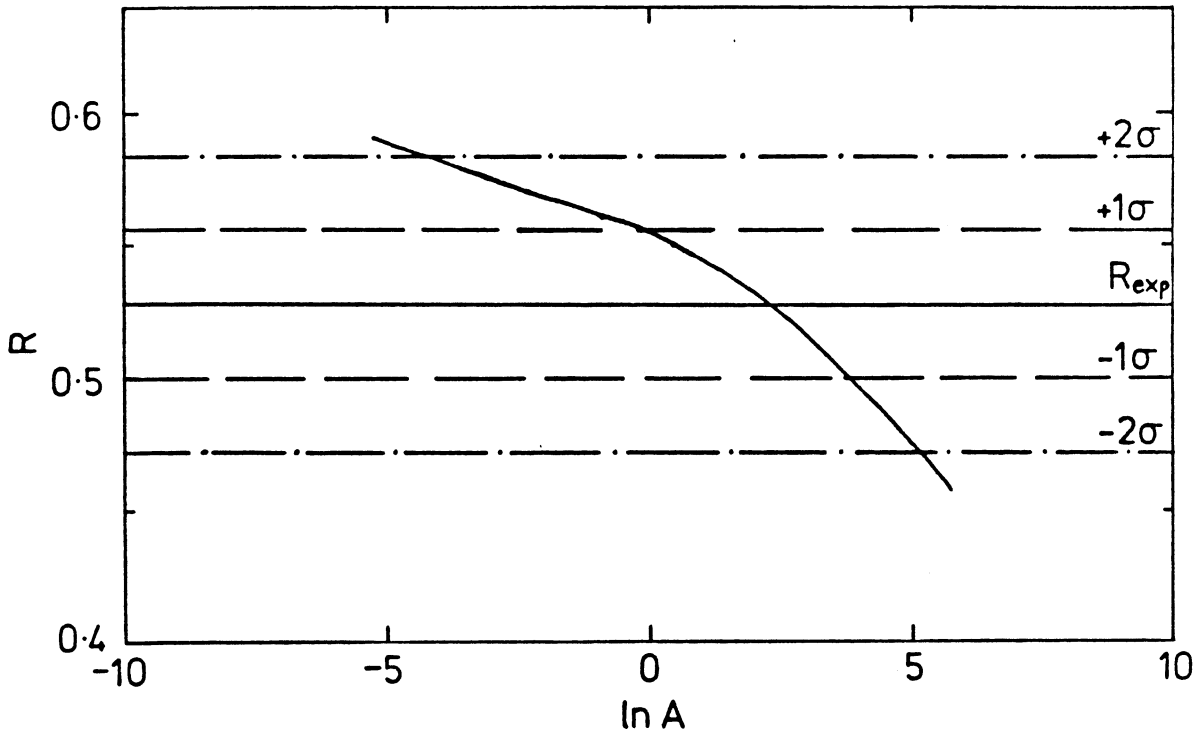

Figure 4.17 The ratio R (see text) as a function of $\ln A$.

As we are only interested in the shape of the distribution we will choose one scale , namely $q^2 = P_T^2/A$ and determine the parameter A. In Figure 4.17 we have plotted R_{th} as a function of $\ln A$ for values of A between 0.01 and 200. It can be clearly seen that R_{th} varies very slowly with A from 0.587 at $A = 0.01$ to 0.469 at $A = 200$, in other words while A changes by four orders of magnitude R_{th} changes by only 20%. Along with the theoretical prediction for R_{th} in Figure 4.17 we have also included the experimentally determined value, R_{exp} given by equation 4.19. Assuming that the error on R_{exp} is Gaussian (a valid assumption because the number of events is sufficiently large) then we can obtain a value for

$\ln A$ by reading off the point at which R_{exp} and the theoretical curve intersect along with the error on the value given by the point at which the curve intersects the $\pm 1\sigma$ line. This value is determined to be

$$\ln A = 2.35^{+1.5}_{-2.3}. \tag{4.20}$$

Hence the value of A is 10.5 and we can write

$$\mathrm{q}^2 = \frac{P_T^2}{10.5}. \tag{4.21}$$

We can also use Figure 4.17 to obtain limits on the range of possible values of $\ln A$, by taking the values at which the $\pm 2\sigma$ line intersects the curve we obtain

$$5.2 > \ln A > -4.2 \qquad \text{at 95\% C.L.} \tag{4.22}$$

We conclude from these results that using the angular distribution we cannot place very tight constraints on the possible values of A because the very slow variation of R_{th} over many orders of magnitude in A means that most choices lie within the errors of our measurement. We can however eliminate the choice of $\hat{\mathrm{s}}$ as a possible scale as will now be demonstrated.

If we define $\mathrm{q}^2 = \hat{\mathrm{s}}/A$ then because we are using events of fixed mass then $\hat{\mathrm{s}}$ remains constant and changing A only alters the overall event rate but does not affect the value of R_{th}, which remains constant for all values of A. We obtain a value for R_{th} of 0.678 and, to the extent that the data show a rise with χ, this value can be excluded at the level of 5σ, clearly demonstrating that $\hat{\mathrm{s}}/A$ is not a viable scale for the two-jet angular distribution. The finite width of the mass bin causes R_{th} to vary from 0.675 to 0.680, a negligible change, so the quoted value is an average.

In Figure 4.18 we compare the experimental angular distribution given in Table 4.4 to the prediction obtained by taking $\mathrm{q}^2 = P_T^2/10.5$ in the calculation described above. This choice for q^2 gives a variation of $\sim 10\%$ in α_s from $\chi = 1$ to $\chi = 9$. Finally in Figure 4.19 the ratio R is plotted as a function of the

jet-jet mass for $m_{2J} = 180 - 300$ GeV and is indeed independent of mass within the experimental errors. The solid curve is the QCD prediction assuming $q^2 = P_T^2/10.5$.

4.8 Determining the number of space-time dimensions

One result of the calculation of the higher order corrections to the two parton scattering processes[38] is that the $2 \rightarrow 2$ matrix elements are given in terms of the number of space-time dimensions n. For all the $2 \rightarrow 2$ processes except $gg \rightarrow gg$ this introduces extra terms into the matrix elements that are functions of ϵ where

$$\epsilon = \frac{4-n}{2} \tag{4.23}$$

so that $\epsilon = 0$ when $n = 4$. In n dimensions phase-space is also modified, introducing a factor of

$$P = \left(\frac{\hat{s}^2}{\hat{u}\hat{t}}\right)^{\epsilon} = \left(\frac{(1+\chi)^2}{\chi}\right)^{\epsilon} \tag{4.24}$$

into *all* the subprocesses. Considering the matrix elememt for $q\bar{q} \rightarrow q\bar{q}$, the quantity Σ in Table 2.1, becomes (ignoring the phase-space factor)

$$\Sigma'_{q\bar{q}\rightarrow q\bar{q}} = \frac{4}{9}\left(\frac{\hat{s}^2+\hat{u}^2}{\hat{t}^2} + \frac{\hat{u}^2+\hat{t}^2}{\hat{s}^2} - 2\epsilon\right) - \frac{8}{27}(1-\epsilon)\left(\frac{\hat{u}^2}{\hat{s}\hat{t}} + \epsilon\right) \tag{4.25}$$

and for the process $qg \rightarrow qg$

$$\Sigma'_{qg\rightarrow qg} = -\frac{4}{9}\left(\frac{\hat{u}^2+\hat{s}^2}{\hat{u}\hat{s}} - \frac{\epsilon\hat{t}^2}{\hat{u}\hat{s}}\right) + \left(\frac{\hat{u}^2+\hat{s}^2}{\hat{t}^2} - \epsilon\right). \tag{4.26}$$

To investigate what effect, if any, the existence of extra flat space-time dimensions may have on the two-jet cross-section we have plotted in Figure 4.20 the quantity $\Sigma' \times P$ for the subprocesses $gg \rightarrow gg$, $qg \rightarrow qg$ and $q\bar{q} \rightarrow q\bar{q}$ for $\chi = 1$ and $\chi = 9$. For both scattering angles the cross-sections decrease as n increases with the cross-sections for $\chi = 9$ decreasing faster than those at $\chi = 1$. This implies that the appearance of extra flat dimensions will be characterized by a change in shape of the angular distribution with fewer events at $\chi = 9$ relative to $\chi = 1$.

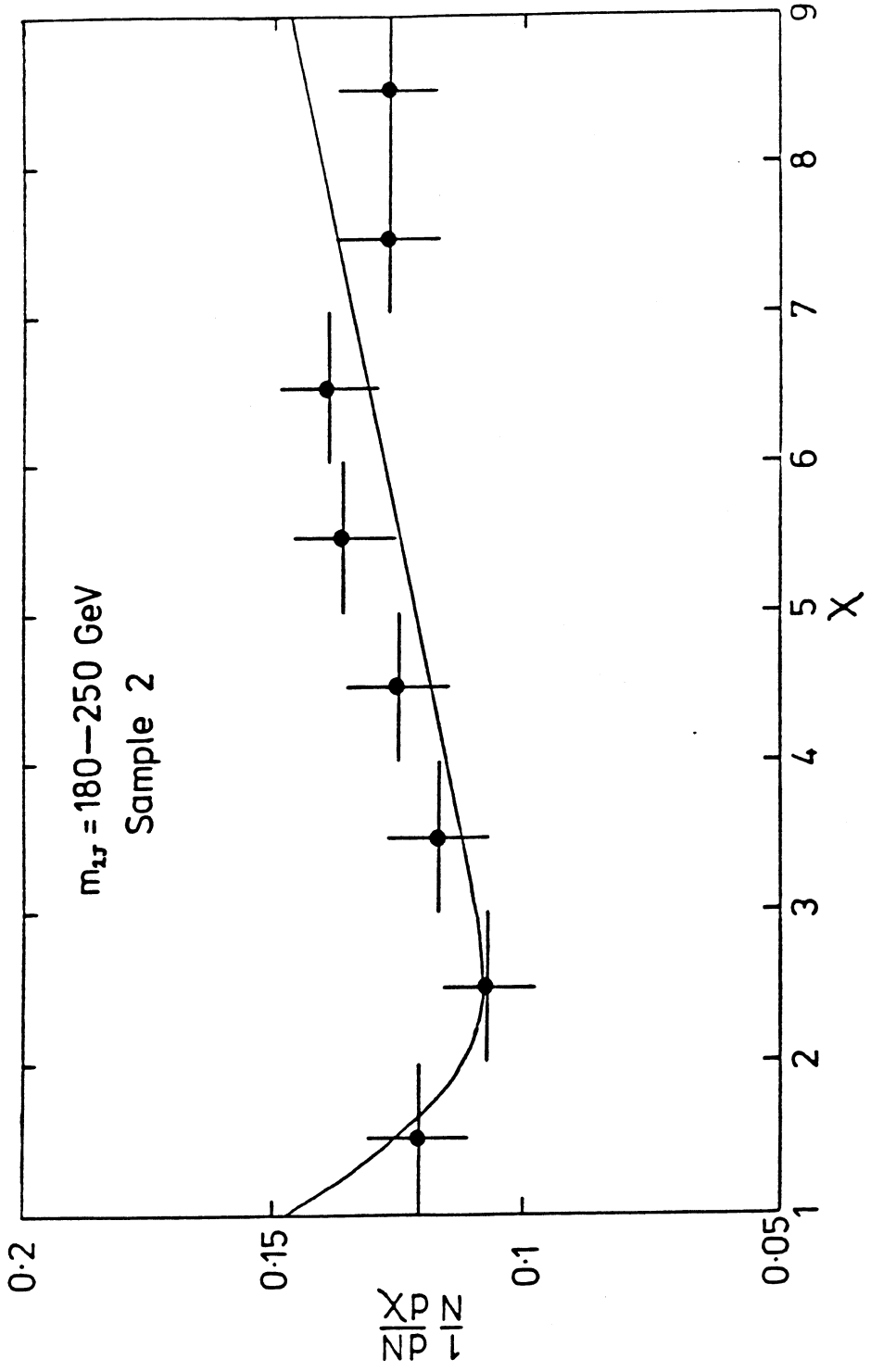

Figure 4.18 Final angular distribution for sample 2, $m_{2J} = 180 - 250$ GeV.

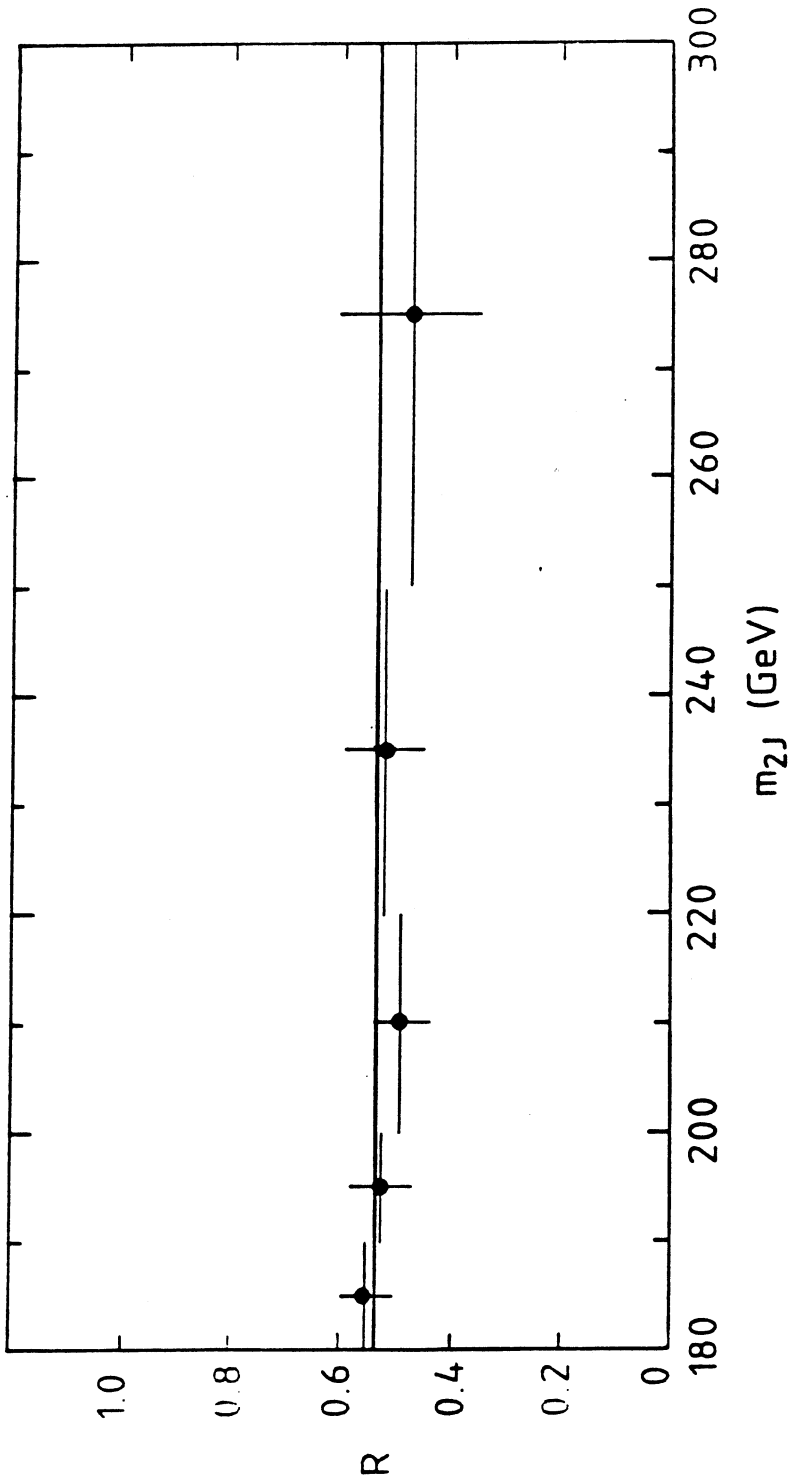

Figure 4.19 Ratio R (see text) as a function of the jet-jet mass.

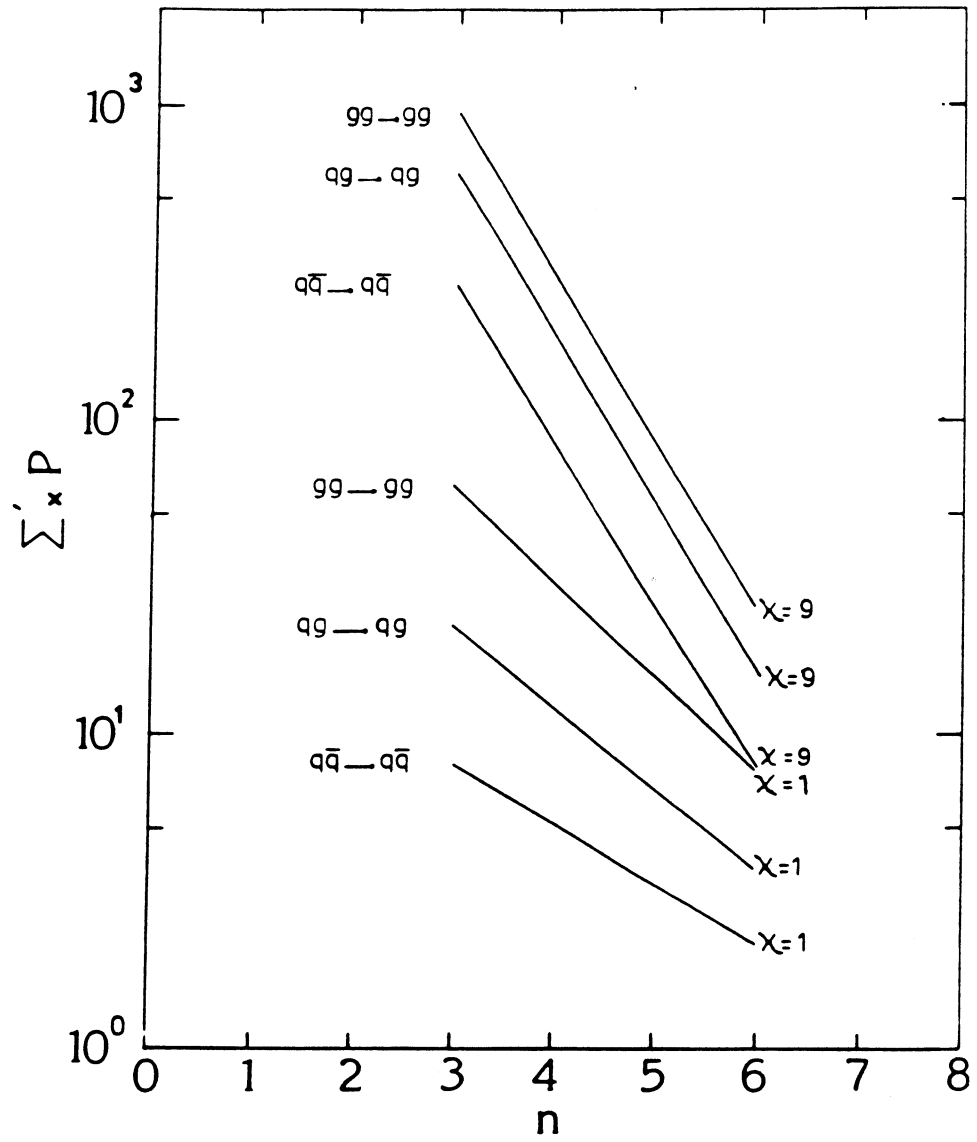

Figure 4.20 $2 \rightarrow 2$ scattering processes in n-dimensions for $\chi = 1$ and $\chi = 9$.

It follows that the two-jet angular distribution can be used to measure the number of flat space-time dimensions. Such extra dimensions would normally be curled up and hence not visible at lower energies but once the energies of the interacting partons are such that their Compton wavelength is of order the radius of the extra dimension then they may be scattered into this dimension. As we do not know at what energy scale this would happen we will use the highest mass two-jet events, those with $m_{2J} = 250 - 300$ GeV. As we are at such high mass the angular range can be extended to $\chi = 19$ without encountering any problems of acceptance.

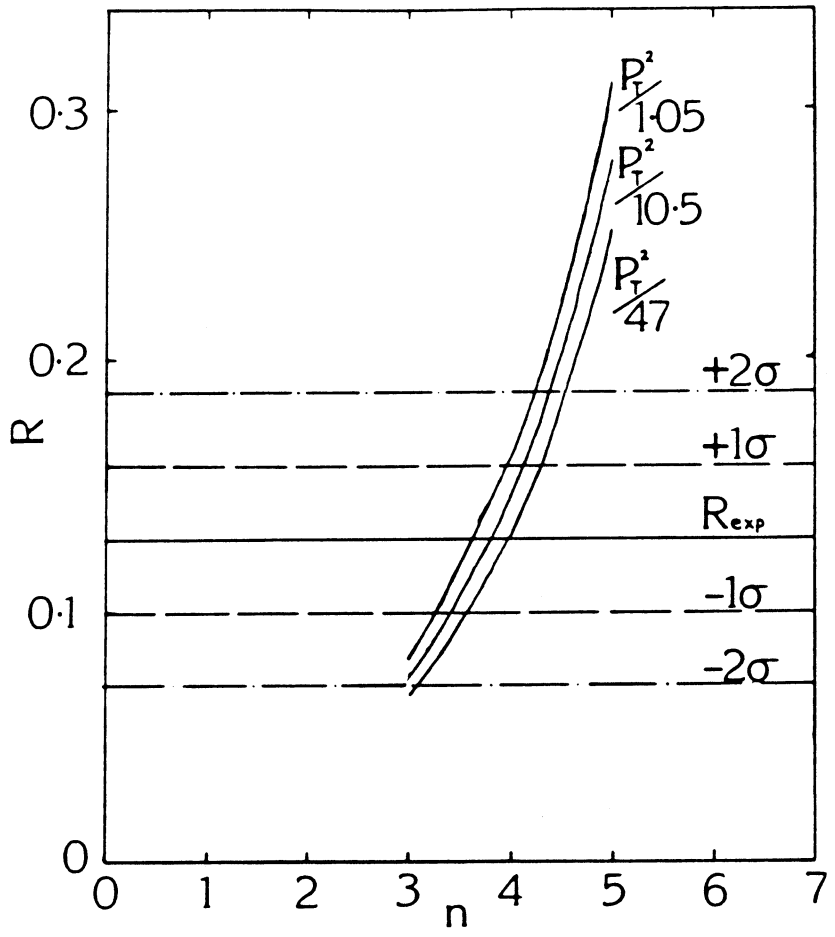

Figure 4.21 Ratio R (see text) as a function of the number of space-time dimensions.

Again we define a ratio R where in this case

$$R = \frac{\sigma(\chi = 1-4)}{\sigma(\chi = 4-19)}. \tag{4.27}$$

The experimental distribution has been corrected for the effects of acceptance and resolution as described previously. From the data we determine $R_{exp} = 0.129 \pm 0.029$. Using the program described in §4.6, with $q^2 = P_T^2/10.5$ as already determined, we replace the usual matrix elements by those for n-dimensions and compute R_{th} for different values of n. Note that we do not go below $n = 3$ as below this value some of the cross- sections become negative and in particular $\sigma(gg \rightarrow q\bar{q}) = \infty$ for $n = 2$. To estimate the uncertainty caused by different choices of

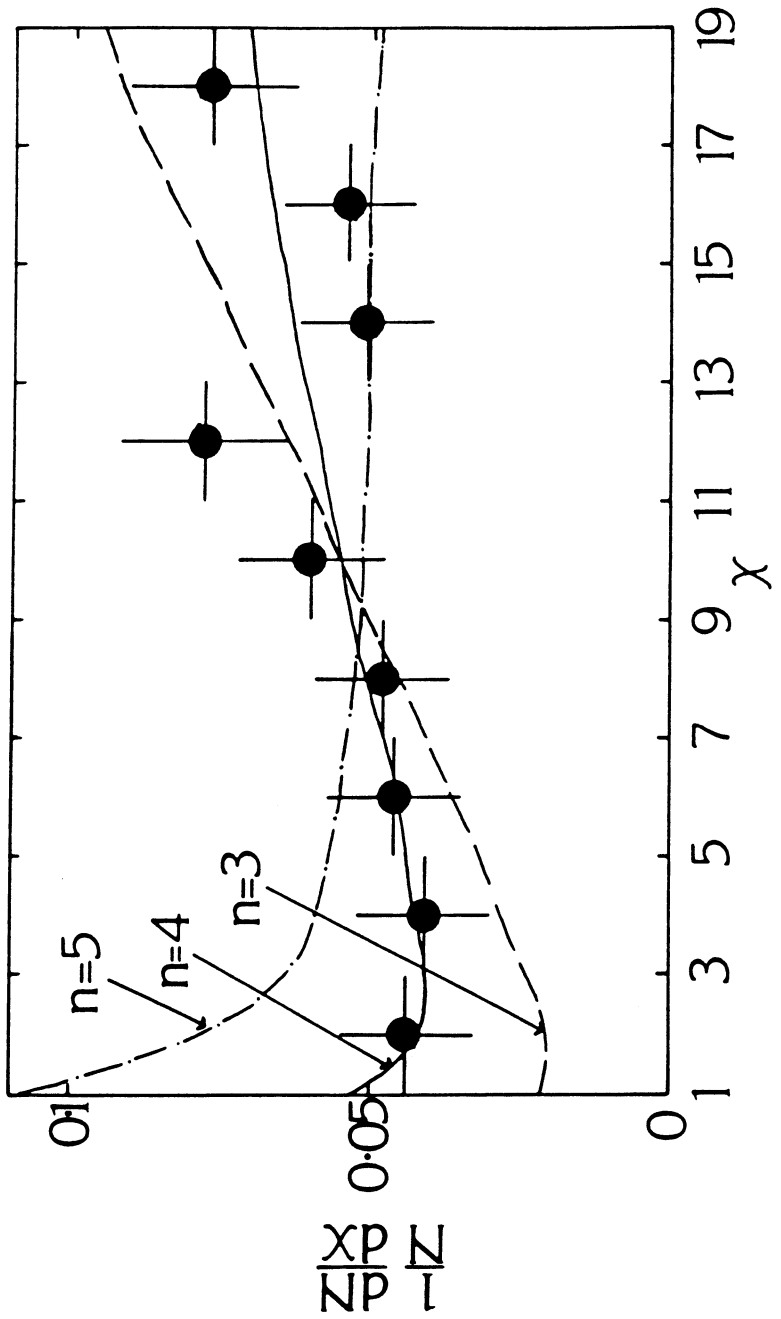

Figure 4.22 Final two-jet angular distribution for sample 2, $m_{2J} = 250 - 300$ GeV. For curves see text.

q^2, R_{th} is also determined using $q^2 = P_T^2/47$ and $q^2 = P_T^2/1.05$, corresponding to the upper and lower values in equation 4.20.

These values for R_{th} are plotted in Figure 4.21 along with the measured value, R_{exp}. Employing the same technique as in §4.6 yields

$$n = 3.8^{+0.3\ +0.2}_{-0.4\ -0.15} \tag{4.28}$$

where the second error is due to the error on the measured q^2- scale. We also obtain the following limit on n of

$$n < 4.4 \qquad \text{at 95\% C.L.} \tag{4.29}$$

with an error of $\pm 5\%$ due again to the uncertainty in the q^2- scale. This assumes that the cross-sections are meaningful for fractional dimensions. If this is not the case then the limit worsens. The experimental distribution is shown in Figure 4.22 along with the theoretical predictions for $n = 3$, 4 and 5.

4.9 Summary

In this chapter we have studied in detail the properties of the two-jet angular distribution. We have seen that in order to obtain agreement between the theoretical and experimental distributions requires the inclusion of non-scaling effects, with equal contributions due to the q^2-dependence of α_s and of the structure function over the mass range under consideration. In only using events of a fixed mass it was shown that the form of q^2 had to include dependence on $\cos\theta$, the c.m.s scattering angle. In trying to determine the form of this dependence we concluded that it was not possible to constrain it very tightly and numerous alternatives were possible. Finally an attempt was made to use the $2 \rightarrow 2$ matrix elements in n-dimensions to place limits on the possible existence of extra flat space-time dimensions.

5. THREE-JET PRODUCTION

Having studied in some detail the properties of two-jet events we will now turn our attention to those events which have a clear third jet of appreciable E_T. Most events do in fact have at least three jets as defined by the UA1 jet algorithm but we require only those events where this third jet is 'real'. In other words it is not just part of a jet from the hard scatter that has fragmented very broadly or part of the spectator jets which may have been produced at large angle to the beam direction. As these effects are non-perturbative and difficult to treat we select those events where all three jets are widely separated from each other and from the spectator jets. This choice of events means that the sample will only contain a small subset of the total three-jet events because the rate of events is greatest when the third jet has a small opening angle with respect to one of the other jets or to the spectator jets.

5.1 The form of the three-jet differential cross-section

The general three-body differential cross-section is written as

$$d\sigma = \frac{(2\pi)^4 |\mathcal{M}|^2}{4\sqrt{(p_1 \cdot p_2)^2 - m_1^2 m_2^2}} d\Phi_3(p_1 + p_2; p_3, p_4, p_5) \tag{5.1}$$

where $|\mathcal{M}|^2$ is an appropriate matrix element and $d\Phi_3$ is the Lorentz invariant three-body phase-space

$$d\Phi_3(p_1 + p_2; p_3, p_4, p_5) = \delta^4 \left(P - \sum_{i=1}^{3} p_i \right) \prod_{i=1}^{3} \frac{d^3 p_i}{(2\pi)^3 2E_i}. \tag{5.2}$$

We now define the following phase-space variables in the centre-of-mass of the three-jet system (Figure 5.1)

1. The Dalitz plot variables x_i where $x_i = 2p_i/\sqrt{\hat{s}}$ with $i = 3, 4, 5$, p_i being the energy of parton i (assuming massless partons), and normalized such that $\sum_{i=3}^{5} x_i = 2$ and ordered such that $x_3 > x_4 > x_5$.

2. $\cos\theta_3$, which is the angle between parton-3 and the incoming partons and ϕ which is the azimuthal angle of parton-3.

3. ψ, which is the angle between the plane containing parton-3 and the incoming partons and the plane containing parton-4 and parton-5.

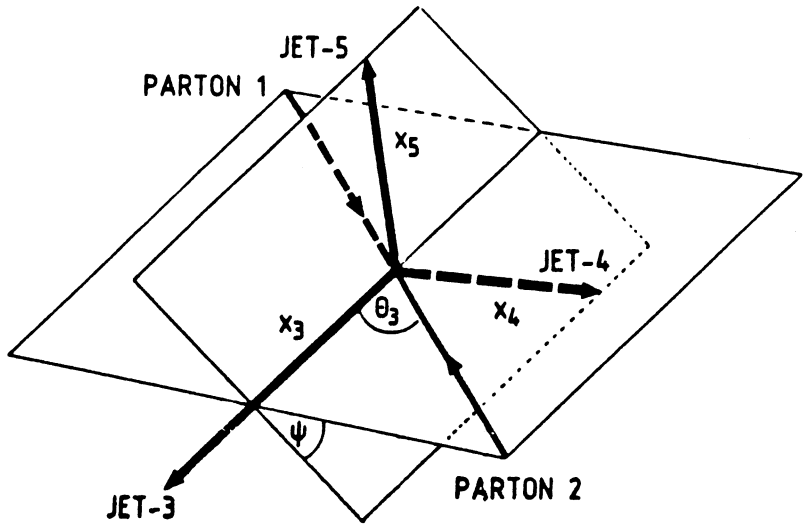

Figure 5.1 Three-jet variables defined in the subprocess c.m.s.

The three-body phase-space can be re-expressed in terms of these variables to give

$$d\Phi_3(x_3, x_4, \cos\theta_3, \psi, \phi) = \frac{\hat{s}}{2^5(2\pi)^9}\, dx_3 dx_4 d\cos\theta_3 d\psi d\phi \qquad (5.3)$$

Substituting this into equation 5.1 and integrating over ϕ gives

$$\frac{d^4\sigma}{dx_3 dx_4 d\cos\theta_3 d\psi} = \left(\frac{1}{32\pi^2}\right)^2 |\mathcal{M}|^2 \qquad (5.4)$$

where $|\mathcal{M}|^2$ is the appropriate leading order matrix element as given by Berends et al.[34].

To obtain curves for comparison with data we first replace the parton momenta by the corresponding x_i's,

$$\begin{aligned} p_1 &\rightarrow 1 \\ p_2 &\rightarrow 1 \\ p_3 &\rightarrow x_3 \\ p_4 &\rightarrow x_4 \\ p_5 &\rightarrow x_5 \end{aligned} \tag{5.5}$$

which allows us to define a dimensionless matrix element squared $|\mathcal{M}'|^2$ where

$$|\mathcal{M}'|^2 = \frac{\hat{s}}{4}\frac{|\mathcal{M}|^2}{g^6} \qquad (g^2 = 4\pi\alpha_s) \tag{5.6}$$

and thus equation 5.4 becomes

$$\frac{d^4\sigma}{dx_3 dx_4 d\cos\theta_3 d\psi} = \left(\frac{1}{4\pi}\right)\frac{\alpha_s^3}{\hat{s}}|\mathcal{M}'|^2. \tag{5.7}$$

We can then generate events according to the three-body phase-space using a simple Monte Carlo, retain the events which satisfy the experimental cuts and weight these events by the corresponding values of $|\mathcal{M}'|^2$. We use the three dominant subprocesses $gg \rightarrow ggg$, $qg \rightarrow qgg$ and $q\bar{q} \rightarrow q\bar{q}g$ and average over the incoming parton types using the relative contributions given in §4.2.

5.2 Three-jet event sample

We now have to decide what criteria to use for defining the event sample so that it satisfies the requirements outlined above. As for the two-jet selection we again apply cuts to dimensionless variables. This way of defining the sample has the advantage that we can combine the previously published[63] data from 1983 with the data from 1984 and plot them together.

First we select all events with at least three reconstructed jets and in each event take the three highest E_T jets only. This is analagous to the two-jet selection where only the top-two were taken and any third jets ignored. Here, again,

any fourth jets are ignored. In the case of hard fourth jets due to bremsstrahlung the problem of whether to add the jet to one of the other jets again arises. As the parentage of this jet is even more uncertain than in the two-jet case we choose not to adopt this procedure. For sample 1 5% of the events have a fourth jet with $E_T > 20$ GeV and for sample 2 the figure is 20%. This is a higher percentage than in the two-jet sample where the contamination was $\sim$ a few percent. An alternative source of four-jet events is double-parton scatters but for high enough jet transverse energies the bremsstrahlung mechanism is expected to dominate[64].

We then perform a Lorentz boost to the c.m.s of the three-jets as described in §4.2. There now are a number of possible variables which could be used to define the sample and two choices are described here. After studying both possibilities the second one is chosen for reasons which will be described below.

(i) The jets are placed in order of decreasing *momenta* and the angle θ_i that each jet makes with the average beam direction is determined, where

$$\cos\theta_i = \frac{\mathbf{p}_i^{cms} \cdot \mathbf{p}_{av}^{cms}}{|\mathbf{p}_i^{cms}| \cdot |\mathbf{p}_{av}^{cms}|}, \quad i = 3,4,5 \tag{5.8}$$

The Dalitz plot variables are defined in terms of momenta as $x_i = 2p_i/\sum_i p_i$. Then for each of the jets we define x_{T_i}, the scaled transverse momentum of jet-i, with

$$x_{T_i} = x_i \sin\theta_i. \tag{5.9}$$

To prevent any of the jets becoming too small or getting too close to the spectator jets we require that the minimum x_T be larger than some chosen value. This minimum x_T is typically x_{T_5}, Figure 5.2a shows the $x_{T_{min}}$ distribution for sample 1. Another cut is required to keep all the jets well separated from each other and for this we use the ΔR variable, where

$$\Delta R_{ij} = \sqrt{(\eta_i - \eta_j)^2 + (\phi_i - \phi_j)^2}, \quad i = 3,4,5. \tag{5.9}$$

The minimum ΔR must be greater than some chosen value, where this minimum value is typically ΔR_{45}, the separation between jet-4 and jet-5. Figure 5.2b

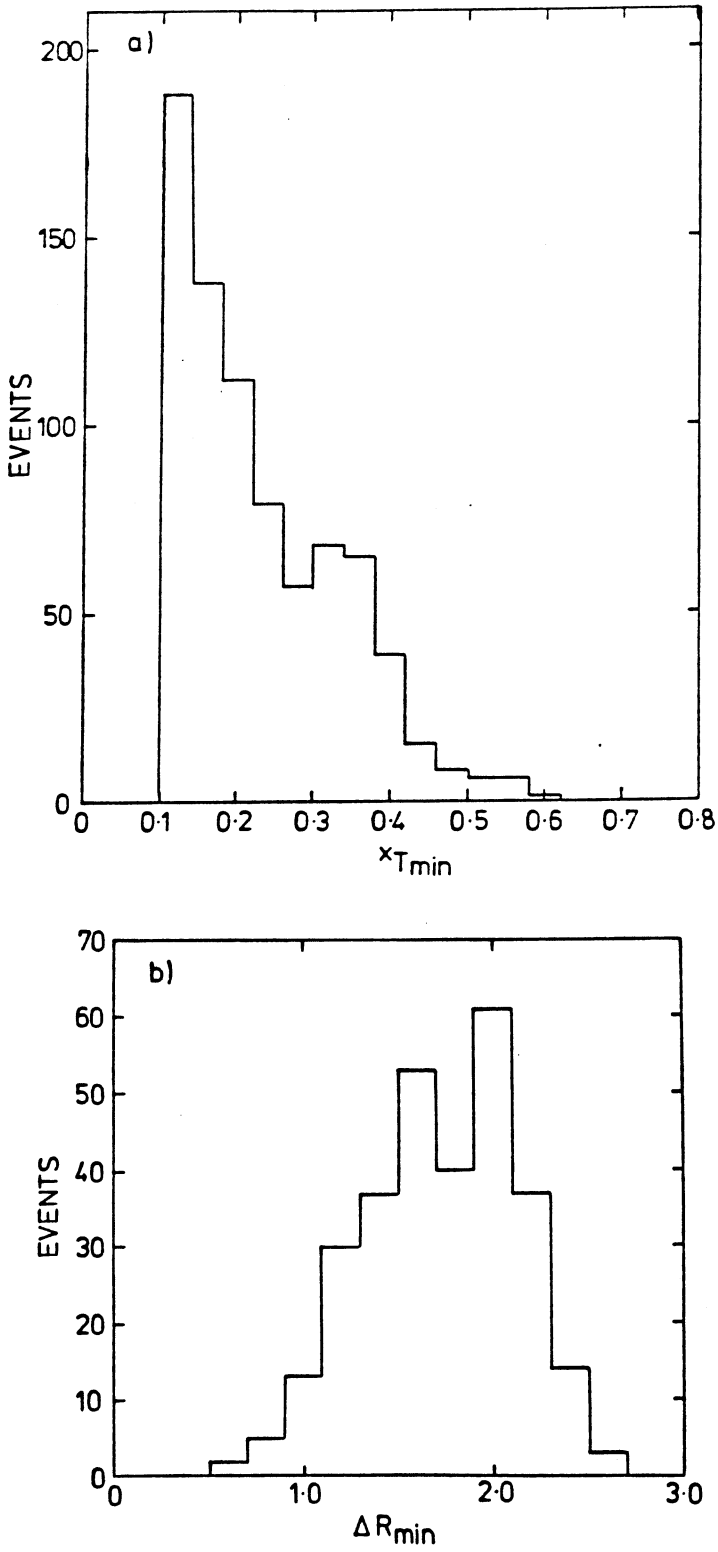

Figure 5.2 The raw distributions for one choice of three-jet variables for sample 1 a) $x_{T_{min}}$, b) ΔR_{min}.

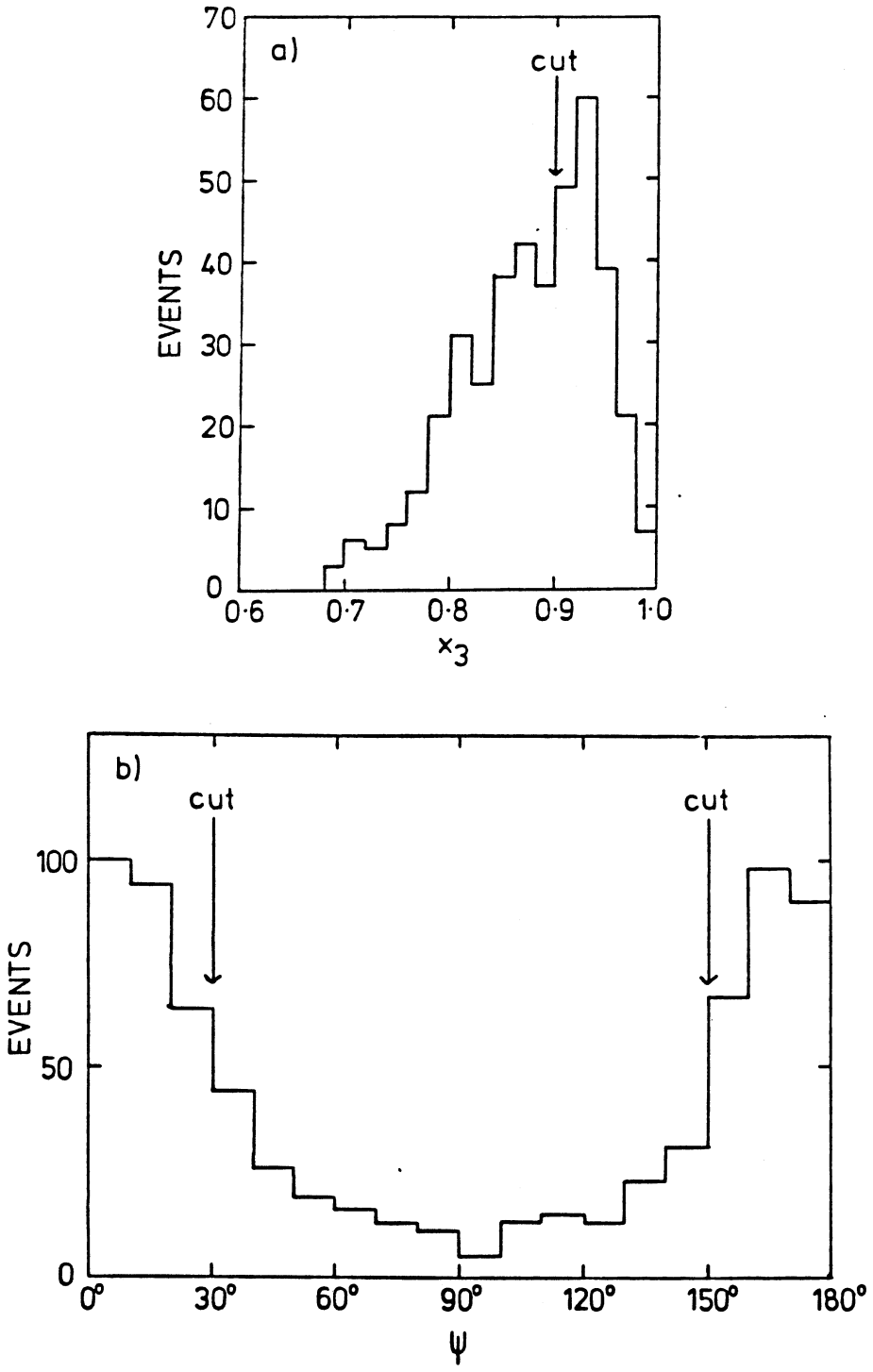

Figure 5.3 The raw distributions for a second choice of three-jet variables for sample 2 a) x_3, b) $|\psi|$.

shows the ΔR_{min} distribution down to 0.5 for sample 1. Of course at the parton level the event rate will increase indefinitely as $\Delta R \rightarrow 0$ but the finite size of the jet algorithm cone means that the possibility of getting two jets very close together is negligible so the event rate in the data decreases.

This choice of variables has two disadvantages. The main one is that any mis-assignment of energy between jets 4 and 5 means that the momenta of these jets and hence the x_i's will be wrongly determined. The second is that the three-parton cross-section is not written in terms of $x_{T_{min}}$ and ΔR_{min} and so applying cuts to these variables makes some of the comparisons between experimental quantities and theoretical predictions harder to interpret.

(ii) For the second choice the jets are arranged in order of decreasing *energy* and the Dalitz plot variables are written as

$$x_i = \frac{2E_i}{\sum_i E_i}, \quad i = 3,4,5 \tag{5.10}$$

where E_i is the energy of jet-i (n.b. $\cos\theta_i$ is still computed using the jet momenta). It should be noted that as the jets have mass, $E_i \neq p_i$, then defining the x_i's in terms of energy leads to slightly larger values for x_3 and hence fewer events will survive the x_3 cut. With the x_3 cut used there is a reduction in the three-jet event sample of $\sim 2\%$ which is negligible. This choice overcomes the first disadvantage as although there may be mis-assignment of the energy between jets 4 and 5, the total energy being a scalar quantity will still be correctly determined.

In order to keep jets 4 and 5 well separated x_3 must not be allowed to become too large and to keep jet-5 away from the plane containing the spectator jets, events with $|\psi| \sim 0^0$ or $|\psi| \sim 180^0$ must be removed. As these are both variables that are used in the theoretical definition of the cross-section then the distributions in these variables will not be modified in a complicated way.

Figure 5.3a shows the sample 2 distribution for x_3 and Figure 5.3b the ψ distribution. At the parton level there are singularities as $x_3 \rightarrow 1$ or as $|\psi| \rightarrow 0^0$ or $|\psi| \rightarrow 180^0$. However the data sample is of course finite and so the cuts must be chosen so that we are well away from any inefficiencies caused by this.

The event sample is chosen so that it satisfies

$$x_3 < 0.9 \text{ and } 150^0 > |\psi| > 30^0. \tag{5.11}$$

Also the mass of the events must satisfy $m_{3J} > 150$ GeV for sample 1 and $m_{3J} > 180$ GeV for sample 2, along with $\cos\theta_3 < 0.6$ to ensure reasonable detection efficiency. One of the events from sample 1 satisfying the above requirements is shown in Figure 5.4.

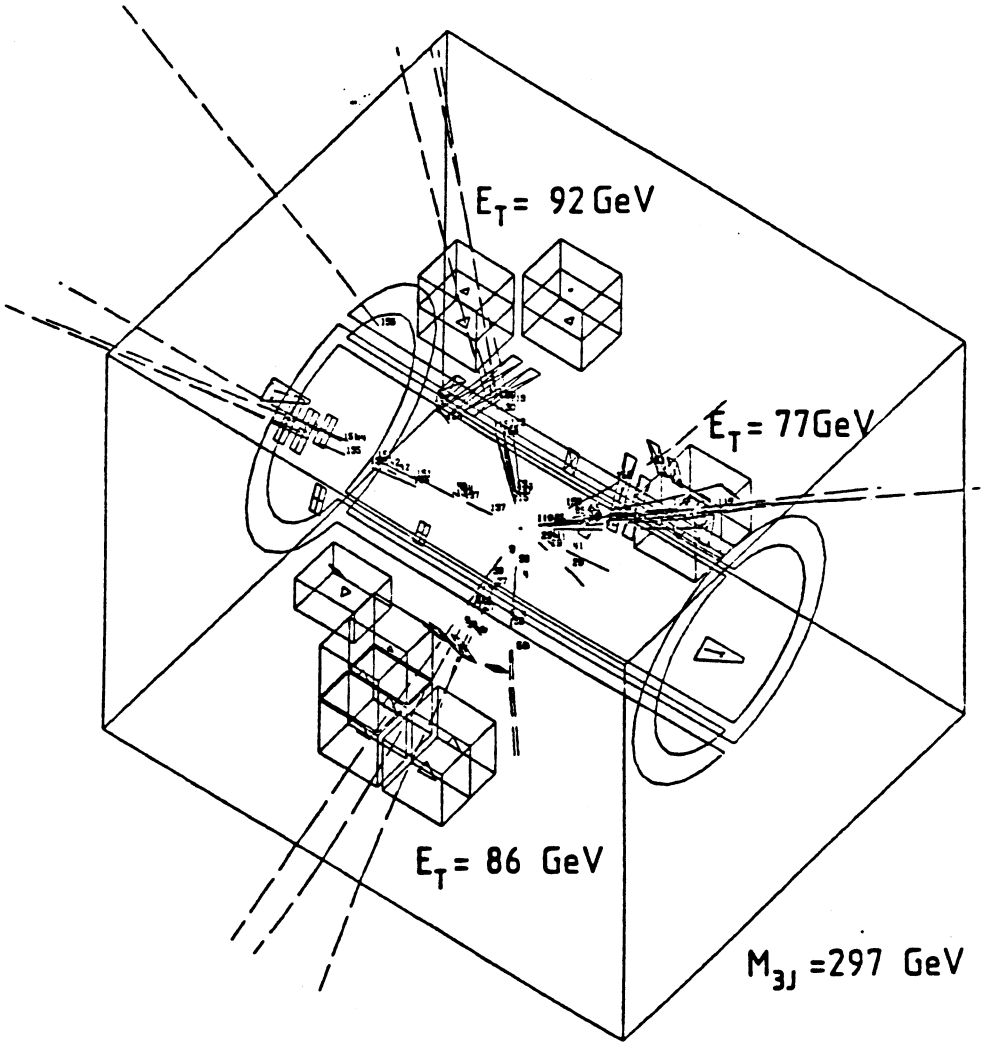

Figure 5.4 A typical three-jet event.

5.3 Acceptance corrections

In order to preserve as large an event sample as possible we have chosen not to remove events where the axis of one of the jets falls close to the vertical gap in the central calorimeters. Instead a correction will be applied to allow for the events which have been lost due to this problem.

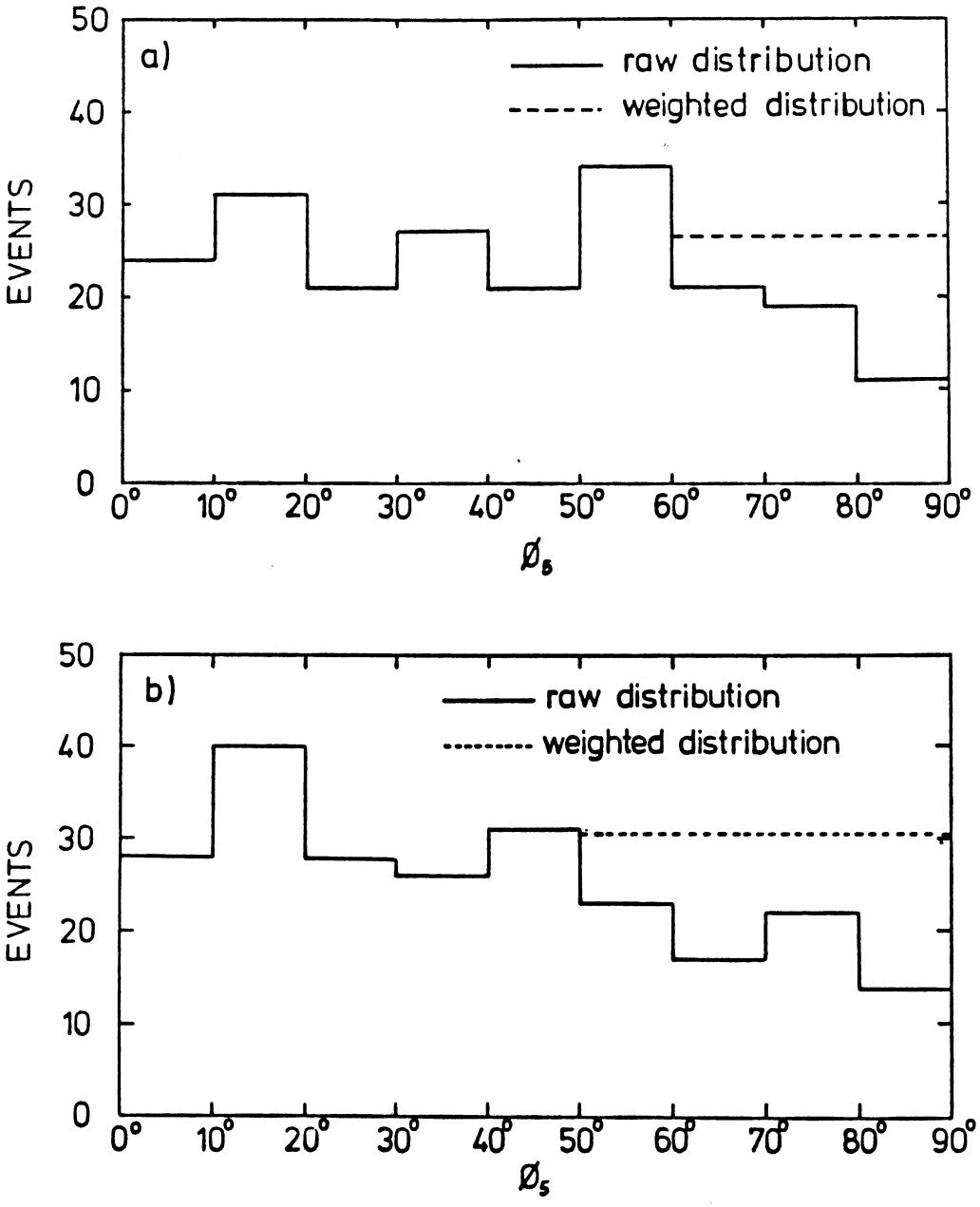

Figure 5.5 The distribution of events in ϕ_5, a) sample 1, b) sample 2.

In order to determine the correction we first consider the ϕ_{cms} distribution of the lowest energy jet (jet-5). The azimuthal angle determined in the c.m.s is used because the 'hole' in the vertical direction is filled in to some extent due to events which have a non-zero transverse boost which smears the ϕ distribution slightly. Figures 5.5a and 5.5b show the ϕ_5 distribution for sample 1 and sample 2 respectively, with both plots having a depletion of events around $\phi_5 = 90^0$.

Assuming that the azimuthal distribution should be flat, a weighting factor can be derived for each of the bins where there is a depletion of events to bring the event rate in each of these bins up to the average value for the rest of the distribution. The dotted lines are the result of performing this procedure for each of the samples. If we then look at the distribution for ϕ_4, shown in Figures 5.6a and 5.6b, then for sample 1 there is still a slight depletion of events for $\phi_4 > 80^0$ which will require further weighting but sample 2 is fairly flat and requires no further weighting.

Also as for the two-jet sample the events must be corrected for any losses due to the fixed threshold of the filter. We use the weighting factors determined in §4.3 and only consider the top-two jets in transverse energy, so each event has a weight as given by equation 4.12. After applying both of these corrections the final event sample contain 212.7 and 279.5 weighted events for sample 1 and sample 2 respectively. The mean weight for both sample 1 and sample 2 is 22%.

5.4 The three-jet mass spectrum

Having applied the acceptance corrections to the samples we can study the properties of the three-jet events. The first distribution to be considered is the mass spectrum for the events. In Figure 5.7 is plotted the corrected mass spectrum for both sample 1 (crosses) and sample 2 (full circles), with sample 1 normalized to sample 2 in the range $m_{3J} = 180 - 250$ GeV. The two samples are clearly consistent with each other although again sample 1 is a little lower than sample 2.

Analagous to the two-jet case we write the parameterization of the spectrum

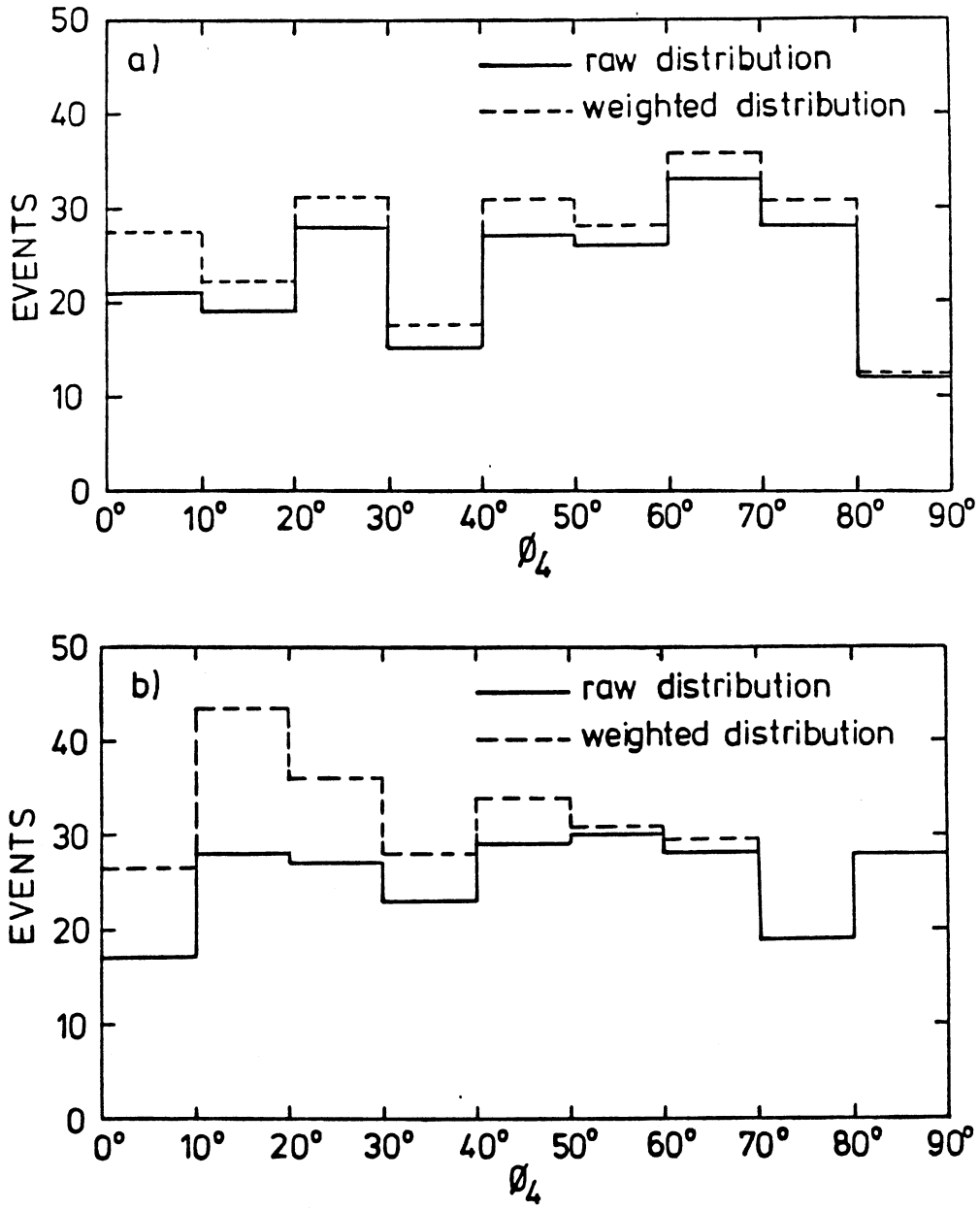

Figure 5.6 The distribution of events in ϕ_4, a) sample 1, b) sample 2.

as

$$\frac{dN}{dm_{3J}} = \frac{A}{m_{3J}^n} \tag{5.12}$$

where A and n have to be obtained by fitting the spectrum. However first the effects of resolution have to be removed from the spectrum. We use the same

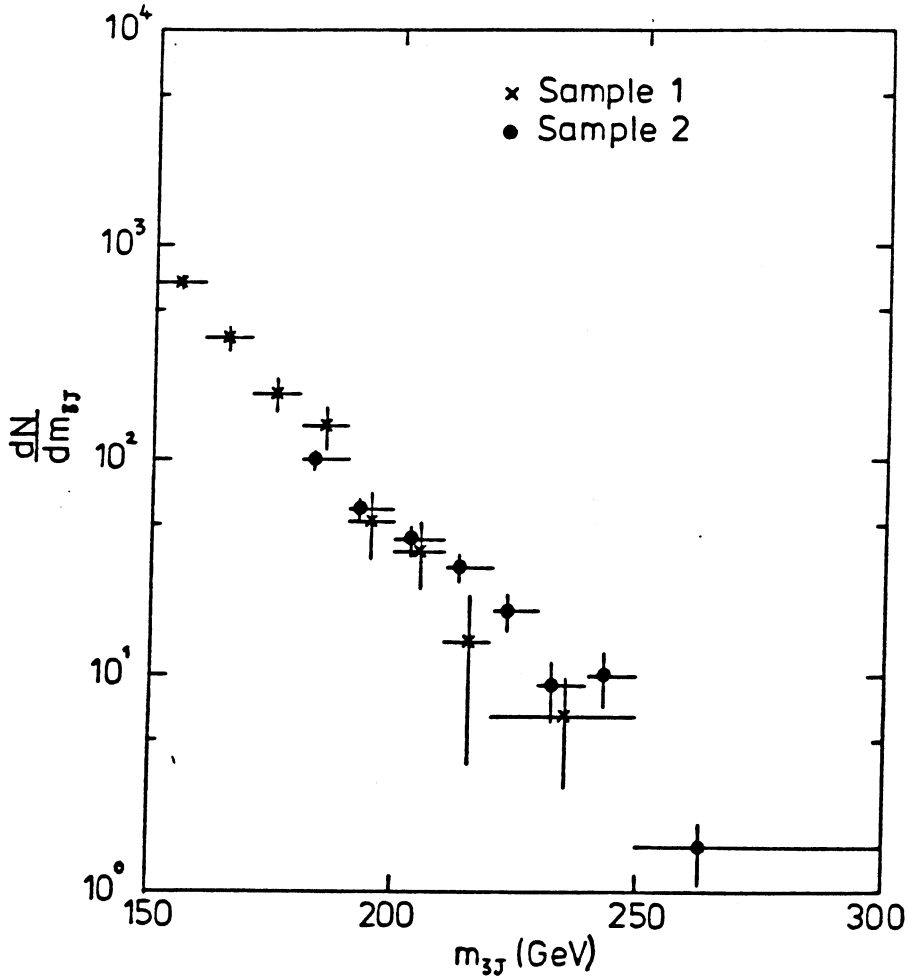

Figure 5.7 Three-jet mass spectrum for sample 1 (crosses) and sample 2 (full circles).

Monte Carlo as described in §4.4 and Appendix B to generate three-jet events (according to the three-parton matrix element) with massless jets. The jet 4-vectors in each event are smeared as described previously and the event is re-analysed. The smearing factors $F(m_{3J})$ are obtained by comparing the generated mass spectrum to the 'reconstructed' spectrum and the results are plotted in Figure 5.8 versus the three-jet mass. Over the mass range considered there is only a slight mass dependence. This is perhaps surprising as one might expect the effects of smearing to be larger for the three-jet events.

Applying these factors to the events in sample 2 with $m_{3J} = 180 - 250$ GeV

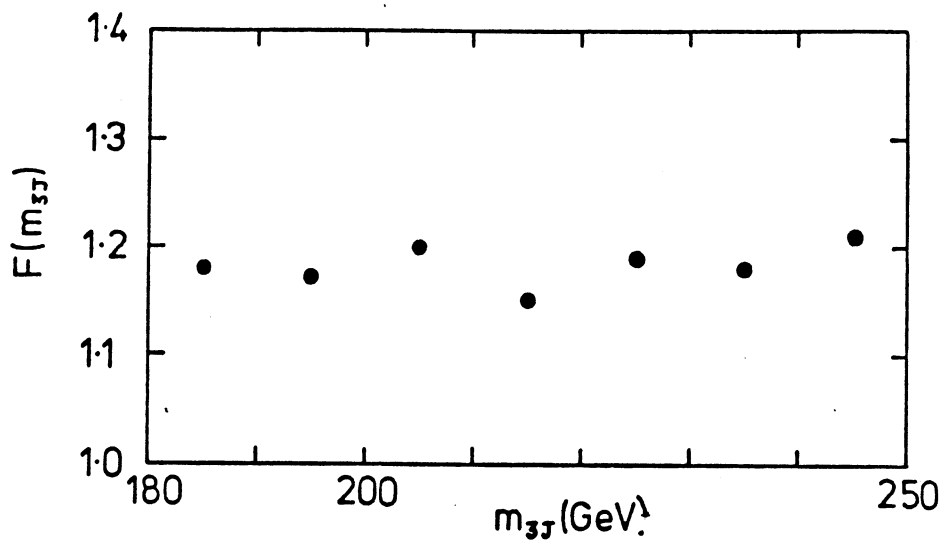

Figure 5.8 Smearing factors $F(m_{3J})$ as a function of the three-jet mass.

and performing a least-squares fit we obtain

$$\begin{aligned} \ln A &= 49 \pm 4 \\ n &= 8.5 \pm 0.8. \end{aligned} \tag{5.13}$$

This result indicates that the three-jet spectrum falls less steeply than the two-jet spectrum where $n = 9.96$ but the two results are consistent within errors. The final mass spectrum for sample 2 is plotted in Figure 5.9 along with the results of the fit.

5.5 The three-jet Dalitz plot and angular distributions

We can now combine both samples and compare the Dalitz plot and angular distributions obtained with the leading order predictions. In Figure 5.10 we show the Dalitz plot for the events, x_4 vs x_3. The projections are compared with the leading order QCD curves obtained as described in §5.1 and also with three-body phase space, i.e., $|\mathcal{M}|^2 = 1$, both normalized to the data. On the scatter plot the two-jet singularity, $x_3 \to 1, x_4 \to 1$ can be seen clearly as an increase in density. If we fix x_4 and allow x_3 to approach its limiting value of one then jet-4 and jet-5 become increasingly collinear. An increase in event rate under these

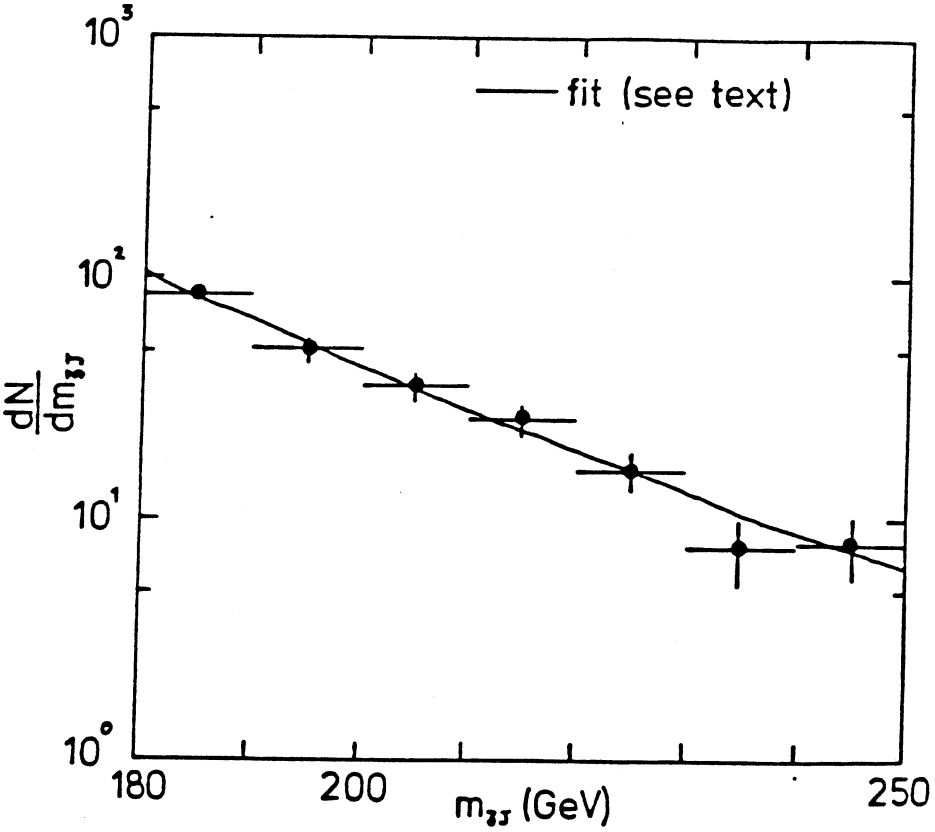

Figure 5.9 Final three-jet mass spectrum for sample 2.

conditions would be indicative of the presence of final-state bremsstrahlung. If from the scatter plot in Figure 5.10 we look between $x_4 = 0.64 - 0.74$ and divide this region into two halves then we see no significant excess of events in the region $x_3 = 0.83 - 0.9$ compared to the region $x_3 = 0.76 - 0.83$. The conclusion is therefore that our choice of cuts tends to bias against obvious final-state radiation.

The scatter plot of ψ vs $\cos\theta_3$ is plotted in Figure 5.11. The shape of the $\cos\theta_3$ distribution is similar to that obtained for the two-jet sample although the singularity as $|\cos\theta_3| \rightarrow 1$ is less steep than for the corresponding two-jet singularity. As the distribution is symmetric in ψ ($\psi \rightarrow -\psi$) it has been folded and plotted from $|\psi| = 0^0$ to $|\psi| = 180^0$. As a function of ψ the event rate increases as $|\psi| \rightarrow 0^0$ and $|\psi| \rightarrow 180^0$. This corresponds to the configuration when jet-4 and jet-5 are in the same plane as jet-3 and the spectator jets, meaning that jet-5 is at its closest to the beam direction. This is the situation preferred by initial-state radiation. The projections are again compared with the leading order QCD curves normalized to the data.

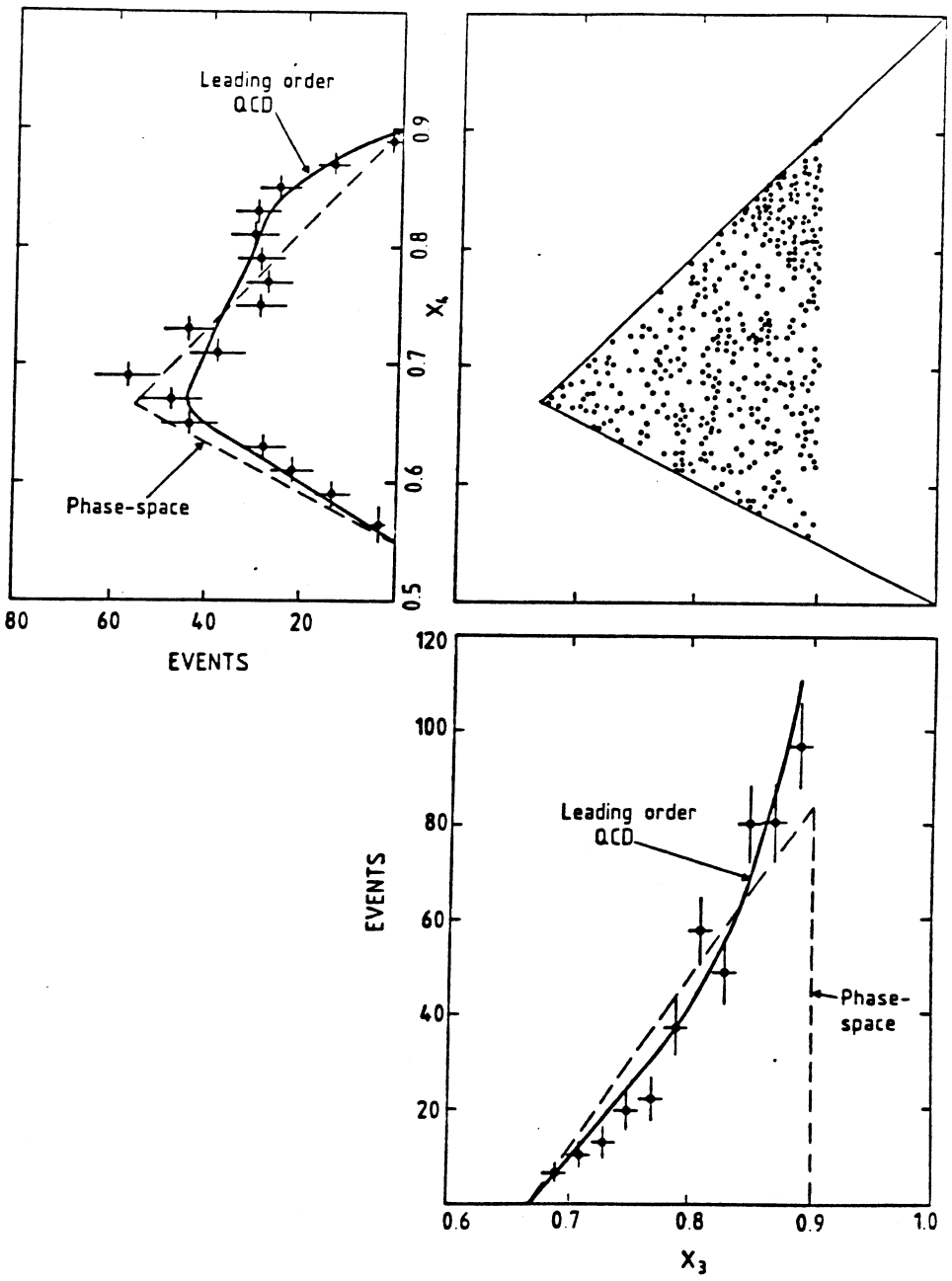

Figure 5.10 Three-jet Dalitz plot, x_4 vs x_3.

For both angular distributions the agreement with the leading order QCD predictions is only qualitative. The observed behaviour is identical to that seen in the two-jet angular distributions. It seems not unreasonable that the same non-scaling effects are required here as were needed in the two-jet distribution.

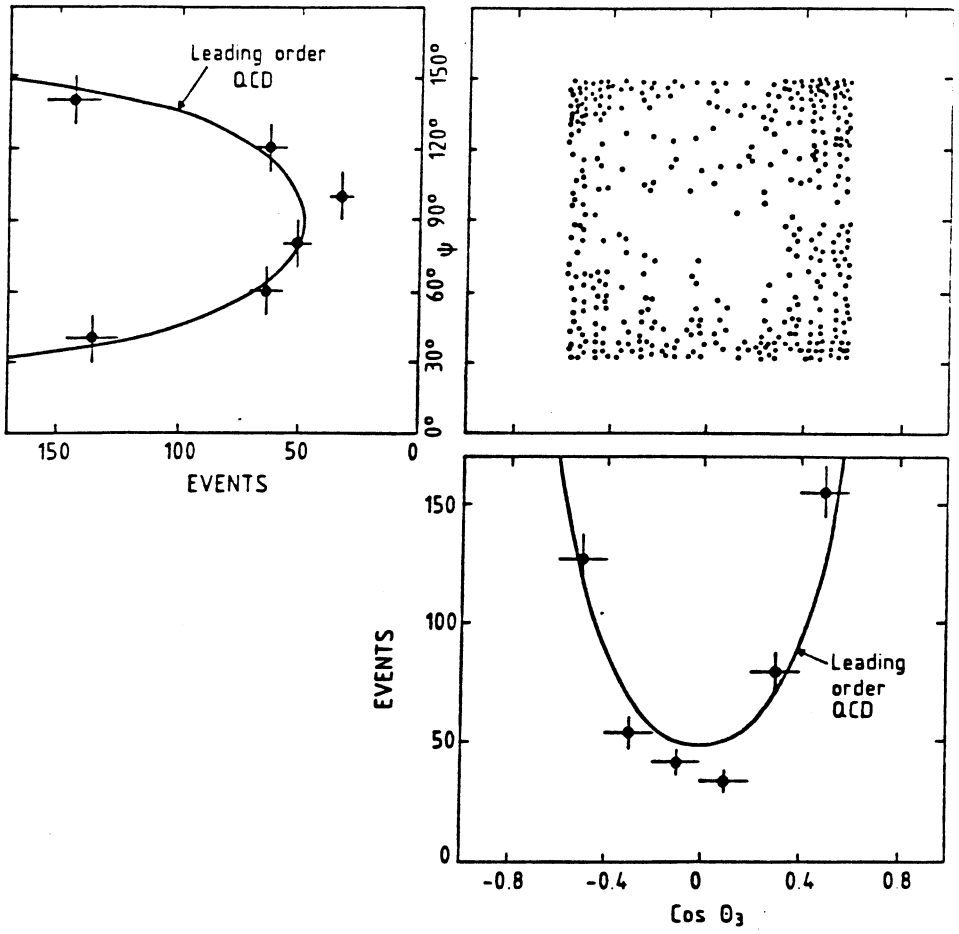

Figure 5.11 Three-jet angular distributions, ψ vs $\cos\theta_3$.

First we have to check whether this behaviour is due to the effects of resolution. We use the Monte Carlo described previously (§5.4 and Appendix B) to compare the generated angular distributions to the 'reconstructed' ones. The quantity $F(\cos\theta_3)$ is plotted versus $\cos\theta_3$ in Figure 5.12a and in Figure 5.12b $F(\psi)$ is plotted vs $|\psi|$. Both plots are fairly flat over the whole angular range showing that there are no major systematic effects present.

In the three-jet case the choice of scale is more complicated as the effect is observed in both the $\cos\theta_3$ and ψ distributions and this suggests that any choice has to be a function of both of these variables. In the two-jet case the scale $\hat{t}$ or P_T^2 is effectively the factor in the denominator of the matrix element. Analagous to this we choose for the kinematic form of the scale the ten dot products which

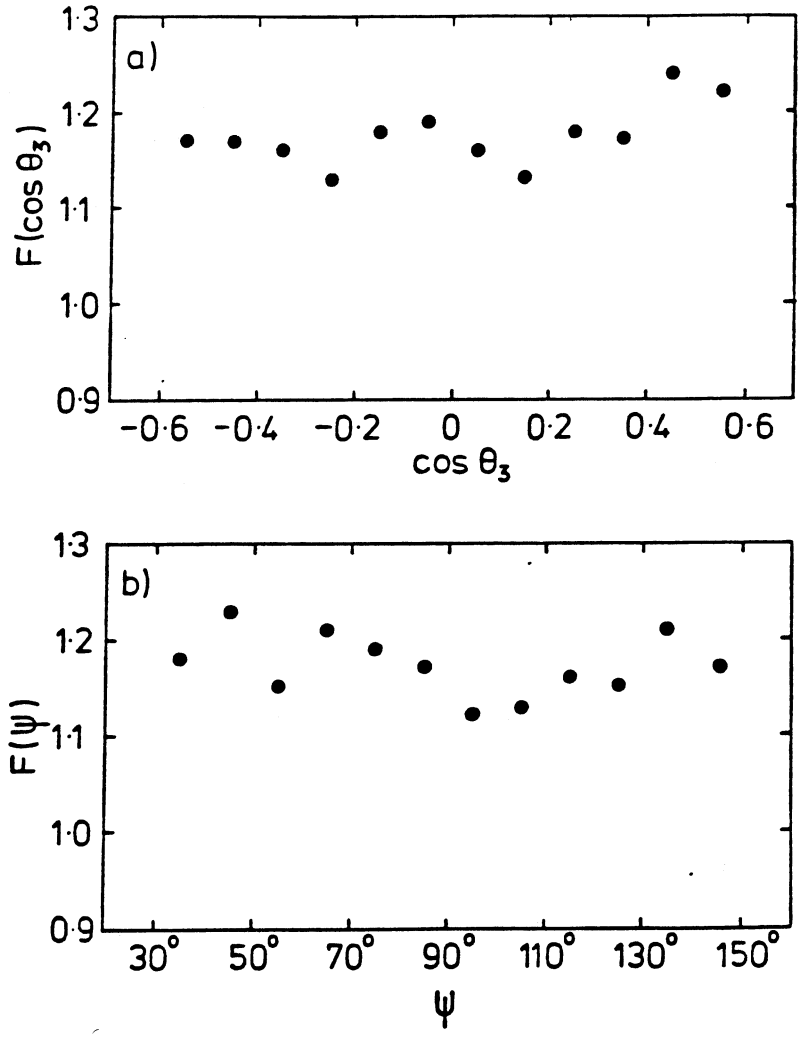

Figure 5.12 Smearing factors, a) $F(\cos\theta_3)$, b) $F(\psi)$.

form the denominator of the $gg \rightarrow ggg$ matrix element, namely

$$q^2 = \frac{\hat{s}A}{4}[(12)(13)(14)(15)(23)(24)(25)(34)(35)(45)] \qquad (5.15)$$

where A is a parameter to be determined. The dot products have been redefined to be dimensionless quantities where $(ij) = x_i x_j(1 - \cos\theta_{ij})$ with θ_{ij} the angle between partons i and j. The factor $\hat{s}$ ensures that the formula is dimensionally correct. If any of the dot products in equation 5.15 become small then so does q^2 and $\alpha_s(q^2)$ will increase.

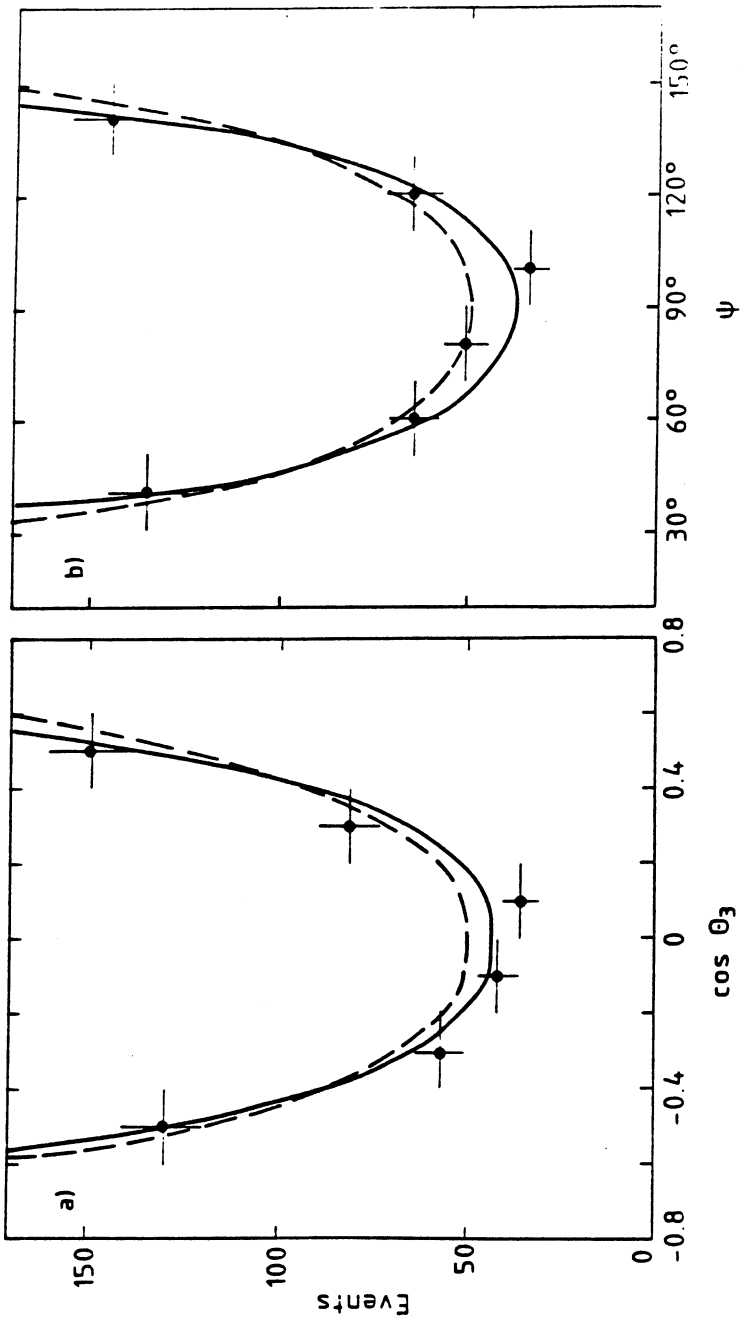

Figure 5.13 Angular distributions corrected for smearing, a) $\cos\theta_3$, b) ψ.
For curves see text.

Using this definition of q^2 we can include a factor of $\alpha_s^3(q^2)F(x_1,q^2)F(x_2,q^2)$ into the Monte Carlo (§5.1) to obtain modified curves. For the $F(x_1,q^2)F(x_2,q^2)$ weight we use the structure functions determined by the CDHS Collaboration[60], extrapolated in q^2. In Figure 5.13a the $\cos\theta_3$ distribution is plotted (after unsmearing and renormalization to 492.2 events). The solid curve is the theoretical prediction including non-scaling effects for $A = 2.5$, with the mean q_{3J} being $0.26m_{3J}$. Almost identical curves are obtained for other choices of A such as 1.5 and 7.5, giving $\langle q_{3J}\rangle \sim 0.2m_{3J}$ and $0.45m_{3J}$ respectively, and hence are not shown. This is identical to the two-jet situation where a wide range of possible values for A gave reasonable agreement with the data. There is a clear deviation from scaling behaviour (dashed curve) with a tendency for the non-scaling curve to become flatter around $\cos\theta_3 = 0$. Figure 5.13b shows the $|\psi|$ distribution for the data. The solid curve is obtained using $A = 2.5$ as above and again the curves for the other choices of A are almost identical. Here the deviation from perfect scaling (dashed curve) is more dramatic.

We shall see in Chapter 6 that some of these choices for A (and hence q^2) will be excluded by the need to predict the observed three-jet event rate relative to the two-jet rate.

5.6 Asymmetries arising from quark-gluon scattering

The only way that asymmetries can arise in $2 \rightarrow 3$ processes is if there are two distinct parton types, namely quarks and gluons[65]. So from the three dominant subprocesses the only subprocess that can give rise to an asymmetry is $qg \rightarrow qgg$.

In events that have large longitudinal boosts one of the partons, typically the quark(antiquark) carries much more momentum than the other. As the gluon is more likely to undergo bremsstrahlung than the quark the highest energy jet (in the c.m.s) will tend to be the quark jet rather than the gluon jet. There are two possible configurations, events with positive boosts (Figure 5.14a) and those with negative boosts (Figure 5.14b). In Figure 5.14 we have defined $\cos\theta_3$ so that it is positive when jet-3 points in the same direction as the boost. Looking at Figure 5.14 it can be seen that in both a) and b) case (i) is more likely than

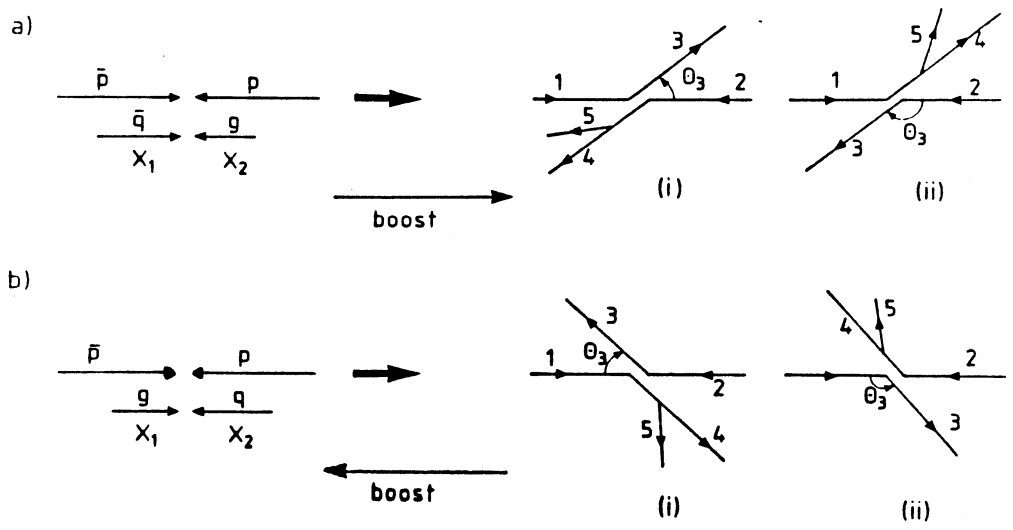

Figure 5.14 Event configurations for large boosts, a) positive boost, b) negative boost.

case (ii) due to the gluon being more likely to radiate than the quark. So we expect to observe an excess of events for which $\cos\theta_3 > 0$ over those where $\cos\theta_3 < 0$. Using the predicted angular distributions from the Monte Carlo calculation described in §5.1 the predicted asymmetry for pure $\bar{q}g$ (gq) scattering is +0.086(−0.086) (allowing for the effects of including all possible final state configurations). Averaging over $\bar{q}g$ and gq the overall asymmetry is reduced to +0.024 and falls to +0.01 when the other two main subprocesses are included. There will also be a similar asymmetry in the variable ψ with more events having $|\psi| < 90^0$ than having $|\psi| > 90^0$.

Using the $\cos\theta_3$ and ψ distributions, after removing the effects of resolution, the measured asymmetries are

$$\begin{aligned} A(\cos\theta_3) &= 0.075 \pm 0.055 \\ A(\psi) &= 0.021 \pm 0.055. \end{aligned} \tag{5.14}$$

neither asymmetry being significant ($\sim 1.5\sigma$).

One could attempt to enhance the fraction of quark-gluon events in the data sample by only using events with large boosts but this reduces the sample size quite substantially. Therefore any result obtained has even less significance due to its increased error.

5.7 Summary

In this chapter we have studied some of the properties of a small subset of three-jet events from the total data sample. The mass spectrum of the events is well represented by a power law of the form $dN/dm_{3J} = 1.7 \times 10^{21}/m_{3J}^{8.5}$. The Dalitz plot and angular distributions for the sample are in qualitative agreement with the predictions of the leading order QCD bremsstrahlung formulae. The ψ distribution shows evidence for initial-state radiation but the choice of cuts seems to bias against obvious final-state radiation. Both of the angular distributions show evidence of non-scaling behaviour and are well described by an appropriate choice of scale. Finally the evidence for asymmetries due to quark-gluon scattering is not very strong, the measured values being consistent with zero asymmetry.

6. COMPARISON OF TWO-JET AND THREE-JET PRODUCTION

Having defined samples of two-jet and three-jet events we can use these to investigate the relative rates of production at fixed subprocess centre-of-mass energy $\sqrt{\hat{s}}$. We can measure the ratio of the number of three-jet events to the number of two-jet events for fixed mass and then use this experimental ratio to obtain a value for the strong coupling constant α_s. As the data extends over a fairly large mass range, 150 – 300 GeV for the combined sample then the ratio can be determined for a number of different masses.

6.1 Determination of σ_{2J} and σ_{3J}

In §5.1 we wrote the three-parton differential cross-section as (equation 5.7)

$$\frac{d^4\sigma}{dx_3 dx_4 d\cos\theta_3 d\psi} = \frac{1}{4\pi}\frac{\alpha_s^3}{\hat{s}}|\mathcal{M}'|^2 \tag{6.1}$$

where $|\mathcal{M}'|^2$ was a dimensionless matrix element that was related to the matrix element of Berends et al. (equation 5.6). Defining the denominator on the left-hand side of equation 6.1 to be dV_{3J} then the three-parton subprocess cross-section contained in volume V defined by the cuts is given by

$$\sigma_{3J} = \frac{\alpha_s^3}{\hat{s}}\frac{1}{4\pi}\int_V |\mathcal{M}'| dV_{3J} \tag{6.2}$$

Likewise, the two-parton subprocess cross-section contained in volume V' is given by

$$\sigma_{2J} = \frac{\pi\alpha_s^2}{2\hat{s}}\int_{V'} \Sigma \, d\cos\theta \tag{6.3}$$

where Σ for each subprocess is given in Table 2.1.

Equations 6.2 and 6.3 can be re-written as

$$\sigma_{2J} = \frac{\alpha_s^2}{\hat{s}} C_{2J}$$
$$\sigma_{3J} = \frac{\alpha_s^3}{\hat{s}} C_{3J} \tag{6.4}$$

where C_{2J} and C_{3J} are the dimensionless coefficients obtained by integrating the matrix elements over the phase-space volume and including any constant factors.

Integration of the two-parton subprocesses can be performed analytically as there is only one integration variable $\cos\theta$ and the expressions for Σ are fairly simple. The three-parton subprocesses are much more complicated and integration is over four variables so a Monte Carlo method is employed which will be described briefly.

We use the Monte Carlo calculation described in §5.1 to generate events according to three-body phase-space and determine the value of $|\mathcal{M}'|^2$ for each event. The total volume available for generation is $V_{TOT} = 4\pi^2/3$ and if we let the total number of phase-space points generated be N_{TOT} and the number that satisfy our cuts be N_V then the volume inside our cuts is given by

$$\int_V dV_{3J} = V = V_{TOT} \frac{N_V}{N_{TOT}} \tag{6.5}$$

Then we define an average matrix element $\langle|\mathcal{M}'|^2\rangle_V$ inside the cuts to be

$$\langle|\mathcal{M}'|^2\rangle_V = \frac{\int_V |\mathcal{M}'|^2 \, dV_{3J}}{\int_V dV_{3J}} \tag{6.6}$$

where $\langle|\mathcal{M}'|^2\rangle_V = \sum_V |\mathcal{M}'|^2/N_V$ with $\sum_V |\mathcal{M}'|^2$ being the sum of all the $|\mathcal{M}'|^2$ over volume V. Hence this allows us to write

$$\int_V |\mathcal{M}'|^2 \, dV_{3J} = \frac{\sum_V |\mathcal{M}'|^2 V_{TOT}}{N_{TOT}} \tag{6.7}$$

where the integral on the left is the quantity C_{3J} (after including a factor of $1/4\pi$).

Subprocess	C_{3J}	C_{2J}	C_{3J}/C_{2J}
gg	111.5	110.5	1.01
qg	38.1	48.2	0.79
$q\bar{q}^*$	16.4	21.4	0.76
*$q\bar{q}$ identical flavours only elastic subprocesses only			

Table 6.1 Summary of cross-section coefficients for *loose* cuts.

The results of performing this integration for the three dominant subprocesses are listed in Table 6.1 for the cuts described in §5.2 (referred to as 'loose' cuts) along with the ratio C_{3J}/C_{2J} for each subprocess. As would be expected the two-jet coefficients follow the familiar pattern of $1 : \lambda : \lambda^2$ for the subprocess ratio $gg : qg : q\bar{q}$ with $\lambda \sim 0.44$. The perhaps more surprising observation is that to within $\sim 30\%$ the three-jet coefficients also follow this rule. One might expect that the extra quark-gluon vertex present in $qg \rightarrow qgg$ or $\bar{q}q$ scattering would introduce an extra factor of 0.44 but this turns out not to be the case. This means that the three-jet cross-section can be represented by a single effective subprocess[65] where

$$d\sigma_{3J} \approx F(x_1)F(x_2)\; d\sigma_{gg\rightarrow ggg} \tag{6.8}$$

where $F(x) = G(x) + \lambda(Q(x) + \bar{Q}(x))$ with $\lambda \sim 0.34$ for our phase-space volume and choice of cuts.

This universality breaks down further for the $2 \rightarrow 4$ processes where the approximation is only good to within a factor 2[66]. For the two-jet subprocesses the deviations from $\lambda = 0.44$ increase as the scattering angle becomes large. Assuming this is also true for the three-jet subprocesses then a useful variable in which to study this variation of λ is the transversality T[65] where

$$T = \frac{1}{2}\sum_{i=3}^{5} x_i \sin\theta_i, \quad 1 \geq T \geq 0 \tag{6.9}$$

with x_i and θ_i as defined in §5.1. The ratio λ depends on T and the approximation to the two-jet case improves as T decreases. The maximum disagreement occurs

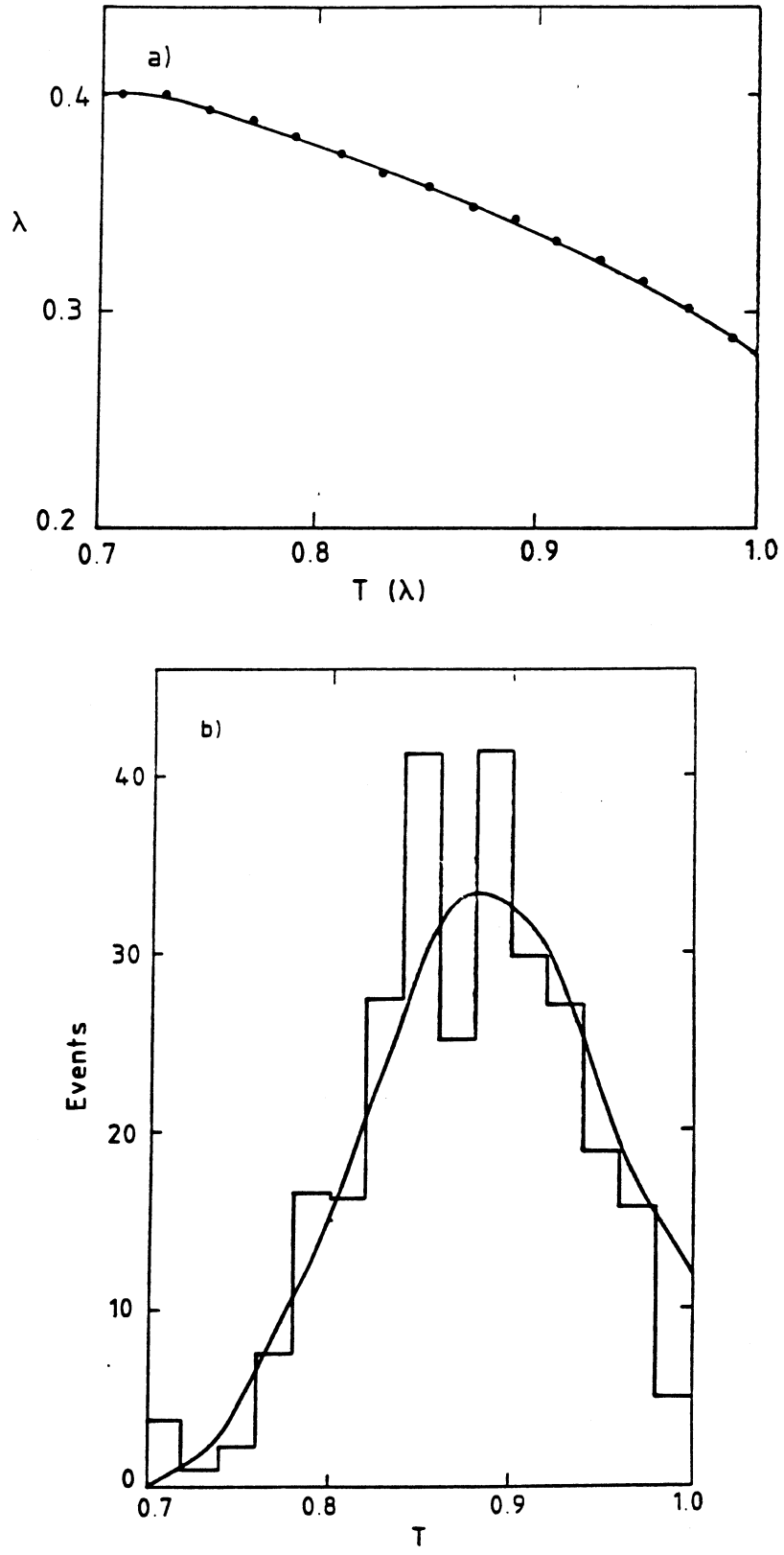

Figure 6.1 a) The quantity λ plotted as a function of the transversality T.
b) The transversality distribution for sample 2. For curve see text.

when $T = 1$ and $x_3 = x_4 = x_5 = 2/3$ with $1 : \lambda : \lambda^2 \equiv 1 : 0.273 : 0.142$. In Figure 6.1a we plot the ratio $qg/gg \equiv \lambda$ as a function of T for values of T between 0.7 and 1.0 (the lower limit being defined by our choice of cuts). We also plot the transversality distribution for sample 2 in Figure 6.1b and compare it with the prediction from the Monte Carlo calculation (§5.1). The mean transversality of the data sample is $\langle T \rangle = 0.87 \pm 0.07$.

6.2 Three-jet to two-jet ratio, σ_{3J}/σ_{2J}

To obtain the experimental ratio as a function of mass we simply divide the number of three-jet events of a particular mass by the corresponding number of two-jet events. We will also require a theoretical calculation of σ_{3J}/σ_{2J}.

We can write the ratio as

$$\frac{\sigma_{3J}}{\sigma_{2J}} = \frac{\alpha_s^3(\mathrm{q}_{3J}^2)}{\alpha_s^2(\mathrm{q}_{2J}^2)} \frac{F(x_1, \mathrm{q}_{3J}^2) F(x_2, \mathrm{q}_{3J}^2)}{F(x_1, \mathrm{q}_{2J}^2) F(x_2, \mathrm{q}_{2J}^2)} \left\langle \frac{C_{3J}}{C_{2J}} \right\rangle \tag{6.10}$$

where $\langle C_{3J}/C_{2J} \rangle$ is the value of the ratio of cross-section coefficients averaged over incoming parton types for each mass bin, and F is an effective structure function. It can be easily seen that if $\mathrm{q}_{3J} = \mathrm{q}_{2J} = \mathrm{q}$ then equation 6.10 simplifies to

$$\frac{\sigma_{3J}}{\sigma_{2J}} = \alpha_s(\mathrm{q}^2) \left\langle \frac{C_{3J}}{C_{2J}} \right\rangle \tag{6.11}$$

If on the other hand the scales are different then we have to include the structure function contribution, averaged over boost. In Figure 6.2a and 6.2b we plot the ratio σ_{3J}/σ_{2J} as a function of mass and boost respectively. Over the range plotted the data show no significant mass or boost dependence. Also shown are four theoretical predictions, obtained using $\Lambda_{QCD} = 200$ MeV. In both figures the solid curve represents the case where $\mathrm{q}_{3J} = \mathrm{q}_{2J} = 0.45\sqrt{\hat{\mathrm{s}}}$ (the 0.45 is obtained by taking $\mathrm{q}_{2J}^2 = -\hat{\mathrm{t}}$ and determining the mean q value and $\sqrt{\hat{\mathrm{s}}}$ for the data). For both mass and boost this choice does not provide a very good description of the data, with the curve falling significantly below the points in both plots. The other three curves are obtained by taking a significantly lower

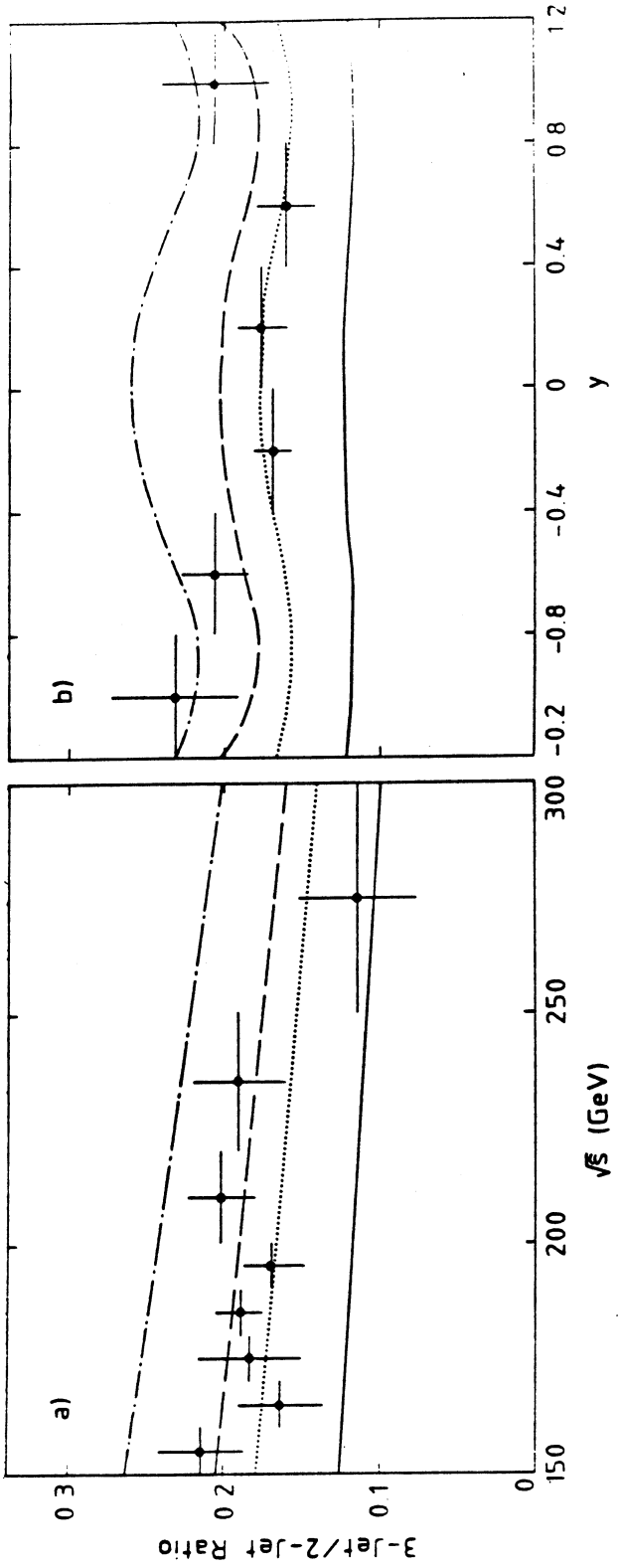

Figure 6.2 The ratio σ_{3J}/σ_{2J} as a function of a) mass and b) boost. For curves see text.

scale for the three-jet events, while keeping $q_{2J} = 0.45m_{2J}$. The uppermost curve (dash-dotted) corresponds to $q_{3J} = 0.2m_{3J}$ and clearly this choice is too low as it predicts a much higher ratio than is observed. The dashed curve uses $q_{3J} = 0.26m_{3J}$ and this choice clearly provides a good description of the data as does the dotted curve for which $q_{3J} = 0.3m_{3J}$. The data plotted versus boost seem to favour the dotted curve rather than the dashed one. It is therefore apparent that although all these choices gave a good description of the angular distributions they give vastly different values for the ratio.

Both these plots clearly demonstrate that in order to reproduce the observed rate of three-jet events, the q^2-scale that applies to the three-jet events has to be substantially lower than for two-jet events of the same mass. It is interesting to notice here that, unlike in the determination of the two-jet q^2-scale, we are able to use the overall normalization provided by the ratio to limit possible choices of scale. It should be noted that all these predictions apply for a particular value of Λ_{QCD}, namely 200 MeV. Choosing a larger value of Λ_{QCD} rather than changing the scale would produce very similar results.

6.3 Determination of $\alpha_s(q^2)$

We are now in a position to extract a value for the strong coupling constant $\alpha_s(q^2)$ using the whole data sample. We determine $\alpha_s(q^2)$ by inverting equation 6.11 to give $\alpha_s(q^2) = (\sigma_{3J}/\sigma_{2J}) \times \langle C_{3J}/C_{2J} \rangle$. However this formula applies only when $q_{2J} = q_{3J}$ and as we have just shown in §6.2 this is probably not the case. To allow for differences in scales, as well as a lack of precise knowledge about the form of the scale, we introduce a ratio K_{3J}/K_{2J} where K_{2J} and K_{3J} are the factors by which the leading order cross-section would have to be multiplied by to give the observed cross-section. So what we actually determine is

$$\alpha_s(L.O.) = \alpha_s \times \left(\frac{K_{3J}}{K_{2J}}\right) \tag{6.12}$$

As a cross-check of the consistency of our results we define a second event

Subprocess	C_{3J}	C_{2J}	C_{3J}/C_{2J}
gg	45.3	45.2	1.00
qg	14.8	19.1	0.78
$q\bar{q}$*	6.7	8.4	0.80
*$q\bar{q}$ identical flavours only elastic subprocesses only			

Table 6.2 Summary of cross-section coefficients for *tight.* cuts

sample with more restrictive selection criteria of

$$\begin{aligned} &\text{2-jet events:} && \cos\theta < 0.6 \\ &\text{3-jet events:} && x_3 < 0.9 \\ & && \cos\theta_3 < 0.6 \\ & && 55^0 < \psi < 125^0 \end{aligned}$$

which are referred to as 'tight cuts'.In Table 6.2 are given the corresponding values for C_{2J}, C_{3J} and $\langle C_{3J}/C_{2J}\rangle$. By chance the tight cuts give almost the same values for $\langle C_{3J}/C_{2J}\rangle$ as for the loose cuts.

Table 6.3 contains a summary of the results obtained for $\alpha_s(L.O.)$ from three different samples. Also given are the weighted number of events in each sample, with observed numbers of events in parenthesis, and the value of σ_{3J}/σ_{2J} for the samples with the value of $\langle C_{3J}/C_{2J}\rangle$ underneath. The first two results are straightforward comparisons for the loose and the tight samples respectively and hence assume that $q_{2J} = q_{3J}$. The values obtained for $\alpha_s(L.O.)$ are consistent with each other as would be expected but are higher than one might expect at these energies. However, the value of K_{3J}/K_{2J} is probably large as we have shown that $q_{2J} \neq q_{3J}$. What we can do is make an attempt to compare two samples whose q^2's are more similar. We have shown that the data are consistent with $q_{3J} \sim 0.3m_{3J}$ and it turns out that if we take two-jet events with $0.8 > \cos\theta > 0.6$ ((loose − tight) sample) then with $q_{2J}^2 = -\hat{t}$ we obtain $q_{2J} \sim 0.38m_{2J}$. As this is slightly larger than the scale appropriate to the whole three-jet sample we use the tight three-jet sample for our comparison. The third line of Table 6.3 gives

the result of making this comparison, and it can be seen that the value obtained for $\alpha_s(L.O.)$ is now $\sim 25\%$ lower than for the other comparisons.

Trying to equalize the scales is the same as trying to make $K_{3J}/K_{2J} \rightarrow 1$. It should be emphasised that until higher order calculations exist for $2 \rightarrow 3$ processes the value of α_s that is measured will always contain unknown K-factors. What is important here is not so much the actual value of $\alpha_s(L.O.)$ obtained but the indication that it decreases if one tries to make the q^2-scales more equal.

In Table 6.3 the second of the two errors on the α_s measurements is the estimated systematic uncertainty. Although uncertainties in energy scale and smearing due to energy resolution have a large effect on individual event rates they have a much smaller effect on the ratio. Also systematic effects such as luminosity measurement and filter efficiency tend to cancel when taking the ratio of the event samples. We have included an error of $\pm 15\%$ to allow for any residual differences between the resolution for three-jet events and two-jet events. This is because three-jet events may sample parts of the calorimeter which have a different resolution to the parts sampled by the two-jet events. Added in quadrature to this is an error of $\pm 10\%$ which covers any ambiguity over sample definition. Both the two- and three-jet samples are inclusive, they include events with ≥ 2 jets and ≥ 3 jets respectively. It is not clear whether the extra jet should be combined with one of the other jets, as was discussed in §4.2 and §5.2, because one does not know which parton the third (or fourth) jet was originally radiated from. The other possibility is to define exclusive samples of events (two and only two or three and only three jets), as has been done by the UA2 Collaboration[67]. The quoted error also covers any algorithm dependence, for example 'cross-talk' between jets leads to their axes being reconstucted incorrectly.

6.4 Summary

In this chapter we have demonstrated that the three-jet cross-section can be represented by a universal subprocess as with the two-jet cross-section. The measured ratio σ_{3J}/σ_{2J} indicates that the q^2-scale appropriate to the three-jet event sample is lower than that for the two-jet events of the same mass. Unless

Samples compared	Number of two-jet events	Number of three-jet events	σ_{3J}/σ_{2J} $\langle C_{3J}/C_{2J}\rangle$	$\alpha_s \times (K_{3J}/K_{2J})$
$\frac{\sigma_{3J}(loose)}{\sigma_{2J}(loose)}$	2668.3 (2657)	487.6 (398)	0.183 ± 0.10 0.81	$0.226 \pm 0.012 \pm 0.041$
$\frac{\sigma_{3J}(tight)}{\sigma_{2J}(tight)}$	873.0 (872)	174.1 (134)	0.199 ± 0.018 0.81	$0.246 \pm 0.022 \pm 0.044$
$\frac{\sigma_{3J}(tight)}{\sigma_{2J}(loose) - \sigma_{2J}(tight)}$	1801.3 (1785)	174.1 (134)	0.097 ± 0.009 0.53	$0.183 \pm 0.017 \pm 0.032$

Table 6.3 Summary of results for σ_{3J}/σ_{2J} and $\alpha_s \times (K_{3J}/K_{2J})$.

an attempt is made to take this difference into account then the value obtained for $\alpha_s(L.O.)$ is higher than would be expected at these energies.

7. CONCLUDING REMARKS

This chapter contains a summary the important results arising from the analysis presented in this thesis.

7.1 Two-jet production

The two-jet angular distributions are found to be in qualitative agreement with leading order QCD predictions assuming α_s is a constant. The deviations can be explained by allowing α_s and $F(x)$ to be functions of q^2 and choosing $q^2 = -\hat{t}$. Over the mass range considered it is found that weighting by $\alpha_s^2(q^2)$ *or* $F(x_1, q^2)F(x_2, q^2)$ produces identical shapes for the theoretical distributions, but that both effects are required to describe the data. Attempts to use the shape of the angular distribution alone to constrain possible forms for q^2 were not very successful. This was attributed to the very slow variation of the shape of the theoretical angular distribution over many orders of magnitude in q^2 and hence most choices came within the measurement errors. One possible way of improving this determination might be to use the overall normalization from the mass-spectrum. The other method would be to use the calculations by Ellis and Sexton[38] of the corrections to $O(\alpha_s^3)$ for the two-jet cross-section to determine the q^2-scale analytically.

7.2 Three-jet production

Any three-jet event can be described in terms of four independent dimensionless variables plus the three-jet mass. The three-jet Dalitz plot does not show conclusive evidence for final- state bremsstrahlung. It is assumed that requiring all the jets to be well separated biases against final-state radiation. The ψ distribution however shows clear evidence for initial-state bremsstrahlung. In both the angular distributions the agreement with leading order QCD is again only qualitative. Using an appropriate choice of scale it is possible to introduce noticeable non-scaling effects and hence obtain much better agreement. Again, the data does not differentiate between scales of different magnitudes, all choices giving

reasonable agreement. The measured forward-backward asymmetry which could be attributable to quark-gluon scattering is consistent with zero. A much larger event sample would be required to enable a reasonable sub-sample containing a higher fraction of quark-gluon events to be selected.

7.3 The ratio σ_{3J}/σ_{2J}

The dominant three-parton subprocesses are found to follow the same geometrical progression as the two-jet subproceses to within $\sim$ 30%. This means that the three-jet cross-section can be represented by a universal subprocess, chosen to be $gg \rightarrow ggg$, and an effective structure function. The choice of dimensionless variables to define the three-jet and two-jet samples make it straightforward to compare the event rates and to obtain the theoretical prediction for the ratio. For a given choice of Λ_{QCD} the measured ratio as a function of mass and boost is not consistent with the choice of identical scales for the two processes, but suggests that the three-jet events are characterized by a much lower q^2-scale. The magnitude required is fully consistent with the choices of scale made for the angular distributions. A straight comparison of samples yields a value for $\alpha_s(q^2)$ that seems too high for the masses under consideration. This can be explained by postulating substantial higher-order corrections, $\sim$ 30%, coming from the non-cancellation of the structure functions and the factor of $\alpha_s^2(q_{3J}^2)/\alpha_s^2(q_{2J}^2)$. Trying to select two samples of events where the scales are more equal leads to a substantial reduction in the measured value of $\alpha_s(q^2)$.

7.4 The future

In order to obtain more precise measurements of α_s from hadron colliders requires the calculation of the three-jet cross-section to $O(\alpha_s^4)$. The calculations for the $2 \rightarrow 4$ subprocesses to $O(\alpha_s^4)$ already exist[35] but the virtual corrections have not yet been calculated. An analysis of the type performed on three-jet events could also be applied to four -jet events. Here also there is the possibility of looking for double-parton scatters which will have different properties from four-jet events coming from bremsstrahlung. The ratio $R = \sigma(\chi = 1-4)/\sigma(\chi = 4-9)$

computed for different mass ranges opens up the possibility of looking for high mass resonances decaying to jet-jet which will increase the cross-section between $\chi = 1 - 4$ relative to $\chi = 4 - 9$ due to the more isotropic nature of their angular distributions.

There is clearly considerable scope for studies of jet production at the CERN $p\bar{p}$ collider as well as in the future at the TEVATRON and the SSC but theoretical calculations are required to enable comparisons to be made to anything other than leading order in α_s.

APPENDIX A

This Appendix contains a description of the basic data selection procedure and the corrections and quality cuts applied before the final two-jet and three-jet selections are made.

A1 The 1983 data sample

During the 1983 Collider run a total integrated luminosity of 108 nb^{-1} was recorded by the UA1 experiment at a centre of mass energy of 546 GeV. This data was taken using a variety of triggers in the trigger processor (described in §3.8) to select possible electron candidates and high E_T jets. There were three major triggers involving the calorimeters,

1. Single electron trigger – required $E_T > 10$ GeV in any two adjacent cells of the electromagnetic calorimeter (gondolas or bouchons).
2. Single jet trigger – a small sample (6.1 nb^{-1}) of data were taken using a threshold of $E_T > 15$ GeV in a block of eight gondolas and the two C cells behind them, or a quadrant of the end-cap calorimeters. The rest of the data were taken with a higher threshold of $E_T > 20$ GeV or 25 GeV.
3. Scalar E_T trigger – this required the summed scalar E_T in the central calorimeters ($|\eta| < 1.5$) to exceed 60 GeV.

After processing and full event reconstruction including jet-finding, the total data sample (excluding the 6.1 nb^{-1}) was passed through a filter which re-applied the jet trigger conditions but with a threshold of 30 GeV. This yielded a total of 71,208 events containing high E_T jets.

On average $\sim$ 80% of the energy of a jet is deposited in the electromagnetic calorimeter. This component of the jet is increased by a factor of 1.13 to compensate for the difference in response between hadrons ($\pi^{\pm}$) and electromagnetic particles (π^0) in the electromagnetic calorimeters. This results in 'compensation bias' because a jet with a large electromagnetic component ends up at a higher energy than a jet of the same initial energy but with a large hadronic component.

This results in the filter selecting preferentially those events where there is a high electromagnetic component. As we are not looking at particle composition then we are not affected to a large extent by this problem. However, if gluon jets contain more neutral particles as has been suggested[53] then their energy will be increased more than for quark jets.

As well as the usual cuts to remove bad events such as requirements on vertex postion, two further quality cuts were applied to the sample. The first is a limit on the total energy of the event to remove double interactions, events with $E_{TOT} > 600$ GeV are removed. The second cut removes beam halo and cosmic ray events, and requires that the significance of the missing transverse energy be less than $2.5\sigma_m$ where

$$\sigma_m = \frac{E_T^m}{0.7\sqrt{|\sum E_T|}}. \qquad (A1)$$

These two cuts remove about 98% of bad events from the final sample used for analysis.

A2 The 1984 data sample

In 1984 an integrated luminosity of 263 nb^{-1} was recorded at a centre of mass energy of 630 GeV. Again the three major calorimeter triggers were single electron, single jet and total scalar E_T with the following thresholds

1. Single electron – $E_T > 10$ GeV.
2. Single jet – $E_T > 25$ GeV (with some data at $E_T > 30$ GeV, depending on the beam luminosity).
3. $|\sum E_T| > 80$ GeV in the central calorimeters, $|\eta| < 1.5$.

There was also some data taken ($\sim$ 40 nb^{-1}) which required two hadronic clusters each of transverse energy > 15 GeV. All the events were processed and fully reconstructed and then passed through a variety of filters to select various types of events, e.g.,electrons, jets, missing transverse energy. The data presented here was obtained through the single jet and scalar E_T selection, this required at least one jet of $E_T > 40$ GeV *or* $|\sum E_T| > 100$ GeV and yielded 87,752 events.

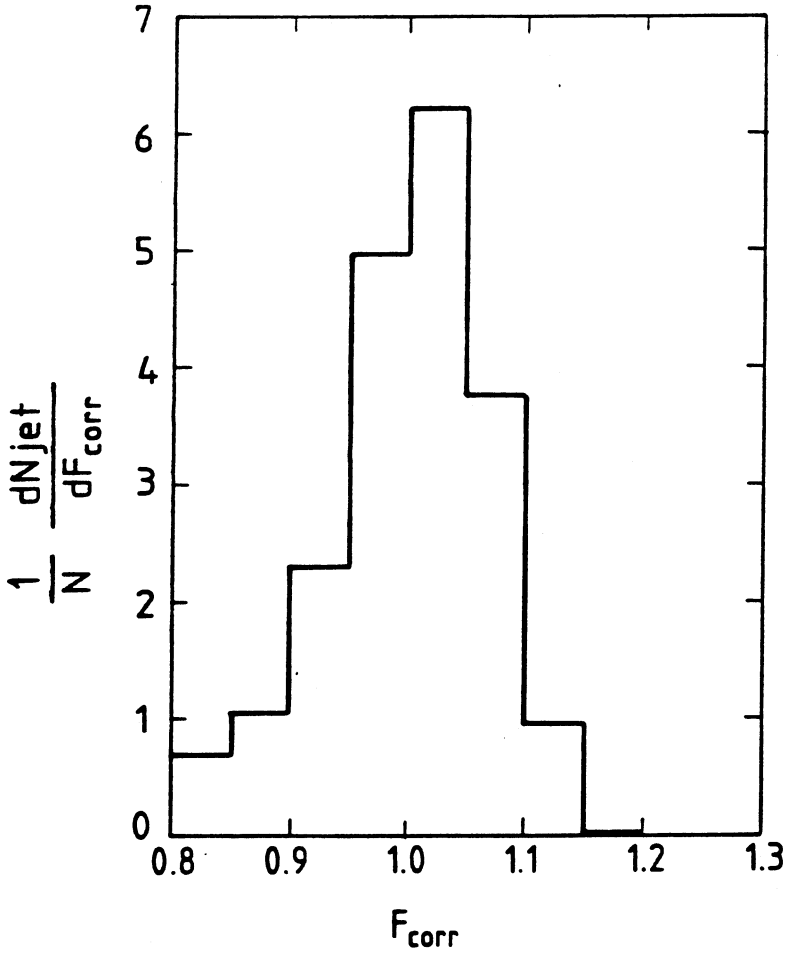

Figure A1 Correction applied per jet for total 1984 data sample.

A number of corrections were then applied to the data, mainly to allow for the effects of ageing of the scintillator in the electromagnetic calorimeters over the course of the data taking period.

1. Ageing of the gondolas – this depended on the integrated luminosity and hence the correction factor increased with time. The maximum ageing was 11%, leading to a maximum correction factor of 1.12.

2. Ageing of the bouchons – again this was luminosity dependent. As the bouchons measure E_T directly a correction was made for the shortening of the attenuation length as well. The maximum correction factor was 1.26.

3. Due to a miscalibration of the hadron calorimeter the energy deposited in the C's and I's had to be reduced by 22%.

Figure A1 shows the correction factor F_{corr} applied per jet for the whole sample.

As before the two quality cuts were applied. The total energy threshold for the double interaction veto was raised to 700 GeV to allow for the increased beam energy while the beam halo and cosmic ray veto remained as before. Only those events which had satisfied the jet requirement ($E_T > 40$ GeV) were used so that the acceptance corrections could be easily evaluated. A breakdown of the effects of these cuts is given in Figure A2.

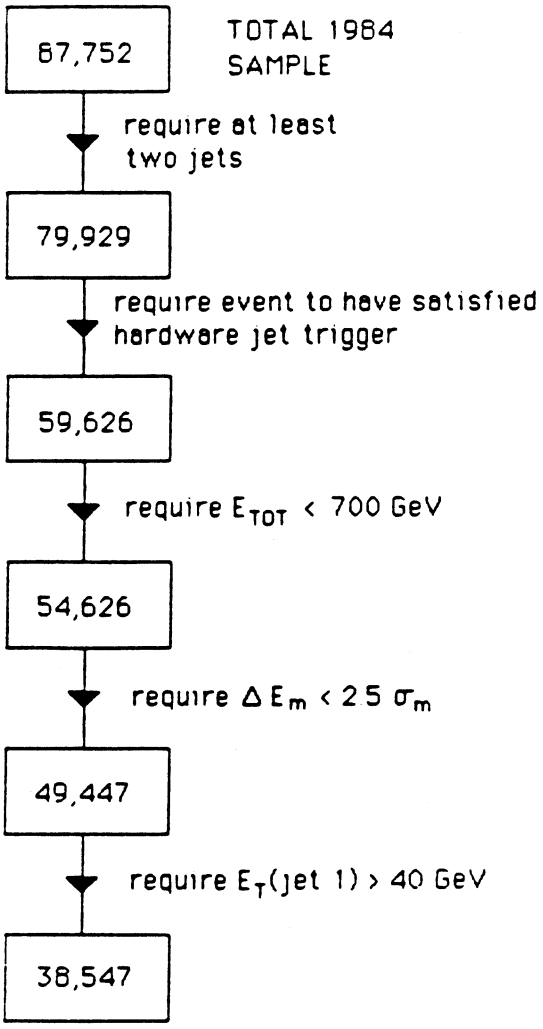

Figure A2 Flow chart showing effects of each of the quality cuts applied to 1984 data sample.

APPENDIX B

This Appendix provides a brief description of the Monte Carlo used to investigate the effects of resolution smearing on the two-jet and three-jet mass and angular distributions. The procedure is as follows.

1. Generate an x_1 and x_2 to represent the two incoming partons, x being the scaled longitudinal momentum. The x's are generated with a $1/R$ distribution, R being a random number between 0 and 1, to produce the correct proportion of high x partons relative to low x partons. For the generation in use here the minimum x generated is 0.02 meaning that the minimum possible mass is 12.6 GeV for $\sqrt{s} = 630$ GeV. The parameterization of the UA1 structure function $F(x) = 6.2e^{-9.5x}$[48] is used to compute a structure function weight for each incoming parton.

2. The mass and boost of the event are determined from the x_1 and x_2.

3. We then generate both a two-jet event and a three-jet event with the same x_1 and x_2, mass and boost.

As the universality of elastic parton-parton subprocesses applies to both two-jet and three-jet cross-sections then a reasonable approximation to reality is obtained by using the $gg \rightarrow gg$ and $gg \rightarrow ggg$ subprocesses only and the effective structure function $F(x) = G(x) + \frac{4}{9}(Q(x) + \overline{Q}(x))$.

4. Two-jet events are generated flat in χ and weighted by the corresponding value of the matrix element while three-jet events are generated flat in x_3, x_4, $\cos\theta_3$ and ψ (see §5.1 for a description of these variables) and again weighted by the appropriate value of $|M|^2$.

5. The event is then transformed to the laboratory frame and the jet 4-vectors are smeared using the jet resolution $\sigma(E_{jet})$ obtained from the study described in §4.1. We generate a normally distributed random number R_N with a mean of zero and a variance of one, and then define a quantity

$$\Delta E = \sigma(E_{jet}) \times R_N. \qquad (B1)$$

So the smeared energy becomes

$$E_{smeared} = \Delta E + E_{generated}. \qquad (B2)$$

This smeared event can then be passed through the same analysis chain as the data, applying the same cuts as are applied to the data and weighting each event by the generated matrix element. We can then compare the generated and smeared events to produce smearing corrections for the various distributions.

REFERENCES

[1] C. Rubbia, 'Experimental observation of the Intermediate Vector Bosons W^+, W^- and Z^0', Les Prix Nobel, 1984 (Almqvist and Wiksell, Stockholm, 1984) p.54
S. van der Meer, 'Stochastic Cooling and the Accumulation of Antiprotons', Les Prix Nobel, 1984 (Almqvist and Wiksell,Stockholm, 1984) p.105

[2] S.L. Glashow, Nuc. Phys. **B22**, (1961) 579.

[3] S. Weinberg, Phys. Rev. Lett. **19**, (1967) 1264.
A. Salam, Proc. 8th Nobel Symposium, Aspenäsgården, 1968 (Almqvist and Wiksell,Stockholm, 1968) p.367

[4] D. Cline, P. McIntyre and C. Rubbia, Proc. Int. Neutrino Conf., Aachen (1976) (Vieweg, Braunschweig, 1977) p.683.

[5] S. van der Meer, internal report CERN ISR-PO/72-31 (1972), unpublished.

[6] G. Carron and L. Thorndahl, internal report CERN ISR-TH/78-11 (1978), unpublished.

[7] G.I. Budker, Proc. Int. Symp. on Electron and Positron Storage Rings, Sacclay, 1966 (PUF, Paris, 1966) p.II-1-1.
G.I. Budker, At. Energ. **22** (1967) 346.

[8] D. Möhl, G. Petrucci, L. Thorndahl and S. van der Meer, Phys. Rep. **58**, (1980) 73.

[9] G. Carron et al., Phys. Letters **77B**, (1978) 353.
G. Carron et al., IEEE Trans. Nuccl. Sci. **NS-26**, No. 3 (1979) 3456.

[10] The staff of the CERN proton-antiproton project, Phys. Letters **107B**, (1981) 306.

[11] K. Alpgard et al., Phys. Letters **107B**, (1981) 310 and 315.
G.Arnison et al., Phys. Letters **107B**, (1981) 320.

[12] S. van der Meer, internal report CERN PS-AA 79-2 (1979) and CERN PS-AA 78-3 (1978), unpublished.

[13] H. Koziol, internal report CERN PS-AA 79-2 (1979), unpublished.
R. Billinge and M.C. Crowley-Milling, IEEE Trans. Nuccl. Sci. **NS-26**, No. 3 (1979) 2974.
S. van der Meer, IEEE Trans. Nuccl. Sci. **NS-26**, No. 3 (1981) 1994.

[14] UA1 proposal, CERN SPSC 78-6/P92 (1978).
UA2 proposal, CERN SPSC 78-8/P93 (1978).
UA3 proposal, CERN SPSC 78-15/P96 (1978).
UA4 proposal, CERN SPSC 78-105/P114 (1978).
UA5 proposal, CERN SPSC 78-10/P108 (1978).
UA6 proposal, CERN SPSC 80-63/P148 (1980).
[15] V. Barnes et al., Phys. Rev. Lett. **12**, (1964) 204.
[16] M. Gell-Mann, Phys. Letters **8B**, (1964) 214.
[17] G. Zweig, CERN 8182/TH.401 and 8419/TH.412 (1964).
[18] J.J. Aubert et al., Phys. Rev. Lett. **33**, (1974) 1404.
[19] J.E. Augustin et al., Phys. Rev. Lett. **33**, (1974) 1406.
[20] S. Okubo, Phys. Letters **5B**, (1963) 163.
J. Iizuka, Prog. Theor. Phys. Suppl. No. 37-38, (1966) 21.
[21] S.L. Glashow, J. Iliopoulos and L. Maiani, Phys. Rev. **D2**, (1970) 1285.
[22] S. Herb et al., Phys. Rev. Lett. **39**, (1977) 252.
[23] E.D. Bloom et al., Phys. Rev. Lett. **23**, (1969) 930.
M. Breidenbach et al., Phys. Rev. Lett. **23**, (1969) 935.
[24] J.D. Bjorken, Phys. Rev. Lett. **179**, (1969) 1547.
[25] R.P. Feynman, Phys. Rev. Lett. **23**, (1969) 1415.
R.P. Feynman, Proc. 3rd Int. Conf. of High-Energy Collisions (1969).
[26] E.M. Riordan et al., SLAC-PUB-1634 (1975).
[27] C.G. Callan and D.J. Gross, Phys. Rev. Lett. **22**, (1969) 156.
[28] D.H. Perkins, Introduction to High Energy Physics (Addison-Wesley 1982).
[29] H. Deden et al., Nuc. Phys. **B85**, (1975) 269.
[30] E. Elsenk, DESY report F22-81/02 (1981).
[31] G. Miller et al., Phys. Rev. **D5**, (1972) 528.
[32] D.J. Gross and F. Wilczek, Phys. Rev. **D8**, (1973) 3633.
H.D. Politzer, Phys. Rep. **14**, (1974) 129.
[33] B.L Combridge, J. Kripfganz and J. Ranft, Phys. Letters **70B**, (1977) 234.
[34] F. Berends et al., Phys. Letters **103B**, (1981) 124.
[35] J.F. Gunion and Z. Kunszt, paper in preparation.
J.F. Gunion and Z. Kunszt, Phys. Letters **159B**, (1985) 167.

Z. Kunszt, paper in preparation.

Z. Kunszt, CERN preprint CERN-TH.4319-85.

S.J. Parke and T.R. Taylor, Fermilab-Pub-85/118-T (1985).

S.J. Parke and T.R. Taylor, Fermilab-Pub-85/162-T (1985).

[36] R.K. Ellis et al., Nuc. Phys. **B173**, (1980) 397.

[37] N.G. Antoniou et al., Phys. Letters **128B**, (1983) 257.

[38] R.K. Ellis and J.C. Sexton, Nuc. Phys. **B269**, (1986) 445.

[39] R.P. Feynman, R.D. Field and G.C. Fox, Phys. Rev. **D18**, (1978) 3320.
R.P. Feynman and R.D. Field, Nuc. Phys. **B136**, (1978) 1.

[40] B. Anderson et al., Z. Phys. **C9**, (1981) 233.

[41] G. Marchesini and B.R. Webber, Nuc. Phys. **B238**, (1984) 1.
B. Webber, Nuc. Phys. **B238**, (1984) 292.

[42] A. Peterson, results from Jade on QCD in e^+e^- annihilations, contribution XVth Rencontre de Moriond (1980).

[43] M. Calvetti et al., Nuclear Instruments and Methods **A176**, (1981) 255.

[44] B. Aubert et al., UA1 technical note TN-85-84-UA1 (1985).

[45] M.J. Corden et al., Nuclear Instruments and Methods **A238**, (1985) 273.

[46] K. Eggert et al., Nuclear Instruments and Methods **A176**, (1980) 217.

[47] A. Astbury et al., Nuclear Instruments and Methods **A238**, (1985) 288.

[48] G. Arnison et al., Phys. Letters **136B**, (1984) 294.

[49] G.A.P. Salvi, Ph.D. Thesis (1983), University of London, 'An Analysis of Hadronic Jets Produced in Proton-Antiproton Colisions at 540 GeV Centre of Mass Energy'.

[50] T.J.V. Bowcock, Ph.D. Thesis (1984), University of London, 'A Study of Hadronic Jets and Parton Properties Produced at the CERN SPS p-$\bar{\text{p}}$ Collider'.

[51] G. Sterman and S. Weinberg, Phys. Rev. Lett. **39**, (1977) 1463.

[52] G. Arnison et al., Phys. Letters **132B**, (1983) 214.

[53] G. Arnison et al., CERN preprint, CERN-EP/86-55 (1986).

[54] F. Paige and S.D. Protopopescu, ISAJET program, BNL 29777 (1981).

[55] E.J. Buckley and W. Kozanecki, UA1 technical note, TN-85-08-UA1 (1985).

[56] J.C. Collins and D.E. Soper, Phys. Rev. **D16**, (1977) 2219.

[57] B.L. Combridge and C.J. Maxwell, Nuc. Phys. **B239**, (1984) 428.

[58] F. Bergsma et al., Phys. Letters **153B**, (1985) 111.

[59] W.G. Scott and C. Albajar, private communication.

[60] H. Abramowicz et al., Z. Phys. **C12**, (1982) 289.

[61] W.J. Stirling, private communication.

[62] E.J. Eichten et al., Rev. Mod. Phys. **56**, (1984) 579.

[63] G. Arnison et al., Phys. Letters **158B**, (1985) 494.

[64] B. Humpert and R. Odorico, Phys. Letters **154B**, (1985) 211.

[65] B.L. Combridge and C.J. Maxwell, Phys. Letters **151B**, (1985) 299.

[66] Z. Kunszt and W.J. Stirling, CERN-TH.4351/86 (1986).

[67] J.A. Appel et al., Z. Phys. **C30**, (1986) 341.

[68] G. Arnison et al., CERN preprint, CERN-EP/86-92 (1986).

[69] T. Akesson et al., CERN preprint, CERN-EP/86-52 (1986).

[70] M. Bengtsson et al., LUND preprint, LU TP 86-11 (1986).